



**Calhoun: The NPS Institutional Archive**  
**DSpace Repository**

---

Theses and Dissertations

1. Thesis and Dissertation Collection, all items

---

1991-06

An analysis of middle ultraviolet emissions of  
molecular nitrogen and nitric oxide and  
vacuum calibration of an ultraviolet spectrograph

Mack, Bryan D.

Monterey, California. Naval Postgraduate School

---

<http://hdl.handle.net/10945/43747>

---

This publication is a work of the U.S. Government as defined in Title 17, United States Code, Section 101. Copyright protection is not available for this work in the United States.

*Downloaded from NPS Archive: Calhoun*



<http://www.nps.edu/library>

Calhoun is the Naval Postgraduate School's public access digital repository for research materials and institutional publications created by the NPS community. Calhoun is named for Professor of Mathematics Guy K. Calhoun, NPS's first appointed -- and published -- scholarly author.

**Dudley Knox Library / Naval Postgraduate School**  
**411 Dyer Road / 1 University Circle**  
**Monterey, California USA 93943**

AD-A245 984



✓  
②

# NAVAL POSTGRADUATE SCHOOL Monterey, California



## THESIS

DTIC  
ELECTE  
FEB 18 1992  
S B D

An Analysis of Middle Ultraviolet Emissions  
of Molecular Nitrogen and Nitric Oxide and  
Vacuum Calibration of an Ultraviolet Spectrograph

by

Bryan D. Mack

June, 1991

Thesis Advisor:

David D. Cleary

Approved for public release; distribution is unlimited.

92-03679



92 2 12 161

## REPORT DOCUMENTATION PAGE

Form Approved  
OMB No. 0704-0188

1a. REPORT SECURITY CLASSIFICATION Unclassified			1b. RESTRICTIVE MARKINGS		
2a. SECURITY CLASSIFICATION AUTHORITY			3. DISTRIBUTION/AVAILABILITY OF REPORT Approved for public release; distribution is unlimited.		
2b. DECLASSIFICATION/DOWNGRADING SCHEDULE					
4. PERFORMING ORGANIZATION REPORT NUMBER(S)			5. MONITORING ORGANIZATION REPORT NUMBER(S)		
6a. NAME OF PERFORMING ORGANIZATION Naval Postgraduate School	6b. OFFICE SYMBOL (If applicable) 39	7a. NAME OF MONITORING ORGANIZATION Naval Postgraduate School			
6c. ADDRESS (City, State, and ZIP Code) Monterey, CA 93943-5000		7b. ADDRESS (City, State, and ZIP Code) Monterey, CA 93943-5000			
8a. NAME OF FUNDING/SPONSORING ORGANIZATION	8b. OFFICE SYMBOL (If applicable)	9. PROCUREMENT INSTRUMENT IDENTIFICATION NUMBER			
8c. ADDRESS (City, State, and ZIP Code)		10. SOURCE OF FUNDING NUMBERS			
		PROGRAM ELEMENT NO.	PROJECT NO.	TASK NO.	WORK UNIT ACCESSION NO.
11. TITLE (Include Security Classification) An Analysis of Middle Ultraviolet Emissions of Molecular Nitrogen and Nitric Oxide and Vacuum Calibration of an Ultraviolet Spectrograph					
12. PERSONAL AUTHOR(S) Bryan D. Mack					
13a. TYPE OF REPORT Master's Thesis	13b. TIME COVERED FROM _____ TO _____	14. DATE OF REPORT (Year, Month, Day) 1991, June		15. PAGE COUNT 95	
16. SUPPLEMENTARY NOTATION The views expressed in this thesis are those of the author and do not reflect the official policy or position of the Department of Defense or the U.S. Government.					
17. COSATI CODES			18. SUBJECT TERMS (Continue on reverse if necessary and identify by block number)		
FIELD	GROUP	SUB-GROUP	Ultraviolet spectrum; Synthetic spectrum; Nitric Oxide; Lyman-Birge-Hopfield (LBH); Vacuum ultraviolet		
19. ABSTRACT (Continue on reverse if necessary and identify by block number)					
<p>Ultraviolet emissions from the earth's ionosphere in the wavelength range 1850 A to 2070 A are analyzed. Specifically, thirteen Lyman-Birge-Hopfield (LBH) band emissions from molecular nitrogen (N<sub>2</sub>) and the gamma, delta, and epsilon bands of nitric oxide are modelled with synthetic spectra to determine the atmospheric density of NO. Corrections to the Franck-Condon factors for the LBH emissions and the NO emissions are derived. Column emission rates are determined for N<sub>2</sub> and compared with computer models. Vacuum calibration of the MUSTANG ultraviolet spectrograph is presented.</p>					
20. DISTRIBUTION/AVAILABILITY OF ABSTRACT <input checked="" type="checkbox"/> UNCLASSIFIED/UNLIMITED <input type="checkbox"/> SAME AS RPT. <input type="checkbox"/> DTIC USERS			21. ABSTRACT SECURITY CLASSIFICATION Unclassified		
22a. NAME OF RESPONSIBLE INDIVIDUAL David D. Cleary			22b. TELEPHONE (Include Area Code) (408) 646-2828		22c. OFFICE SYMBOL 61-C1

Approved for public release; distribution is unlimited.

An Analysis of Middle Ultraviolet Emissions  
of Molecular Nitrogen and Nitric Oxide and  
Vacuum Calibration of an Ultraviolet Spectrograph

by

Bryan D. Mack  
Lieutenant, United States Navy  
B.S., Case Western Reserve University, 1981

Submitted in partial fulfillment  
of the requirements for the degree of

MASTER OF SCIENCE IN PHYSICS

from the

NAVAL POSTGRADUATE SCHOOL

June 1991

Author:

  
Bryan D. Mack

Approved by:

  
David D. Cleary, Thesis Advisor

  
Suntharalingam Ganalingam, Second Reader

  
Karlheinz E. Woehler, Chairman, Department of Physics

## ABSTRACT

Ultraviolet emissions from the earth's ionosphere in the wavelength range 1850 Å to 2070 Å are analyzed. Specifically, thirteen Lyman-Birge-Hopfield (LBH) band emissions from molecular nitrogen ( $N_2$ ) and the  $\gamma$ ,  $\delta$ , and  $\epsilon$  bands of nitric oxide (NO) are modelled with synthetic spectra to determine the atmospheric density of NO. Corrections to the Franck-Condon factors for the LBH emissions and the NO emissions are derived. Column emission rates are determined for  $N_2$  and compared with computer models. Vacuum calibration of the MUSTANG ultraviolet spectrograph is presented.

Accession For	
NTIS GRA&I	<input checked="checked" type="checkbox"/>
DTIC TAB	<input type="checkbox"/>
Unannounced	<input type="checkbox"/>
Justification	
By	
Distribution/	
Availability Codes	
Dist	Avail and/or Special
A-1	

## TABLE OF CONTENTS

I.	INTRODUCTION .....	1
A.	THESIS GOALS .....	3
B.	THESIS OUTLINE .....	3
II.	BACKGROUND .....	4
A.	EARTH'S ATMOSPHERE .....	4
1.	The Neutral Atmosphere .....	4
2.	The Ionosphere .....	7
B.	DIATOMIC MOLECULAR SPECTRA .....	11
1.	Energy Levels .....	12
2.	Spectral Lines .....	14
C.	TRANSITION MECHANISMS FOR N <sub>2</sub> AND NO .....	18
1.	Selection Rules .....	18
2.	Volume Emission Rates .....	19
D.	SYNTHETIC SPECTRA .....	24
III.	THE EXPERIMENT .....	28
A.	INTRODUCTION .....	28
B.	THE INSTRUMENT .....	29
C.	VACUUM CALIBRATION .....	29
1.	Vacuum Chamber .....	30
2.	Experimental Procedure .....	32
3.	Results .....	33

IV. ANALYSIS .....	39
A. FITTING THE OBSERVED SPECTRA .....	39
B. COLUMN EMISSION RATES .....	71
V. CONCLUSION .....	84
A. SUMMARY OF RESULTS .....	84
B. RECOMMENDATIONS FOR FURTHER RESEARCH .....	84
REFERENCES .....	86
INITIAL DISTRIBUTION LIST .....	88

## I. INTRODUCTION

The effects of the ionosphere on electromagnetic waves are of great interest to both the scientific and military communities. Radio astronomical observations, high frequency (HF) radio communication, and over-the-horizon (OTH) radar are just a few of the applications upon which variations in ionospheric conditions have great impact. The defining characteristic of ionospheric behavior is the density of free electrons. Electron density fluctuates widely both in time and location due to solar activity, geomagnetic activity and a number of other causes.

The current method of measuring electron density, which has been around for nearly 50 years, is to transmit a frequency-swept radio signal into the atmosphere and record the reflection at the ground site. While this method is fast and accurate, the electron density profile it produces is applicable only to that portion of the ionosphere immediately above the site. In order to produce reliable performance in HF communication or OTH radar, the electron density must be known over global areas. The 20 or so ionosonde stations currently in operation cannot provide the required geographic coverage, so new methods are being explored. One possibility for obtaining truly global measurement is to deploy orbiting ionosondes, but the power and mass requirements for active sensors in space currently make this approach impractical. This thesis presents a possible method of finding the ionospheric electron density over a large area using passive sensors.



The sensors in this case are the Naval Postgraduate School's (NPS) Middle Ultraviolet Spectrograph (MUSTANG), and the Naval Research Laboratory's (NRL) High Resolution Airglow and Aurora Spectrograph (HIRAAS). The method is the measurement and analysis of the ultraviolet (UV) airglow from Earth's upper atmosphere. Airglow is the radiation emitted from atoms and molecules which are in excited states due to photoexcitation, electron impact excitation, or chemical reaction. HIRAAS was designed to measure the emissions of atomic oxygen between 500 Å and 1500 Å, and will not be discussed in this thesis. MUSTANG was designed to observe the wavelength region from 1800 Å to 3400 Å in which the UV emissions from molecular nitrogen (N<sub>2</sub>) and nitric oxide (NO) are predominant. The purpose in studying these two molecules is that N<sub>2</sub> is the most abundant species in the atmosphere and plays an important part in many atmospheric phenomena, while NO, although only a trace constituent, is a strong source of ions in the lower ionosphere. Calculation of electron density begins with the measurement of emitted intensities which, in principle, allows inference of the volume density of the emitting species. Once the densities are known, models, such as those developed by Cleary (1986), of the chemical relationships between neutral species and ions can be used to find ion and electron densities.

## A. THESIS GOALS

The work presented in this thesis has two goals: to establish the sensitivity calibration for the MUSTANG spectrograph in the 1800 Å to 2000 Å wavelength range, and to determine emission profiles for N<sub>2</sub> and NO by fitting synthetic spectra to observed data.

## B. THESIS OUTLINE

This thesis contains five chapters. Chapter II presents introductory information on topics relevant to ionospheric spectroscopy. These topics include the structure of Earth's atmosphere and ionosphere, molecular spectroscopy, and the mechanisms of UV emission. Also in Chapter II is a discussion of the creation and utilization of synthetic spectra.

Chapter III describes the experiment and gives a brief description of the MUSTANG instrument. The vacuum chamber and the procedure for vacuum calibration of the instrument are also presented.

Analysis of the MUSTANG data and results of fitting with synthetic spectra are given in Chapter IV. Each of 25 observed spectra is approximated with a synthetic spectrum in the wavelength range 1850 Å to 2070 Å. The scaling factor which produces the best fit for each spectrum is then used to determine a column emission profile. Conclusions and suggestions for further research follow in Chapter V.

## II BACKGROUND

The purpose of this chapter is to provide a brief introduction to the concepts which are important in probing the ionosphere with a rocket-borne spectrograph. A thorough treatment of any one of these ideas would be a thesis in itself, so the material presented herein is necessarily brief.

### A. EARTH'S ATMOSPHERE

#### 1. The Neutral Atmosphere

Any description of the earth's atmosphere is complicated by the fluid nature of its thermal, chemical, and electrical characteristics. The two most common characterizations of the atmosphere are by temperature and by chemical composition. Characterization by temperature divides the atmosphere into four layers as shown in Figure 2-1. The first layer, the troposphere, extends from Earth's surface to roughly 15 km at mid-latitudes. Convective turbulence is the major physical process in the troposphere and is caused by the heating of the atmosphere from below by the warm surface. Tropospheric temperature decreases fairly evenly with altitude to about 210 K at the tropopause.

Above the tropopause lies the stratosphere, a layer about 25 km thick at mid-latitudes. The stratosphere exhibits a positive temperature gradient due to absorption of solar ultraviolet radiation near the base of the layer. Ozone is a particularly strong absorber of ultraviolet radiation in the

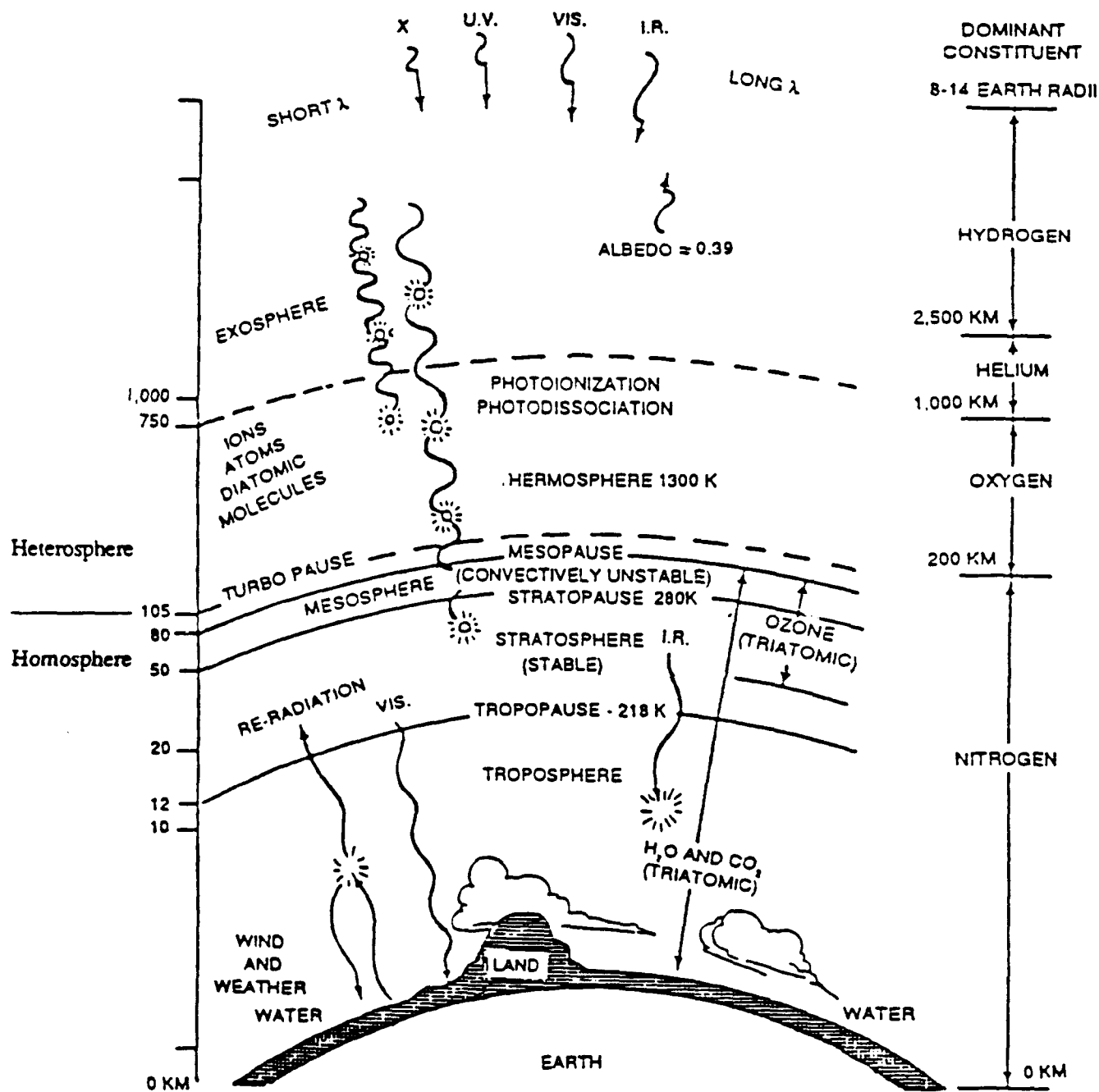


Figure 2-1 Atmospheric Regions (Tascione, 1988)

2000 Å to 3000 Å wavelength range. The temperature increase stops at the stratopause at an altitude of approximately 40 to 50 km.

The altitude region from about 50 km to 80 km is called the mesosphere and is another region of negative temperature gradient. Temperature in the mesosphere is controlled largely by convection, with the warmer stratosphere below affecting the layer much as the planet's surface affects the troposphere. The atmosphere reaches its lowest kinetic temperature of about 180 K at the mesopause near 80 km altitude.

Extending from the mesopause to the ill-defined outer edge of the atmosphere, the thermosphere is marked by a strong positive temperature gradient near its base. There are several factors which cause the gradient, notably the very low density of the gases, the extremely small number of triatomic molecules, and heating of the atmosphere from above by short wavelength solar radiation. With the atmosphere heated *from above* rather than from below, convection ceases and kinetic temperature rises to a level dependent on solar activity. The high temperatures of the thermosphere are the result of the lack of heat removal processes, other than radiation, at low particle density. Beyond 400 km to 500 km altitude, the temperature stops rising and becomes independent of altitude.

Characterization by chemical composition leads to a three-layer description of the atmosphere. Temperatures and densities in the troposphere, stratosphere, and mesosphere are sufficiently high that convective mixing results in uniform distribution of all the atmospheric gases. This region of uniform distribution is called the homosphere and has a composition of approximately 78% molecular nitrogen, 21% molecular

oxygen, and 1% other gases. The upper limit of the homosphere, called the turbopause, is marked by stable temperature gradients and the emergence of molecular diffusion rather than convective mixing as the primary physical process. Molecular diffusion and the subsidence of mixing above the turbopause cause the atmospheric species to stratify according to mass, resulting in a region called the heterosphere. In the heterosphere, nitrogen remains largely in molecular form while photodissociation of molecular oxygen produces significant amounts of atomic oxygen above 100 km.

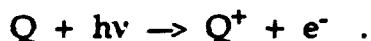
Above approximately 500 km, lies the exosphere which is made mostly of helium and hydrogen at high kinetic temperature and which forms an indistinct boundary between Earth's atmosphere and space somewhere above 1000 km. The exosphere is marked by densities so low that particle trajectories are no longer the random paths caused by collisions with other particles, but become the parabolic trajectories of free-falling bodies.

## 2. The Ionosphere

Although most of the atmosphere is made of neutral atoms and molecules, portions of the upper atmosphere have ions and free electrons present in sufficient numbers to create a plasma which affects radiowave propagation. Such regions compose the ionosphere. The ionosphere is a weak plasma in that even the maximum free electron concentration is three orders of magnitude smaller than the concentration of neutral species. The ionosphere is categorized into layers, labelled D, E, and F, according to altitude and formation process.

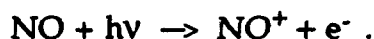
The production of charged particles in the upper atmosphere is due primarily to ionization of neutral gas atoms and molecules by solar

ultraviolet and x-radiation. The creation of layers of electron density can be explained by studying a representative reaction. The ionization of molecule Q can be written as

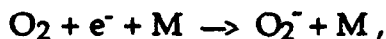


The rate of formation of free electrons depends on the product of the concentration of Q and the flux of photons. Particle density falls exponentially while the flux of ionizing photons asymptotically approaches a maximum as altitude increases, resulting in peak in electron production at some altitude (see Figure 2-2). This electron production peak creates an ionospheric layer.

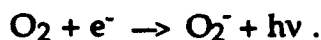
The lowest layer is the D region which extends from about 50 km to 90 km. The primary source of ions in the D region is photoionization of NO by solar Lyman- $\alpha$  radiation, written as



Daytime electron densities are between  $10^2$  and  $10^4 \text{ cm}^{-3}$ . Relatively high particle densities lead to rapid recombination of ions and electrons and cause the the D region to disappear at night. Other significant sources of ions are three-body attachment reactions, e.g.



and radiative attachment, such as



The major loss processes in the D region are collisional detachment, photodetachment, and mutual neutralization. The last process, exemplified by the reaction  $A^+ + B^- \rightarrow A + B$  , indicates the presence of large numbers of negative ions in the layer.

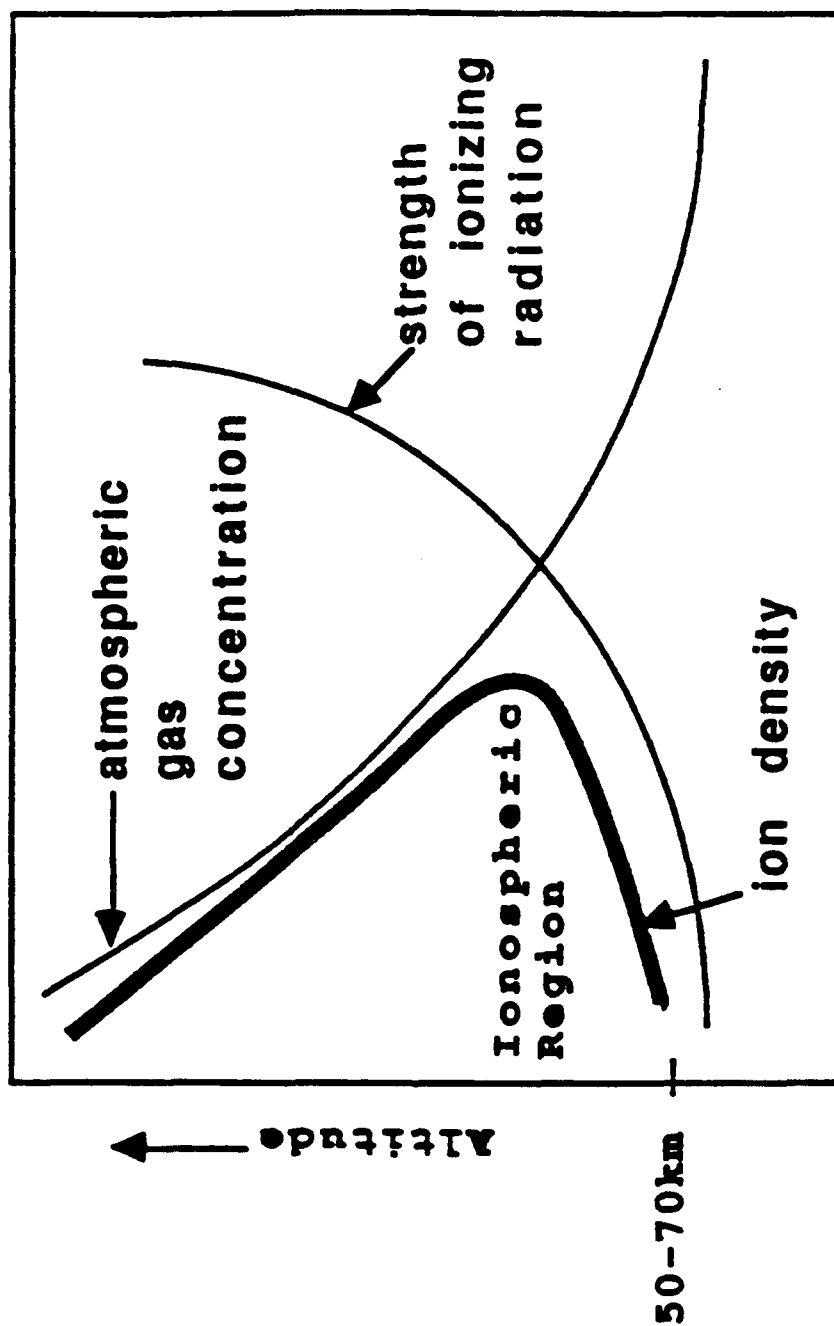
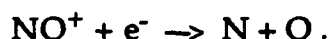


Figure 2-2 Ionospheric Layer Formation



Between 90 km and 140 km lies the E region which is formed mostly by the absorption of far- and extreme ultraviolet (FUV and EUV) and soft x-rays by diatomic and monatomic oxygen.  $\text{NO}^+$  and  $\text{O}_2^+$  are the most abundant ions in the E region, with a smaller concentration of  $\text{O}^+$ . Typical electron density in the E region is  $10^5 \text{ cm}^{-3}$ . The principal loss mechanism is dissociative recombination, for example



Like the D layer, the E layer tends to disappear at night, except at high latitudes where energetic particle bombardment of the upper atmosphere causes continued ionization after sunset.

The  $\text{O}^+$  concentration increases with altitude until it becomes the dominant ion in the F region. The F region is subdivided into F1 and F2 layers, the F1 layer occupying the 140 km to 200 km altitude range, and the F2 layer above 200 km. The presence of an F1 layer as a discernable entity is dependent on solar activity. When it is present, typical electron density in the F1 layer is  $2 \times 10^5 \text{ cm}^{-3}$ . The principal ions in the F1 layer are  $\text{O}^+$  and  $\text{NO}^+$ . In the absence of ionizing radiation, these ions quickly disappear via charge exchange and dissociative recombination. Thus, the F1 layer disappears at night. The uppermost layer of the ionosphere, the F2 layer, has the largest free electron density in the ionosphere. Daytime density is of the order of  $2 \times 10^6 \text{ cm}^{-3}$  at a nominal altitude of 300 km. Absorption of EUV radiation by atomic oxygen is the major ionization process in the F2 layer, and  $\text{O}^+$  the most abundant ion. Part of the reason for the relatively large electron density in the F2 layer is the fact that ion-molecule charge exchange replaces dissociative recombination as the major loss mechanism. This causes the loss

rate of ions to diminish as altitude and particle density decrease. Relatively low densities and bombardment by energetic particles allow the F2 region to persist at night with electron densities about five percent of daylight levels.

## B. DIATOMIC MOLECULAR SPECTRA

The radiation spectrum of a molecule is a measure of the change in its energy as it changes state. The energy state of a diatomic molecule can be described by four quantities. The first quantity is the kinetic energy of the molecule due to the velocity of its center of mass. This energy is linearly proportional to the temperature of the molecule, and it can have any of a continuum of values. When the temperature of the upper atmosphere is said to be, for example, 1400 K, it is equivalent to saying the average kinetic energy of the molecules and atoms in the region is

$$1400 \cdot k = 1.93 \times 10^{-20} \text{ J} = 0.121 \text{ eV} \quad (2.1)$$

where  $k = 1.381 \times 10^{-23} \text{ J/K}$  is Boltzmann's constant. Energies of the order of 0.1 eV correspond to infrared radiation, which is not examined in this thesis. The three other quantities which define the energy state of a diatomic molecule are related to the internal structure of the molecule, specifically its electronic, vibrational, and rotational states. In accordance with the laws of quantum mechanics, these terms can have only discrete values. The quantization of energy values is reflected in the radiation produced when the values change. Such radiation is not continuous, but forms spectra with emission peaks at wavelengths corresponding to the energy of the allowed transitions for the radiating molecule.

## 1. Energy Levels

The subject of molecular spectroscopy is treated in several texts, and the following explanation is taken largely from that of Herzberg (1950). The energy state of a molecule can be found by modelling its motions. The simplest model of a diatomic molecule is one of two masses connected by a massless rigid rod. In addition to translation of its center of mass, there are two possible motions for the molecule: rotation about the center of mass, and vibration along the internuclear axis.

Solution of the Schrodinger equation for a rigid rotator leads to energy levels given by

$$E(J) = \frac{h^2 J(J+1)}{8\pi^2 \mu r^2} \quad , \quad (2.2)$$

where  $J$  ( $=0,1,2,\dots$ ) is the rotational quantum number and  $h$  is Planck's constant. The term  $\mu r^2$  is the moment of inertia for the dumbbell model. When the energy of a state is measured relative to the ground state it is called a term value. The rotational term value is the rotational energy divided by the constant  $hc$ , and is given the symbol  $F(J)$ . To calculate the vibrational energy levels, the rod in the model is replaced by a spring, resulting in an harmonic oscillator. The solution of Schrodinger's equation for a simple harmonic oscillator is well known and results in energy levels given by

$$E(v) = \frac{h}{2\pi} \sqrt{\frac{k}{\mu}} \left( v + \frac{1}{2} \right) \quad , \quad (2.3)$$

where  $v$  is the vibrational quantum number,  $\mu$  the reduced mass, and  $k$  the "spring constant" or force constant for the interaction between the atoms. Analogously to the rotational term value, the vibrational term value,  $G(v)$ , is  $E(v)$  divided by  $hc$ . Since real molecules are neither rigid rotators nor true

harmonic oscillators, the expressions derived above for term values are approximations. Nonetheless, the expressions are conceptually straightforward and illustrate the origin of multiple spectral lines.

There is a third way in which the energy state of a molecule can change, namely by making a transition between electronic energy levels. As is true for individual atoms, the electrons in a molecule have a total orbital angular momentum, denoted  $L$ . In general,  $L$  will precess about the internuclear axis, but the component of  $L$  along the axis is a constant of the electronic motion, and is, therefore, a useful measure of the electronic state of the molecule. This axial component of  $L$ , called  $M_L$ , is quantized and can have values  $L, L-1, L-2, \dots, -L$ . The magnitude of  $M_L$  is given the symbol  $\Lambda$ , so that  $\Lambda = |M_L| = 0, 1, 2, \dots, L$ . The values of  $\Lambda$  for molecular states are given Greek letters corresponding to the Roman letters used to designate orbital angular momentum for atomic states. States  $\Sigma$ ,  $\Pi$ , and  $\Delta$  correspond to  $\Lambda = 0, 1$ , and  $2$ . In addition to their orbital angular momentum, the electrons in a molecule have spin angular momentum which generates a resultant spin,  $S$ . The spin will precess around the internuclear axis in the presence of a magnetic field, but, as with the orbital angular momentum, the component of  $S$  along the axis is a constant of the electron motion. This component, labelled  $\Sigma$ , can be oriented either parallel or anti-parallel to the internuclear axis, so there are two values of the spin quantum number in the presence of a magnetic field. When  $\Lambda = 0$ , there is no internal magnetic field in the molecule, and there is only one value for the axial component of spin. When  $\Lambda$  is not 0, the orbiting electrons create an internal magnetic field, giving rise to  $2S$  values of spin. All together then there are  $2S + 1$  possible values of spin angular momentum

for a molecule. The quantity  $(2S + 1)$  is called the multiplicity of the state of the molecule. The term value for electronic energy is given the symbol  $T_e$ . The values of  $T_e$  are determined by laboratory measurement and have been compiled for most diatomic molecules in Huber and Herzberg (1979).

In spectroscopic notation, the multiplicity of a state is written as a left superscript to the orbital angular momentum symbol. For example, a state having spin quantum number 0 ( $\Sigma + 1 = 1$ ) and orbital angular momentum quantum number  $\Lambda = 1$  is written  $^1\Pi$ . The electronic configuration of the molecule is also given a letter designation. X is used to identify the ground state, with succeeding excited states given symbols A, B, C, or a, b, c depending on whether the excited state has multiplicity the same as (upper case) or different from (lower case) the ground state. A complete description of molecular spectroscopy notation may be found in Herzberg (1950).

## 2. Spectral Lines

The relationships between electronic, vibrational, and rotational energy levels are shown in Figure 2-3. Except in the case of a single atom with  $S=0$ , the radiation from a change in energy is not a single line, but a multiplet of lines which are closely spaced in wavelength. In diatomic molecules, the many possible combinations of rotational and vibrational states lead to multi-line spectra even for transitions between electronic states with multiplicities of one. Figure 2-4 shows the effect of the vibrational and rotational terms on the spectrum of the electronic transition from the first excited state to the ground state of nitric oxide. Note in the figure that the spacing between lines can be fractions of an Angstrom, corresponding to energy differences of the

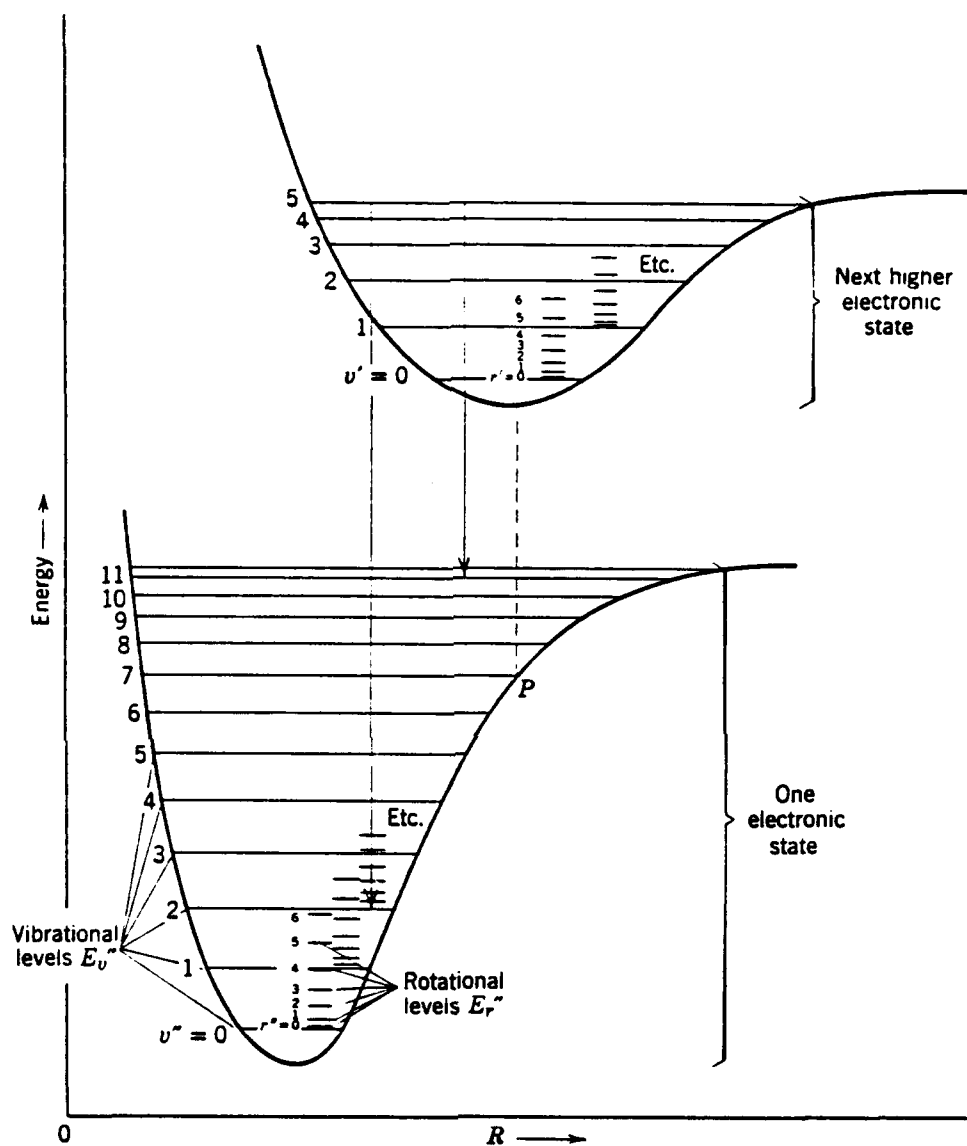


**Figure 2-3 Relationship Between Electronic, Vibrational, and Rotational Energy Levels (Eisberg and Resnick, 1985)**

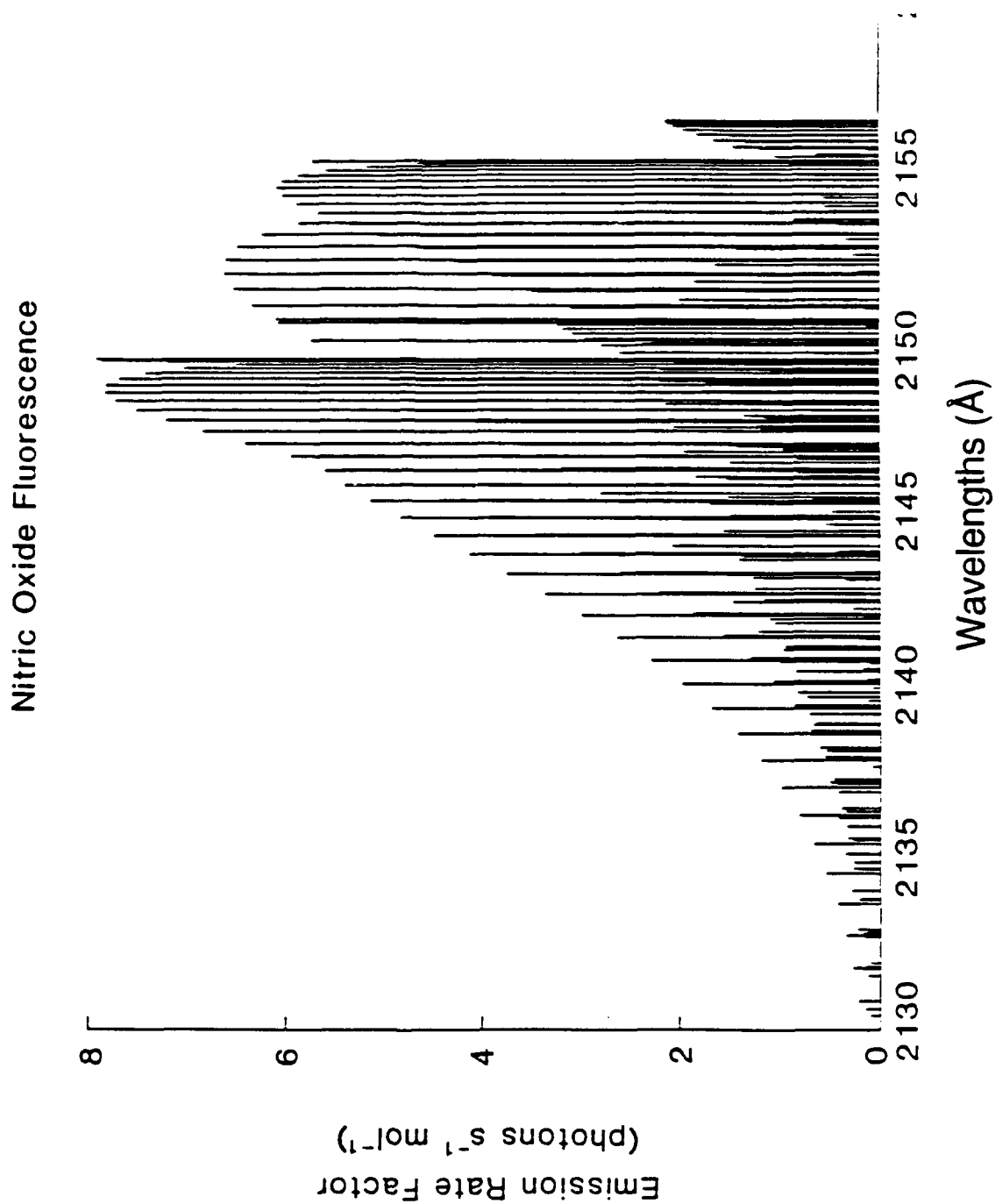


**Figure 2-4** High Resolution Spectrum Showing Vibrational and Rotational Structure (Cleary, private communication)

order of  $10^{-4}$  eV between rotational energy levels. When measured with an instrument such as MUSTANG, which has a wavelength resolution of approximately 10 Å, the many lines appear as one broad peak. Compare Figure 4-2.

The wave number,  $\sigma$ , of a spectral line is determined by the difference in energies between the initial and final states, and is given by

$$\sigma = \frac{E_i - E_f}{hc} \quad (2.4)$$

From the preceeding discussion on term values, the term value,  $T$ , for a given state may be written

$$T = T_e + G(v) + F(J) \quad (2.5)$$

Using the convention of denoting the upper state of a transition with a single prime and the lower state with a double prime, the wave number for a given transition can be written

$$\sigma = T' - T'' = T'_e - T''_e + G(v') - G(v'') + F(J') - F(J'') \quad (2.6)$$

The group of transitions for which the upper and lower electronic energies are fixed is referred to as a molecular band system. This thesis is concerned with the LBH bands of molecular nitrogen and the  $\gamma$ ,  $\delta$ , and  $\epsilon$  bands of nitric oxide. For each of these band systems, the lower electronic state is the ground state.



## C. TRANSITION MECHANISMS FOR N<sub>2</sub> AND NO

### 1. Selection Rules

The airglow spectrum in the 1800 Å to 2000 Å wavelength range is composed of the LBH bands of N<sub>2</sub> and the γ, δ, and ε bands of NO. The specific transitions involved are:

$$\gamma: A^2\Sigma^+ \longleftrightarrow X^2\Pi_r$$

$$\delta: C^2\Pi \longleftrightarrow X^2\Pi_r$$

$$\epsilon: D^2\Sigma^+ \longleftrightarrow X^2\Pi_r$$

in NO and

$$a^1\Pi_g \longleftrightarrow X^1\Sigma_g^+$$

in molecular nitrogen for LBH. The γ, δ, and ε bands of NO arise from allowed transitions, but the LBH transition is forbidden. The term 'forbidden' does not indicate that a particular transition never occurs. Instead, it means that the selection rules governing the occurrence of such a transition via electric dipole radiation are violated. For a brief explanation of selection rules, consider the case of a one-electron atom with a dipole moment  $p = -er$ , where  $e$  is the electron charge and  $r$  is the vector from the center of the nucleus to the electron. The probability per unit time that the atom will emit a photon, the transition rate, can be written

$$R = \frac{16\pi^3\nu^3 p_{fi}^2}{3\epsilon_0 hc^3},$$

where  $\nu$  is the frequency of the photon. The term  $p_{fi}$  is called the matrix element of the electric dipole moment between the initial and final states, and is defined by the equation

$$p_{fi} = \left| \int \psi_f^* e r \psi_i d\tau \right| , \quad (2.7)$$

where  $\psi_i$  and  $\psi_f^*$  are the eigenfunctions describing the initial and final energy levels and  $d\tau$  indicates integration over all space. The selection rules are a set of conditions on the quantum numbers associated with  $\psi_i$  and  $\psi_f$ , which lead to a value of zero for  $p_{fi}$  when those conditions are violated (Eisberg and Resnick, 1985). Violation of the selection rules leads to a transition rate of zero, hence, a "forbidden" transition. The rules for multi-electron atoms and molecules are derived in a similar manner, but with vastly more complicated wavefunctions.

The designation of the LBH band transition as forbidden means that it is not driven by a change in the electric dipole moment of the nitrogen molecule. In particular, the LBH transition violates a rule which requires the change in the sum of the orbital angular momenta of the electrons in the  $N_2$  molecule to be  $\Delta L = \pm 1$  for electric dipole radiation. There is, however, another rule which says that the electron angular momentum may change by  $\Delta L = \pm 2$  and produce radiation via a change in the electric quadrupole or magnetic dipole moments of the molecule. It is this rule which leads to LBH radiation. Because of these selection rules, the excitation mechanism for LBH is not photoexcitation but energetic photoelectron impact. In contrast, the nitric oxide bands, which come from allowed transitions, are driven by photoexcitation and emit via electric dipole radiation.

## 2. Volume Emission Rates

The population of a state depends on the electronic, vibrational, and rotational term values which define it. An accurate expression for the

population requires that corrections be made to the expressions for term values derived from the simple model of the diatomic molecule.

The first correction accounts for the anharmonicity of real vibrational motion. The corrected vibrational term value is written

$$G(v) = \omega_e(v + \frac{1}{2}) - \omega_e x_e(v + \frac{1}{2})^2 \quad . \quad (2.8)$$

$\omega_e$  and  $x_e$  are constants of the molecule and are listed in Huber and Herzberg (1979). Corrections to the rotational term values involve the multiplicity of the state and are more complicated than those for the vibrational terms. For singlet states, the corrected rotational term value is

$$F(J) = B_v J(J + 1) - D_v J^2(J + 1)^2 \quad . \quad (2.9)$$

The  $B_v$  and  $D_v$  terms depend on the vibrational state of the molecule and are found from the expressions

$$B_v = B_e - \alpha_e(v + \frac{1}{2}) + \text{higher order terms}, \quad \text{and} \quad (2.10)$$

$$D_v = D_e - \beta_e(v + \frac{1}{2}) + \text{higher order terms} \quad . \quad (2.11)$$

The constants  $B_e$ ,  $D_e$ ,  $\alpha_e$ , and  $\beta_e$  are again found in Huber and Herzberg. When the multiplicity of the state is greater than one, the rotational term value depends strongly upon the coupling between orbital and spin angular momenta. Hund (1927) classified five coupling schemes based on the strength of the coupling. These schemes will not be explored in this thesis, but they are discussed in Cleary (1985) and Bosserman (1989).

The volume emission rate of a specific spectral line is the product of the population of the upper state to which the line corresponds and the coefficient for spontaneous emission between the upper and lower states. Using the notation VE for volume emission rate, N for the fraction of molecules in the upper state, A for the spontaneous emission coefficient, and n to denote electronic state, the emission rate can be written

$$E(n'v'N'J'p', n''v''N''J''p'') = N(n'v'N'J'p') A(n'v'N'J'p', n''v''N''J''p'') \quad , \quad (2.12)$$

where n,v,N,J, and p describe the electronic, vibrational, and rotational state according to Hund's models. For an upper level defined by n' and v', the fractional population of the level, in steady state, is found by dividing the production rate, P(n'v'), by the loss rate for that level. In both the LBH and the nitric oxide bands, the loss rate for the upper level is just the sum of the spontaneous emission rates to all possible lower vibrational levels.

Quenching can be ignored for LBH above 95 km (Vallance Jones, 1974). The fractional population is then written

$$N(n'v') = \frac{P(n'v')}{\sum_{v''} A_{v'v''}} \quad . \quad (2.13)$$

For the nitric oxide bands, the production rate depends on the solar flux, the absorption cross-section for transition to the upper state, and on molecular number density. Using the notation of Barth (1965), this rate can be written as

$$P(n'v') = \pi F \frac{\pi e^2}{mc^2} \lambda_{0v'}^2 f_{xn} q_{0v'} \quad (2.14)$$

where  $\pi F$  is the solar flux,  $\lambda$  is the wavelength of the incoming photon,  $f_{xn}$  is the oscillator strength for the electronic transition from ground state X to

upper state  $n$ , and  $q_{0v'}$  is the Franck-Condon factor for the  $v=0$  level of the ground state to the  $v'$  level of the excited state. Franck-Condon factors are explained below. In the case of the LBH bands, the excitation rate depends on the number density and on the photoelectron flux and electron impact cross-section of the molecules. The production rate in this case can be expressed as follows:

$$P(n'v') = q_{0v'} N \int \phi(E) \sigma(E) dE , \quad (2.15)$$

where  $N$  is the number density,  $\phi(E)$  denotes the flux of photoelectrons,  $\sigma(E)$  is the cross-section for an  $X$ -to- $n'$  electronic transition, and  $dE$  indicates integration over the range of photoelectron energies. The difference in excitation processes for the two molecules makes calculation of the excitation rate for NO much easier than that for  $N_2$ .

The flux of photons with the correct energies to excite the NO bands exhibits little variability over the solar cycle. The absorption cross-sections of NO for these photons are constants and have been measured. On the other hand, the flux of the photoelectrons which produce the upper state of the LBH transition is highly variable. The primary source of photoelectrons is the ionization of  $N_2$ ,  $O_2$ , and O by solar EUV radiation, particularly the He 304 Å emission. Variations in the sun's output become larger as the wavelength of the radiation gets shorter, so the EUV emissions which generate photoelectrons fluctuate more than do the MUV emissions sustaining NO excitation. Also, these photoelectrons have sufficient kinetic energy to cause multiple ionizations. The secondary photoelectrons penetrate into the atmosphere causing more ionization and losing energy in collisions

until they are thermalized. The energy spread of this cascade of photoelectrons must be modelled by some form of random distribution. Since the collision cross-section of nitrogen is a function of energy, accurate calculation of the LBH excitation rate requires knowledge of the energy distribution of the photoelectrons.

When the excitation rate has been established, the population of specific states must be determined. To make this determination, the branching ratio into the available vibrational and rotational levels must be found. For given electronic levels, the branching ratio into the available vibrational levels is found in the Franck-Condon factors. The Franck-Condon factors represent the transition probabilities between upper and lower vibrational states. When the wavefunctions for the vibrational states are known, the Franck-Condon factor can be calculated from

$$q_{v'v''} = \left| \int \psi_u \text{er} \psi_l d\tau \right| \quad (2.16)$$

where  $v'$  is the upper vibrational state with wavefunction  $\psi_u$ , and  $v''$  is the lower vibrational state with wavefunction  $\psi_l$ . When the wavefunctions are not known, the factors for a band progression must be measured. The sum of all Franck-Condon factors for a fixed value of  $v'$  or a fixed value of  $v''$  is unity, signifying that the vibrational transition that actually occurs must be one of those available. When the Franck-Condon factor is relatively large, the radiation from the corresponding vibrational transition is strong. This fact is important in the fitting of synthetic spectra to the measured data presented in Chapter IV. The branching ratio from a particular vibrational level into each of the available rotational states,  $J$ , is determined by the Honl-

London factors. The sum of the Honl-London factors for a fixed value of  $J'$  is  $(2J' + 1)$ , so the Honl-London factor for a specific rotational transition must be divided by  $(2J' + 1)$  to give a probability.

Assembling Equations (2.12), (2.13), and (2.14) or (2.15) as appropriate, gives a final expression for the volume emission rate as

$$E = P(n'v') \frac{N(n'v'N'J'p')}{N(n'v')} \frac{A_{v'v''}}{\sum_{v''} A_{v'v''}} \frac{S(J'J'')}{2J' + 1} \quad (2.17)$$

In measuring emission rates, account must be taken of the phenomenon of self-absorption. Self-absorption occurs when a photon emitted from an excited molecule is absorbed by a molecule of the same species. Since the molecules have identical energy state structures, the energy of the emitted photon will match exactly one of the transition energies in the molecule it strikes, and the photon may be absorbed. For this to be true, the absorbing molecule must be in the same state as was the emitting molecule after it emitted the photon. Since the vast majority of molecules in the atmosphere are in the lowest vibrational state, only those photons from transitions to  $v''=0$  are likely to be absorbed. Note that since the LBH transition is driven by photoelectron impact rather than photoexcitation, its emissions are not subject to self-absorption.

#### D. SYNTHETIC SPECTRA

In order to analyze the observed spectra, models are needed which create synthetic spectra based on theoretical considerations such as those which lead to Equation (2.17). Such models have been developed by Cleary (1986) for the  $\gamma$ ,  $\delta$ , and  $\epsilon$  bands of nitric oxide and for the LBH bands of  $N_2$ . The basis of the

model is the calculation of a theoretical volume emission rate for each rotational line in a molecular band. The spectral region of concern is divided into wavelength bins, and the emission rates are placed in the appropriate bins to create a synthetic spectrum.

Before a spectrum from one of these models can be used for comparison with observed data, it must be conditioned to reflect the characteristics of the measuring instrument. To do so, the synthetic spectrum is convolved with the instrument slit function. The slit function is the frequency domain transfer function of the spectrograph, and is determined by measuring the instrument response to a wavelength delta function. For the MUSTANG slit function determination, the delta functions were approximated by several of the spectral lines of atomic mercury. The wavelength resolution of the MUSTANG was found to be 10.6 Å, and the effect of convolution on the synthetic spectra can be seen in Figure 2-5. As noted earlier, the resolution of the MUSTANG is too coarse to show the rotational structure of a band.

One purpose of fitting the observed spectra with synthetic ones is to find column densities of NO at each altitude. As explained previously, the excitation rate for NO is calculable, so the measured emission rate is directly related to the density of nitric oxide. The relationship between the synthetic fit and column density is straightforward. The intensity recorded by the spectrograph is a volume emission rate integrated over the instrument line of sight, while the synthetic spectrum represents the volume emission rate from a single molecule. The scale factor between the synthetic and observed spectra is, therefore, equal to the column density of the emitting molecule. The molecular densities then become inputs to other models which lead to



the ultimate goal of deducing ionospheric electron densities. The use of synthetic spectra to infer molecular nitrogen density from LBH emissions is not as direct as it is for nitric oxide. While the scale factor for the LBH spectra still represents column emission rate, as it does for the NO spectra, the rate cannot be directly converted to a density for nitrogen. Many of the parameters that affect the LBH emission rate are not directly measureable, and the relative variations among them are unknown. For example, the density of nitrogen is one of the important factors in determining the photoelectron flux driving the emissions by which we seek to measure nitrogen density. The coupling between variables makes it necessary to assume values for certain parameters, and to use those values to generate coherent results.

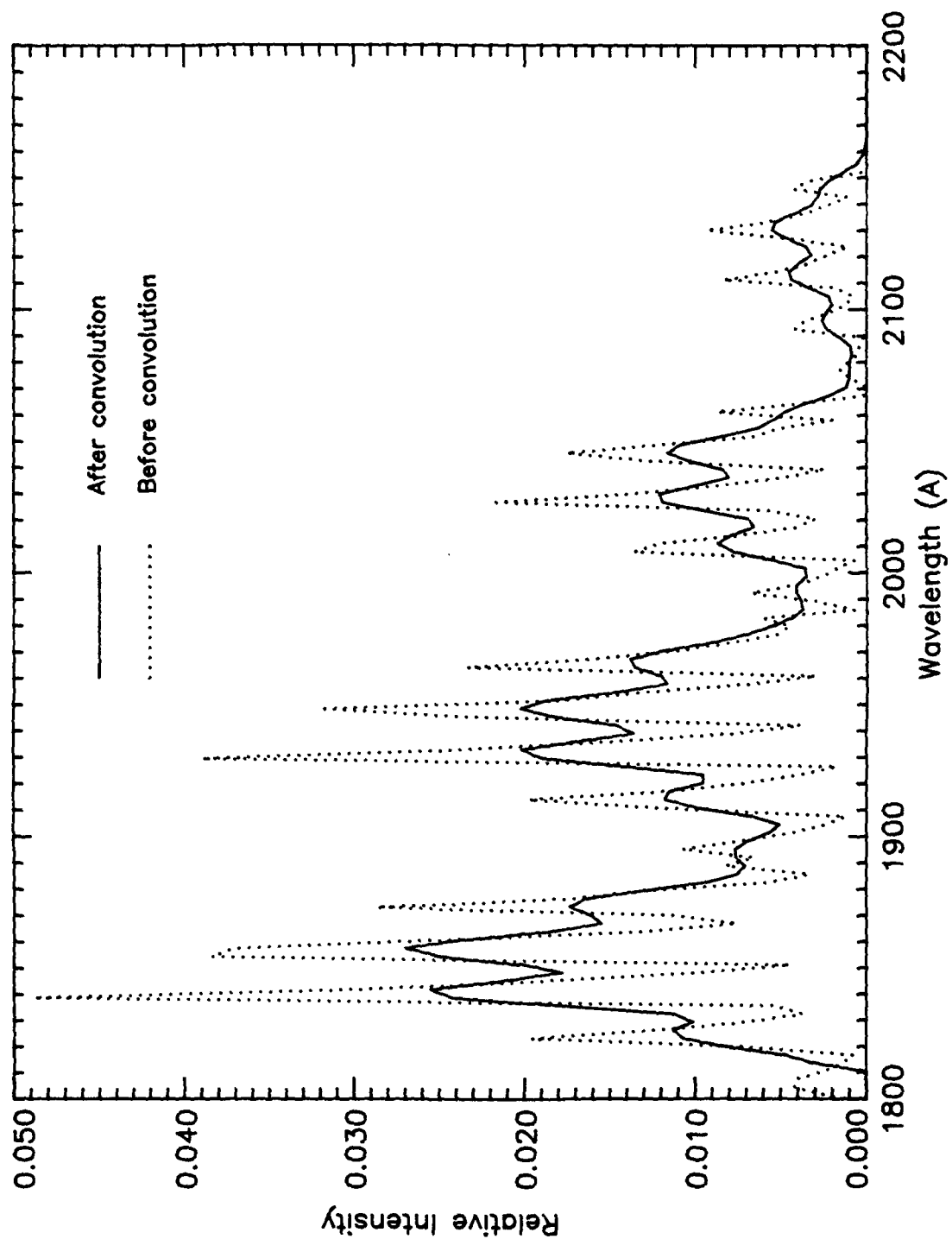


**Figure 2-5 Effect on Synthetic Spectrum of Convolution with MUSTANG Slit Function**

### III. THE EXPERIMENT

#### A. INTRODUCTION

The MUSTANG instrument constituted half of an ionospheric research package that was launched at 1700 GMT on 30 March, 1990 from White Sands Missile Range aboard a NASA Terrier boosted Black Brant sounding rocket. The other half of the payload was the NRL HIRAAS, an instrument designed to measure UV emissions, primarily from  $O^+$ , in the 500 Å to 1500 Å wavelength region. Latitude and longitude of the launch site are 32.4° N and 106.34° W, respectively. At the time of launch, the solar zenith angle was 62.9°, and F10.7 was 186.9. Total flight time was approximately 14 minutes, with the payload reaching a maximum altitude of 320 kilometers. An active attitude control system kept the payload properly oriented for data collection throughout the flight. For MUSTANG, the correct orientation was a 90° observation-zenith angle (horizontal view in the rocket's frame of reference) and 90° solar-observation angle. This orientation results in a view through the limb of the earth's atmosphere. Such a view was necessary both to prevent saturation of the detector by the very bright airglow in the nadir direction, and to enable detection of the NO and N<sub>2</sub> emissions between 1800 Å and 3000 Å which are almost completely absorbed by O<sub>2</sub> and O<sub>3</sub> in the nadir view. The MUSTANG instrument has no inherent recording capability, so the data were telemetered to a recording station on the ground. The payload section of the rocket was recovered after a parachute-retarded final descent.

## B. THE INSTRUMENT

The MUSTANG instrument is a space-qualified 1/8 meter Ebert-Fastie spectrograph with an off-axis telescope. A photodetector consisting of an image intensifier optically coupled to a linear photodiode array is positioned at the exit focal plane of the spectrograph. The voltage output from each of the 512 photodiodes in the array is proportional to the intensity of radiation at the wavelength to which the diode corresponds. The limits of wavelength coverage are from 1800 Å to 3400 Å which is the middle ultraviolet portion of the electromagnetic spectrum. The spectral resolution of MUSTANG is 10.6 Å; and, to avoid anomalous data spikes, the radiation at a given wavelength was sampled by three adjacent pixels, each of which has a coverage of 3.133 Å. For a complete description of the detector, see Clayton (1990) or Andersen (1990).

## C. VACUUM CALIBRATION

Calibration of the spectrograph in the wavelength range 2000 Å to 3400 Å was accomplished by Andersen (1990) in his analysis of the OII 2470 Å and OI 2972 Å features. An extension of that calibration to wavelengths below 2000 Å was done to enable analysis of the LBH bands of N<sub>2</sub> from 1850 Å to 2070 Å. Such an extension required the removal of oxygen from the path between the UV calibration source and the spectrograph in order to preclude absorption of the signal by the O<sub>2</sub> Schumann-Runge bands. Oxygen absorption was eliminated by performing the calibration in a vacuum chamber which had been evacuated and refilled with nitrogen.

## 1. Vacuum Chamber

The vacuum chamber, shown schematically in Figure 3-1, was built from a 1.5 m long section of PVC pipe 12 inches in diameter. One end of the chamber was sealed with an end cap through which ports were drilled and tapped for the vacuum and nitrogen backfill lines. A vacuum gauge was fitted to the nitrogen line. The other end of the pipe was fitted with a flange assembly containing an O-ring groove and an attaching ring to which a 12.5 mm-thick aluminum plate was bolted. A hole in the center of the aluminum plate was covered by an 110 mm diameter feed-through plate through which a 37-pin ribbon cable and three single wires were passed. The ribbon cable provided connection to the spectrograph, and the wires provided power to a deuterium discharge lamp. The deuterium lamp is an ultraviolet spectral irradiance standard for calibration of spectroradiometer systems.

Inside the chamber, the instrument and the lamp were mounted on a 4.75 mm thick aluminum table measuring 1.4m x .285m. The lamp was mounted, at a height corresponding to the center of the entrance slit in the spectrograph, on a micrometer-driven translation stage. The translation stage allowed the precise horizontal positioning of the lamp required to get a useable signal through the 140- $\mu$ m width of the slit. The distance from the lamp to the detector was 1.83 m and, when properly positioned, the lamp output was sufficiently strong to saturate the detector. A piece of black card stock with a pinhole in the center was placed over the end of the spectrograph telescope reducing the signal intensity to a non-saturating level. The close proximity of the lamp to the wall of the chamber caused concern about the

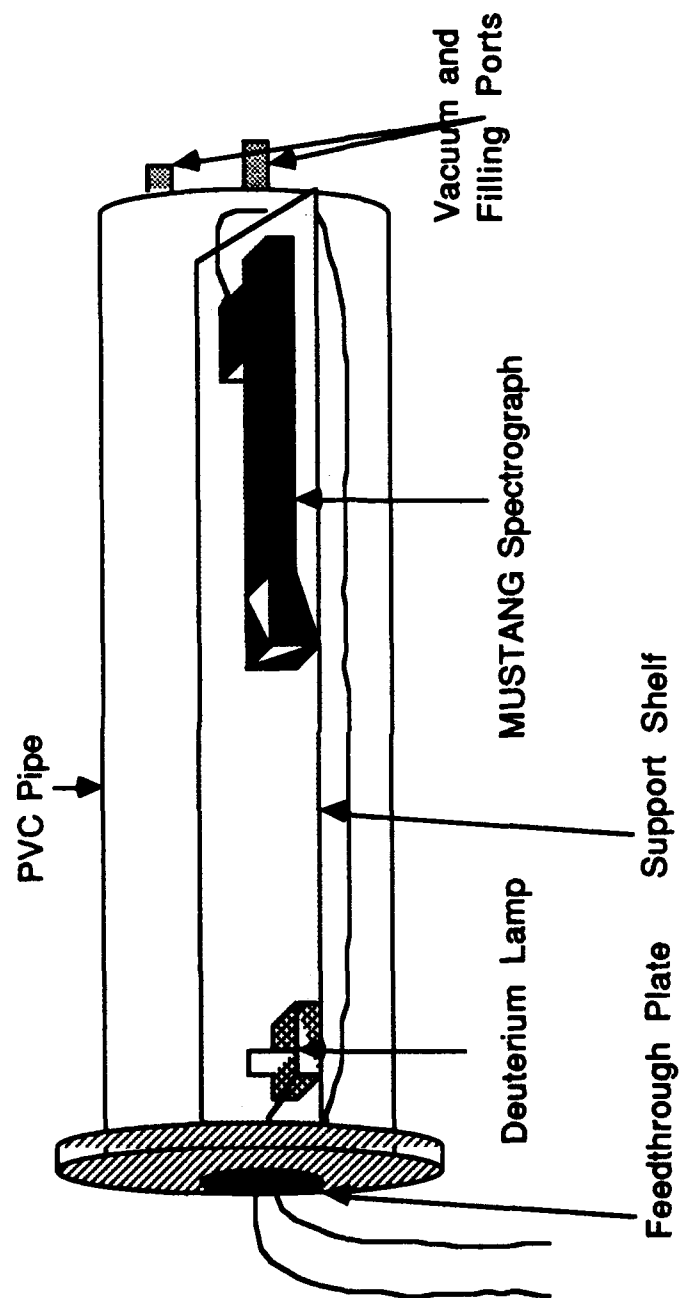


Figure 3-1 Schematic Diagram of Vacuum Calibration Chamber

possibility of heat and/or UV damage to the chamber, so the upper section of the chamber wall in the vicinity of the lamp was covered with aluminum foil.

## 2. Experimental Procedure

Spectra were recorded under several conditions once the vacuum chamber apparatus was assembled. In all cases, the deuterium lamp was switched on and allowed ten minutes to warm up before any spectra were recorded. Despite the warm up period, a slow decrease in output was seen consistently during each set of recordings. Andersen (1990) attributes this decrease to an exponentially decreasing spectrograph response with a time constant of 224 seconds. The decrease in instrument response introduces an uncertainty of  $\pm 8\%$  in the calibration.

The first spectra were taken with the cover plate removed from the chamber and the apparatus open to the laboratory atmosphere. Fifteen recordings were made at atmosphere, each consisting of fifty individual spectra averaged together. The chamber was then sealed and evacuated, with an oil-sealed mechanical vacuum pump, to a pressure of approximately three torr. Power was removed from the lamp and the spectrograph during pumping, and no spectra were taken under vacuum conditions in order to avoid low-pressure arcing of high-voltage electronic components in the spectrograph.

Once the chamber was evacuated, dry, gaseous nitrogen was introduced into the chamber until it reached atmospheric pressure. Power was reapplied to the lamp and spectrograph and, after the ten-minute warm up, fifteen recordings were made. This cycle was repeated five times for a

total of six purge/fill cycles. Since one atmosphere exerts approximately 760 torr pressure, each evacuation of the chamber reduced the concentration of oxygen to 3/760 ths of atmospheric concentration. The amount of oxygen remaining in the chamber after the last cycle was estimated to be

$$\left(\frac{3}{760}\right)^6 = 4 \times 10^{-15} \quad (3.1)$$

times the oxygen concentration in the laboratory air.

While these preliminary calibration data were being studied, the apparatus was allowed to remain in the nitrogen-filled chamber at atmospheric pressure for ten days. The chamber was then evacuated and refilled with room air. Three recordings were made after the ten-minute lamp warm up and three more made after an additional 20 minutes of lamp operation. When the recording was complete, the chamber was opened, and the apparatus removed. After a week in the laboratory atmosphere, six more recordings were taken to provide a comparison of performance before and after operation in the vacuum chamber.

### 3. Results

Figure 3-2 clearly shows the increase in detector response below 2000 Å when oxygen is removed from the path. The O<sub>2</sub> absorption bands at 1972 Å, 1947 Å, 1924 Å, 1902 Å, and 1882 Å can be seen to decrease with successive evacuations of the chamber. Although the system was purged six times, the detector response did not increase noticeably after the third purge/fill cycle, at which point the chamber oxygen concentration was decreased by more than seven orders of magnitude. The system response after the third purge was used as the short-wavelength calibration standard.



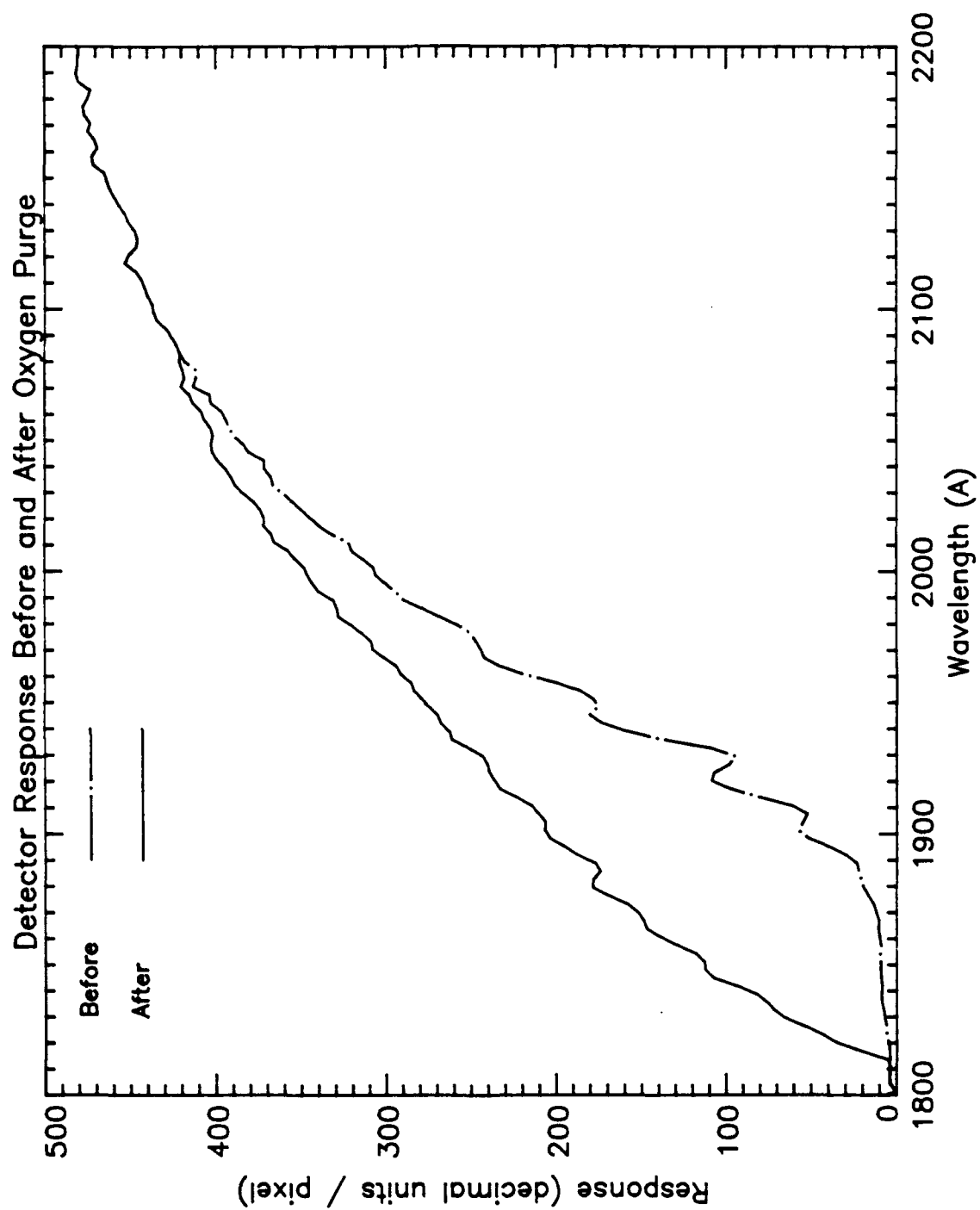


**Figure 3-2 Detector Response After Oxygen Purge**

In order to get meaningful numbers from the data, the system output must be converted to units which describe atmospheric radiation. The unit used to describe radiation is the Rayleigh, which is defined as  $10^6$  photons/cm<sup>2</sup>·sec. The system output is a voltage which is measured in decimal units (du) per pixel. Dividing this output by the absolute intensity, in Rayleighs per Angstrom (R/Å), of the deuterium irradiance standard lamp yields a calibration parameter with units of (du/pixel) per (R/Å). When the observed MUSTANG data, which have units of (du/pixel), are divided by the calibration parameter, the result is spectra with units of (R/Å). These spectra can then be integrated over wavelength to find an emitted intensity in Rayleighs.

The calibration performed in the vacuum chamber differed in the physical arrangement of the equipment from that done by Andersen(1990) in atmosphere. In the chamber, the spectrograph was placed to view the lamp directly from a distance of 1.83 m, whereas Andersen positioned the spectrograph to view a reflecting screen illuminated by the lamp from a distance of 2.00 m. In addition to the different physical arrangements, two important equipment considerations led to a decision to use the vacuum chamber results to extend Andersen's calibration rather than to create an entirely new calibration.

The first consideration is the fact that the deuterium lamp output changes with lamp age. The absolute intensity of the lamp output falls as the lamp ages, but does so fairly uniformly across the wavelength range of interest making an absolute calibration difficult, but having little effect on a relative calibration. The second consideration arises from the choice of PVC

as a vacuum chamber material. PVC pipe was chosen for the chamber because it was available quickly and inexpensively, and the chamber was not intended for use at high vacuum. Unfortunately, three days of curing and 80 hours of continuous purging still did not remove from the chamber all the volatile components of the adhesives used to seal the ends of the pipe. When the apparatus was allowed to stand in the chamber for ten days, the volatile components are believed to have formed a film on the equipment. The effect of the film can be seen in the curve labelled 'After Vacuum Chamber, Film Present' in Figure 3-3. After a week in the open laboratory, the film had evaporated and detector response at short wavelengths (pixels 0 to 92) resembled pre-vacuum-chamber response. Both the vacuum chamber calibration curve and Andersen's open-atmosphere calibration curve are shown in Figure 3-4. The curves have the same general shape, but the vacuum chamber curve displays a larger response at short wavelength than does Andersen's atmospheric curve. The increased response can be attributed to the removal of Shumann-Runge oxygen band absorption. The remainder of the vacuum calibration curve shows smaller response than Andersen's, and this is believed to be due to a decrease in the irradiance from the deuterium lamp. There is also a minor absorption peak near 2740 Å in the vacuum calibration curve which is attributed to shadowing by a small particle on the detector face.

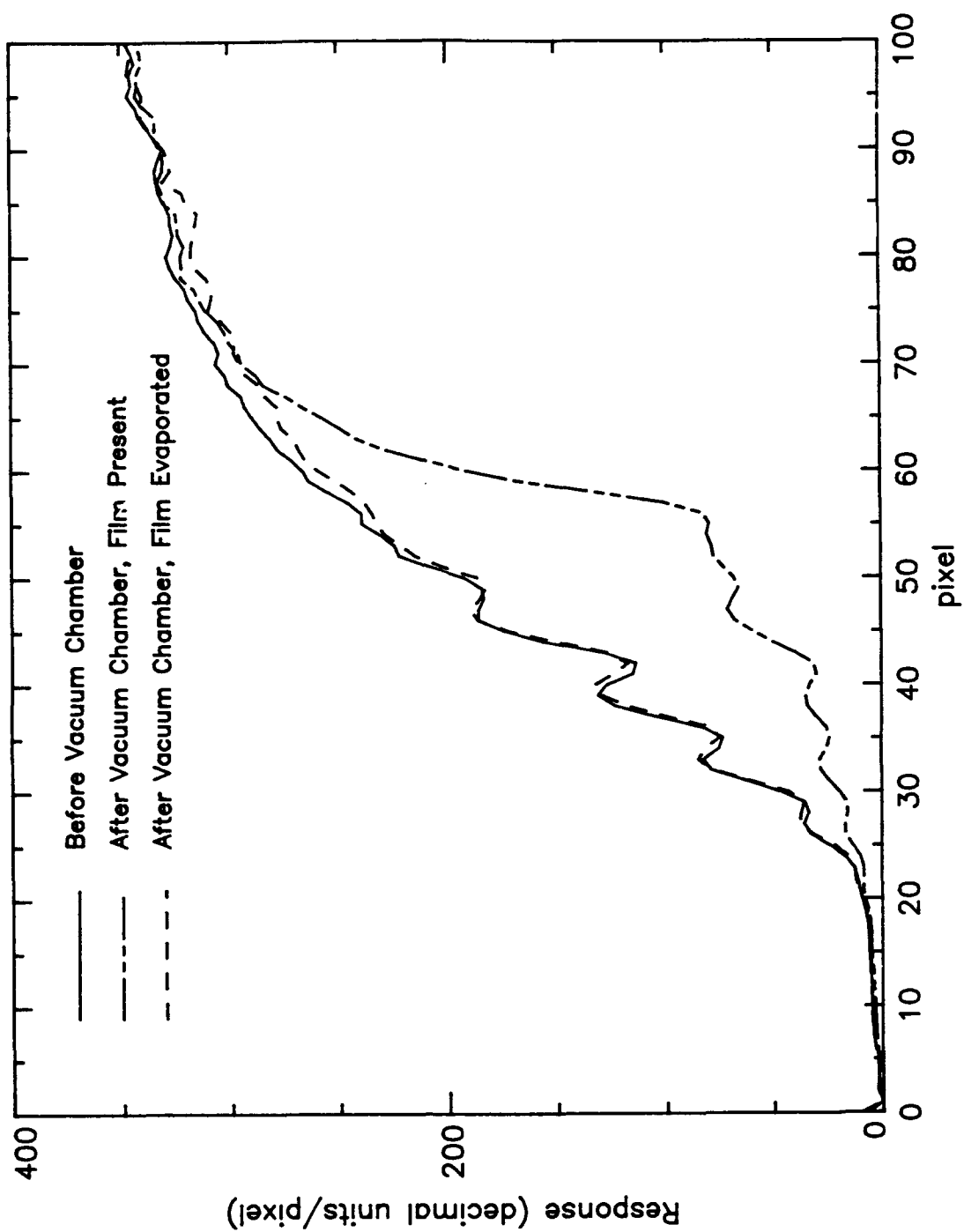
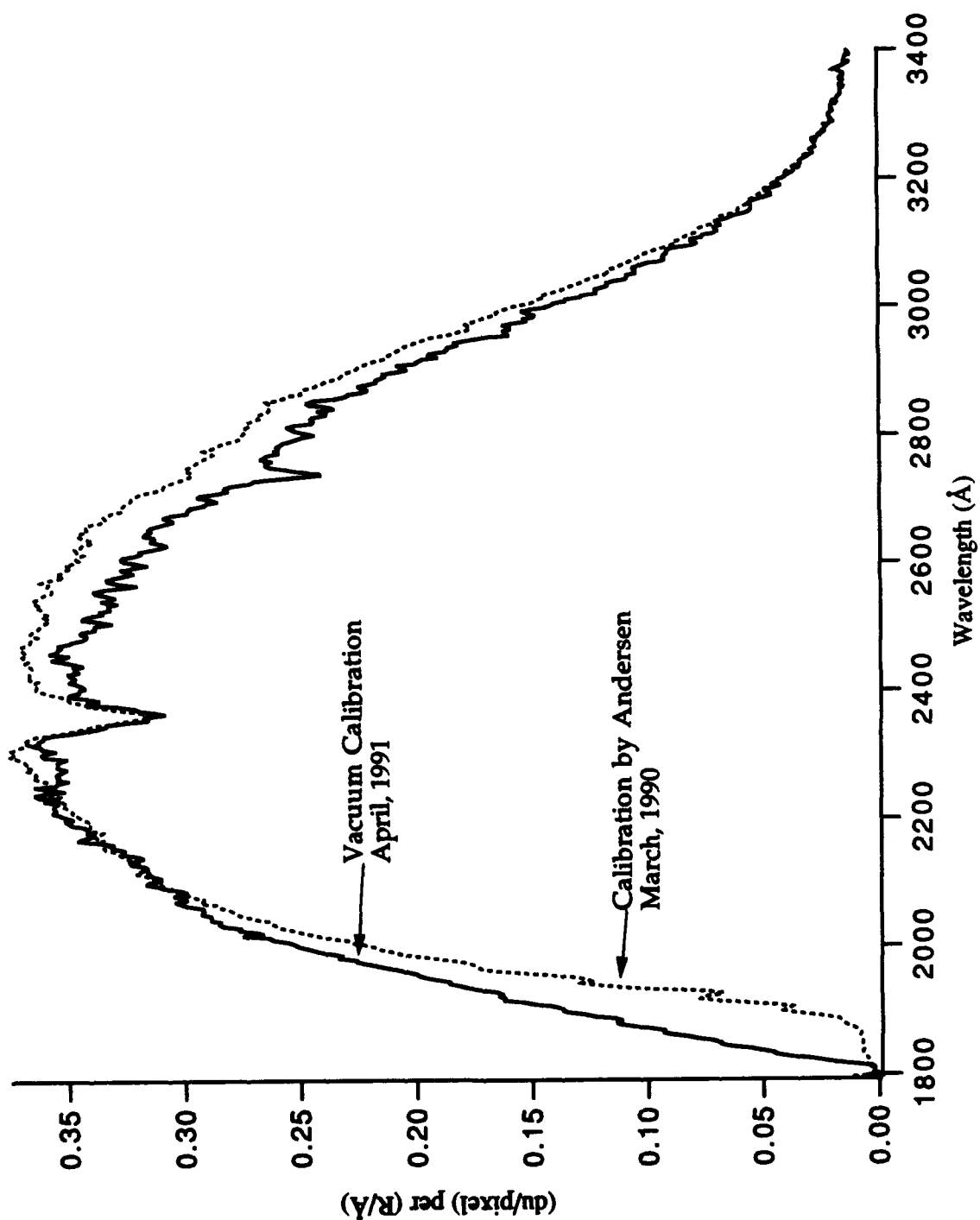


Figure 3-3 Change in Detector Response due to Film



**Figure 3-4 Comparison of Vacuum Chamber and Open Atmosphere Calibration Curves for MUSTANG**

#### IV. ANALYSIS

A total of 8400 spectra were recorded in two altitude groups: from 150 km to 320 km during ascent, and from 200 km to 100 km during descent. To facilitate their evaluation, the spectra were averaged into 25 representative spectra each corresponding to a 10 km segment of altitude. The averaged spectra are labelled with the median altitude for the segment, e.g. the spectra from 170 km to 180 km are designated the 175 km spectrum. The number of individual spectra averaged together in an altitude segment varies, because of the changing vertical speed of the rocket, from 81 at 105 km to 330 at 315 km. The resulting 25 spectra are herein modeled with synthetic spectra from which LBH column emission rate and nitric oxide density, can be inferred.

##### A. FITTING THE OBSERVED SPECTRA

During the data collection period, a defective timing signal caused the loss of every seventeenth data word from the telemetry stream. The periodic loss of data points caused a progressive shift in the recorded wavelength positions of subsequent points. The loss was corrected during initial data reduction by inserting an average value in place of each missing point and shifting the positions of the remaining points. As reported by Clayton (1990), an additional wavelength discrepancy caused the emissions from several transitions to appear at incorrect wavelengths. This discrepancy is thought to be an artifact of the telemetry circuitry, and it has been corrected by performing a cubic spline fit between the recorded wavelength data and the

theoretical wavelength curve of MUSTANG as determined by Andersen (1990). Plots of the measured peaks as a function the spline-fit wavelength data show excellent agreement with the published values of the peak wavelengths.

Having established the correct wavelength distribution for the data, synthetic spectra were generated based on temperature of the atmosphere. The temperature profile used for the synthetic spectra was determined by Clayton (1990) from his analysis of the  $\gamma(1,0)$  emission of nitric oxide. In order to account for instrument response characteristics, the synthetic spectra were convolved with the instrument slit function and multiplied by the calibration parameter described in Chapter III. Of the 512 points in each spectrum, the 72 corresponding to wavelengths 1848 Å to 2070 Å were selected for fitting the synthetic to the observed spectra. The spectrum in this wavelength region is composed of four emissions as shown in Figure 4-1. Fitting was done using a parameter space grid search adapted by Clayton (1990) from Bevington (1969). The parameters included in the search were LBH intensity, the sum of the  $\gamma$ ,  $\delta$ , and  $\epsilon$  intensities from NO, and a constant background term. The background term was included to account for scattering into the line of sight from the bright portion of the atmosphere below the instrument. The background component is omitted from Figure 4-1 for the sake of clarity. Goodness of fit was determined by minimizing the value of  $\chi^2$  between the observed spectrum and the sum of the synthetic terms. The results of the fitting are shown in Figures 4-2 to 4-26.

The effect of an exponentially decreasing density is easily seen in the fits. The intensity of the emissions varies from nearly 1500 R/Å at 105 km to less

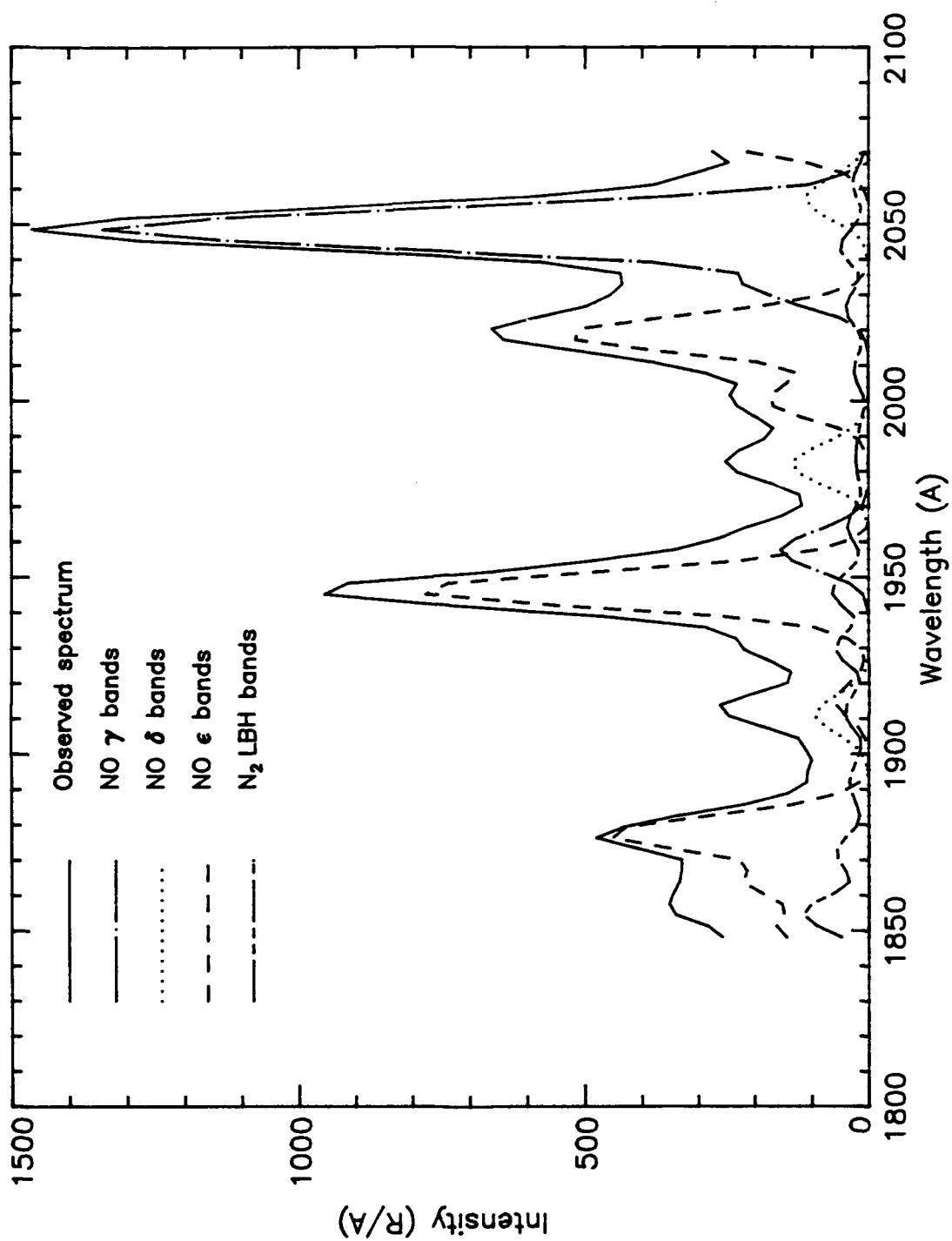


Figure 4-1 Spectral Components



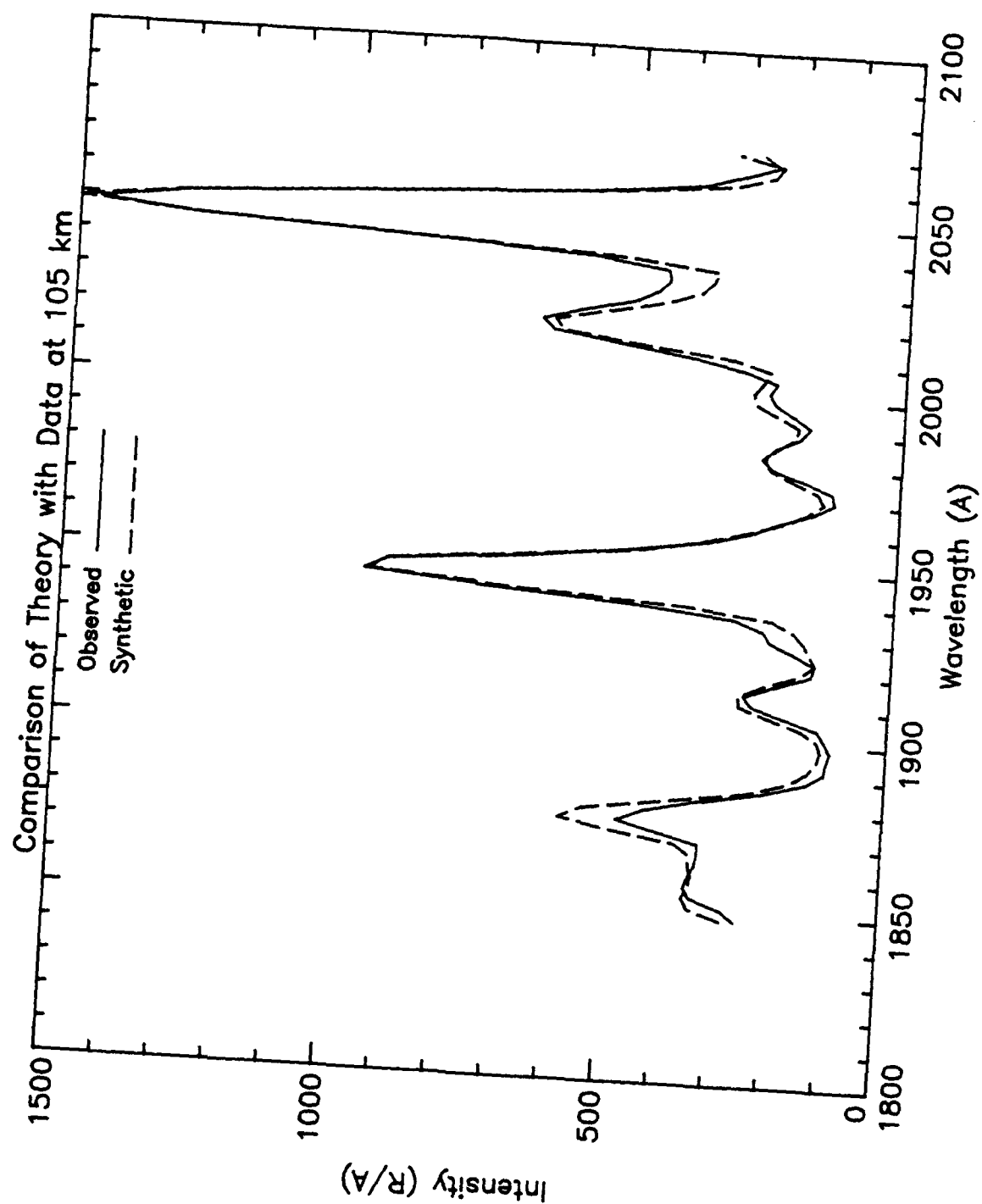


Figure 4-2 Comparison of Synthetic and Observed Spectra at 105 km

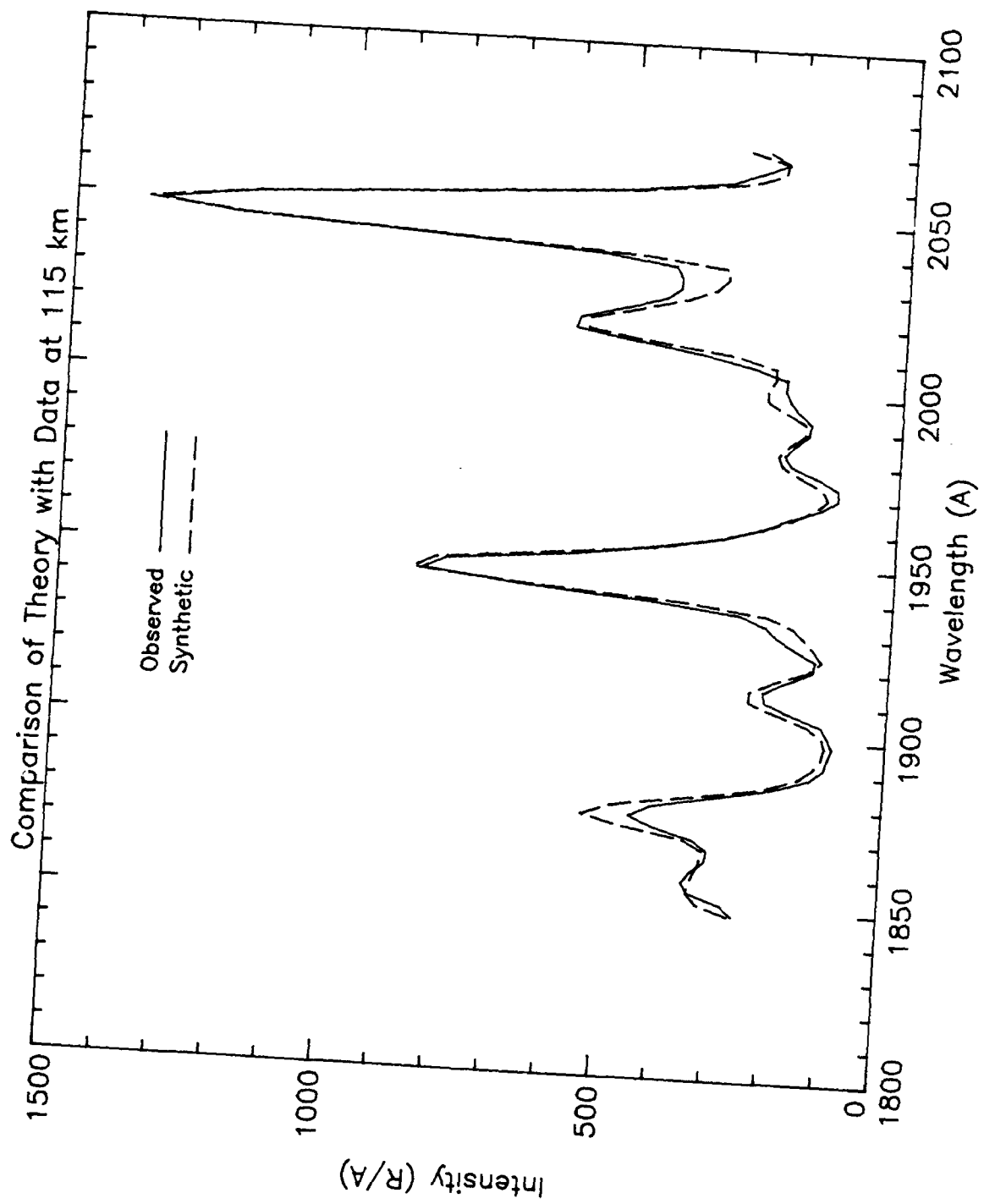


Figure 4-3 Comparison of Synthetic and Observed Spectra at 115 km

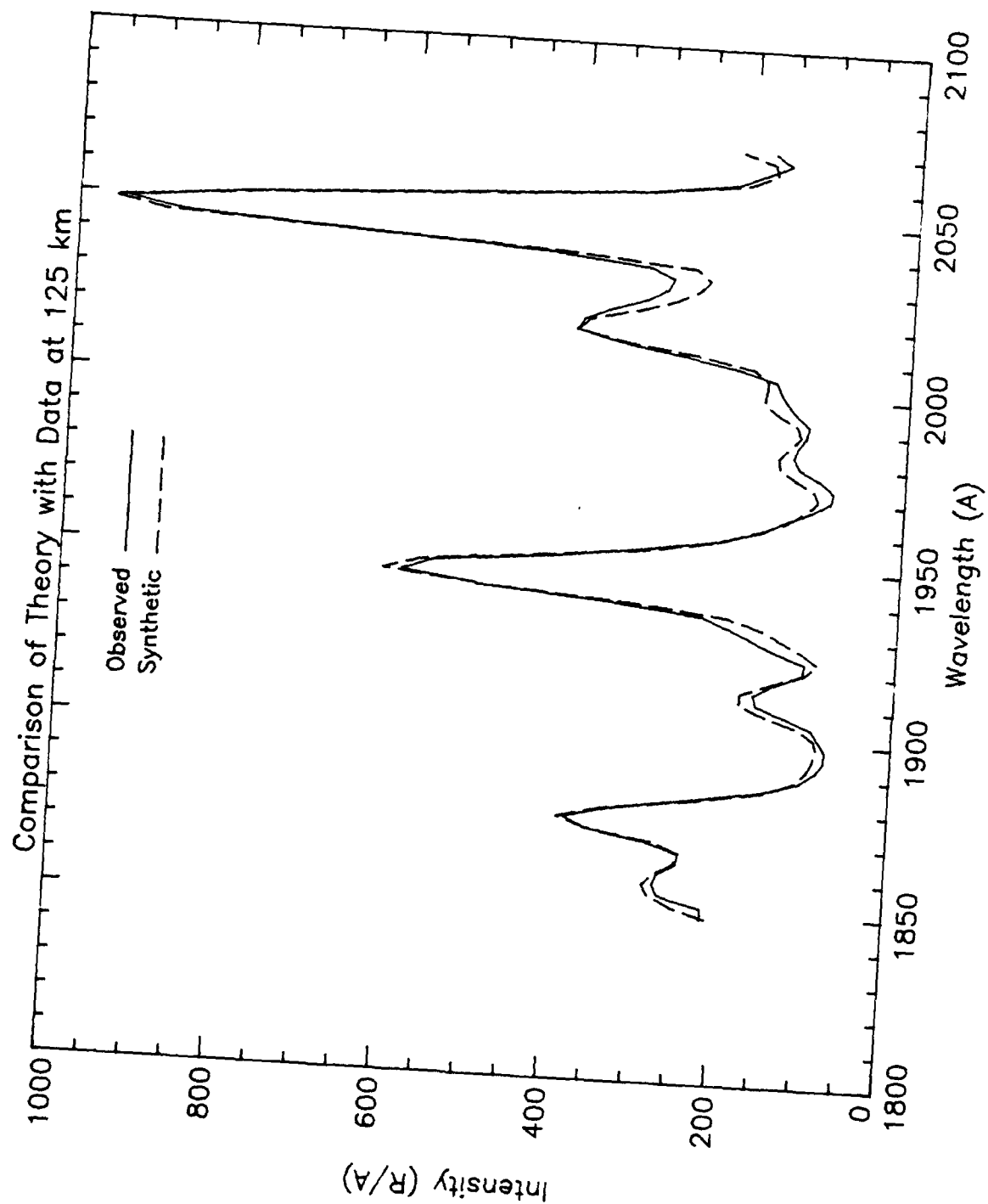
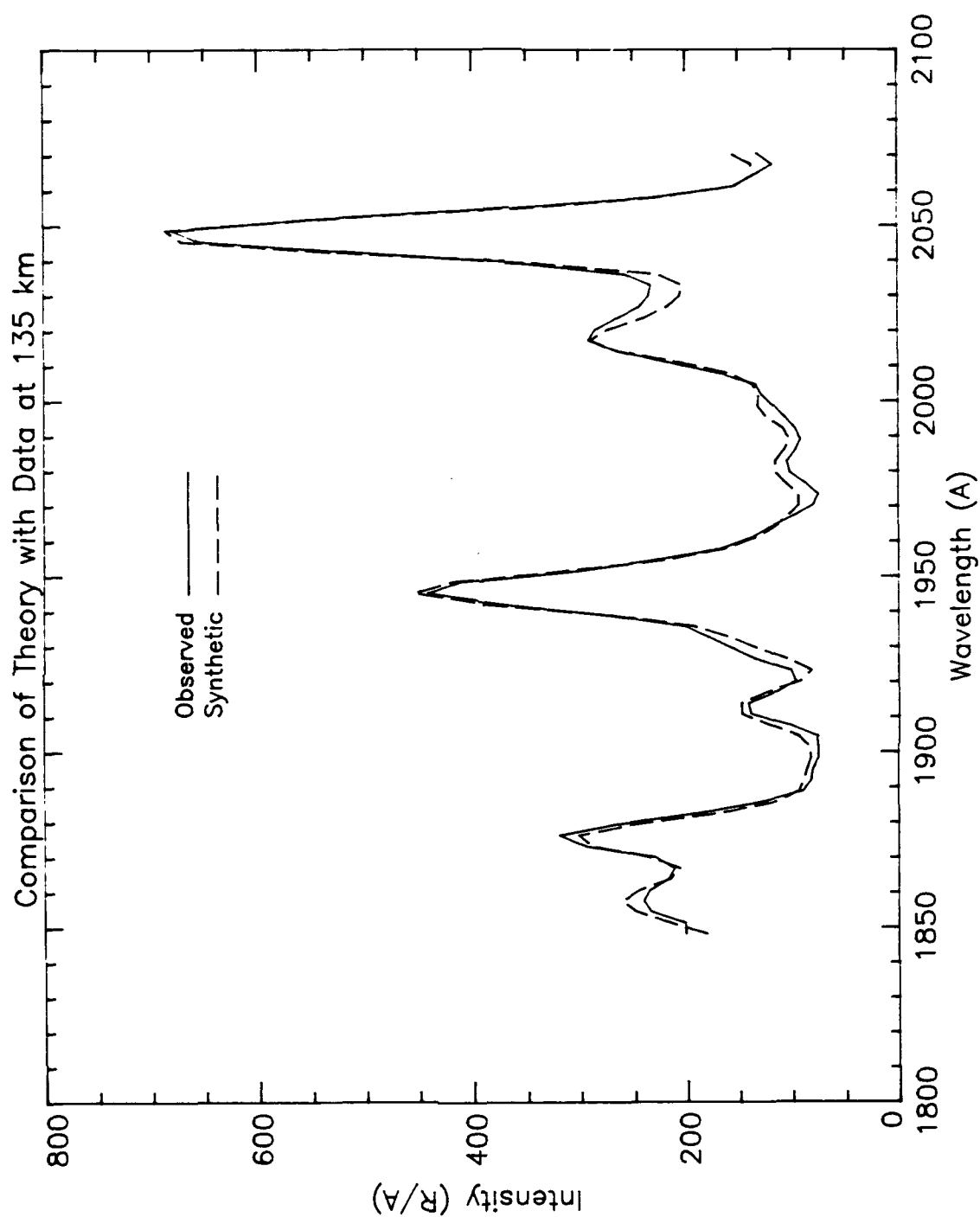
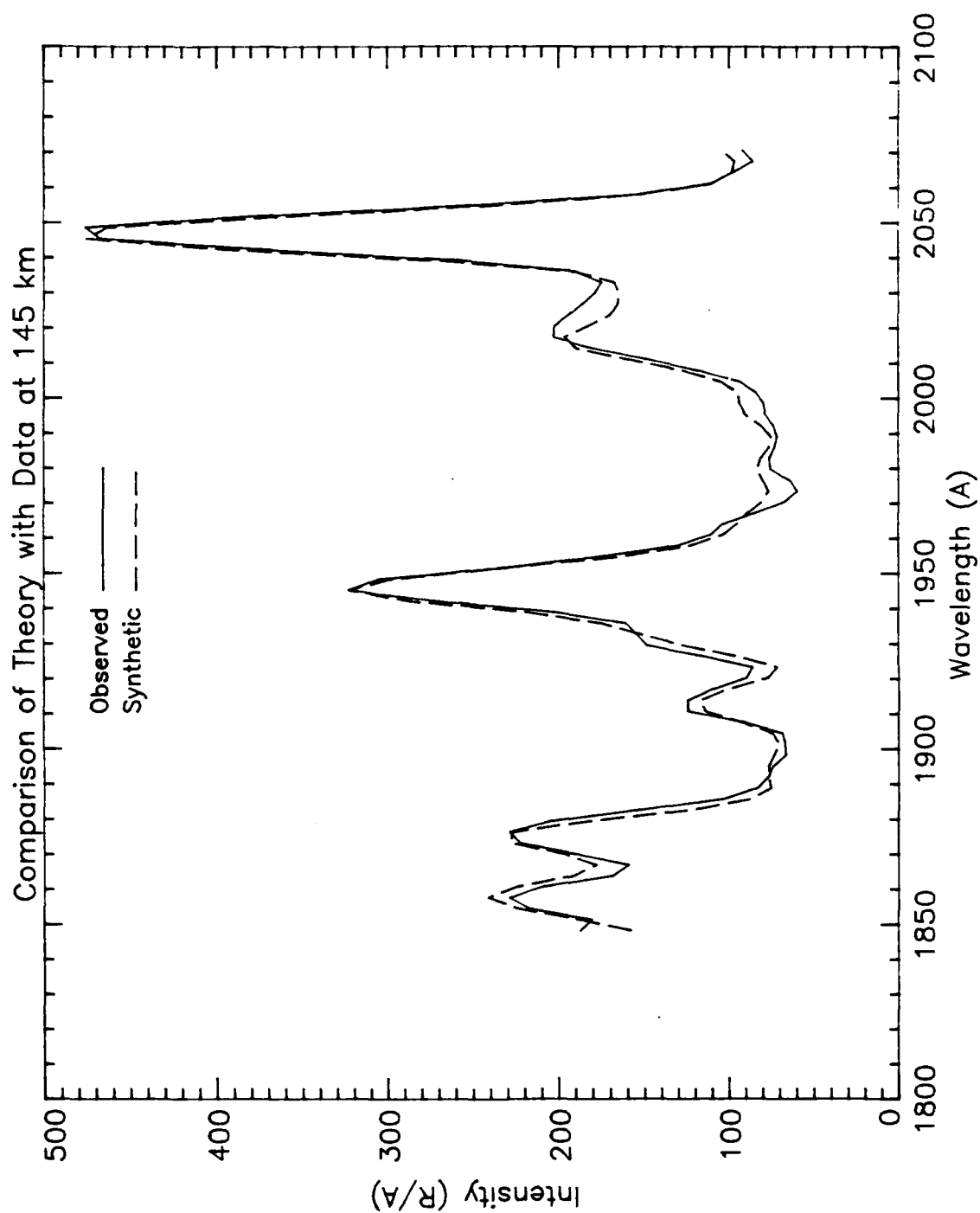


Figure 4-4 Comparison of Synthetic and Observed Spectra at 125 km



**Figure 4-5 Comparison of Synthetic and Observed Spectra at 135 km**



**Figure 4-6 Comparison of Synthetic and Observed Spectra at 145 km**

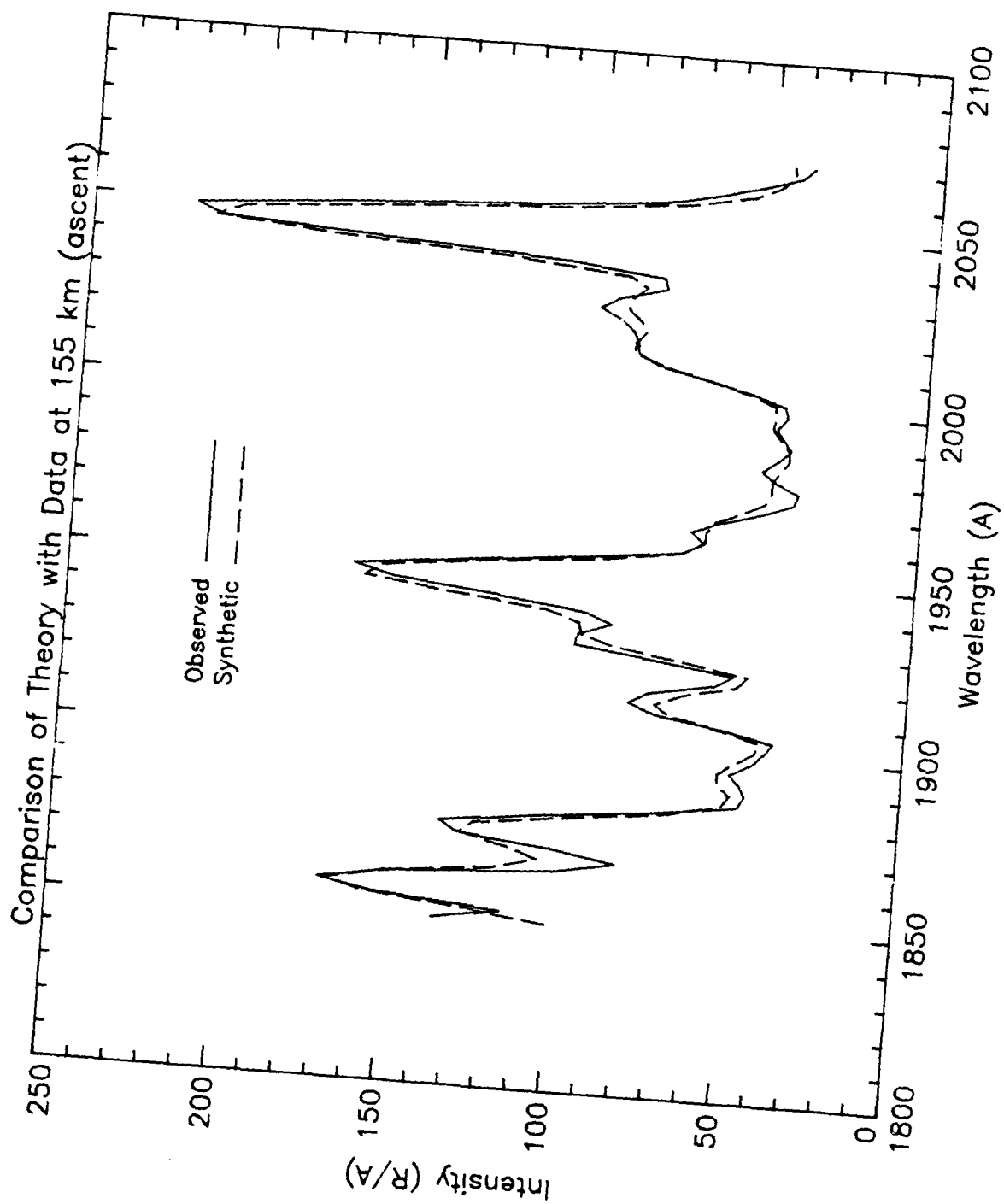


Figure 4-7 Comparison of Synthetic and Observed Spectra at 155 km (ascent)

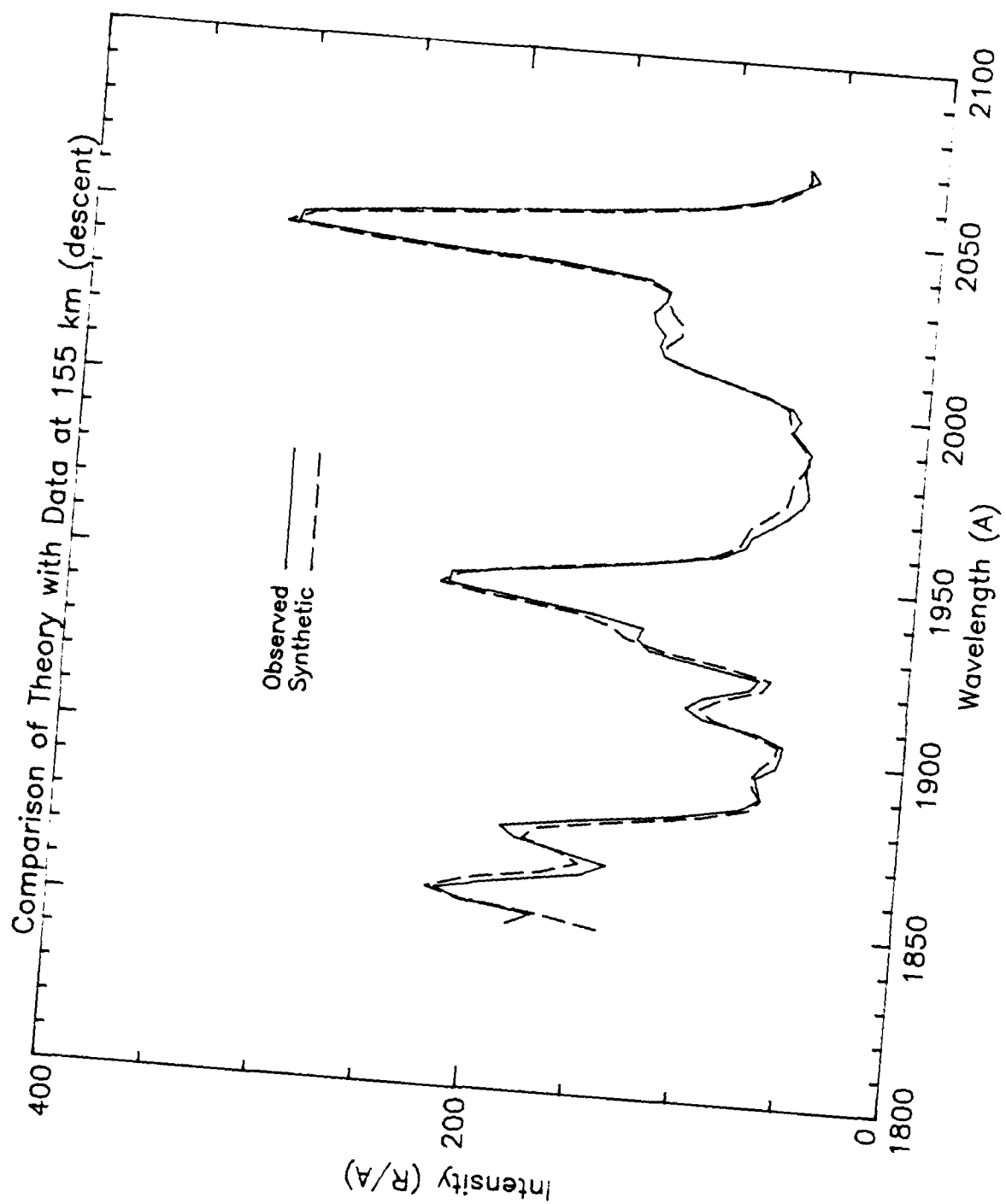
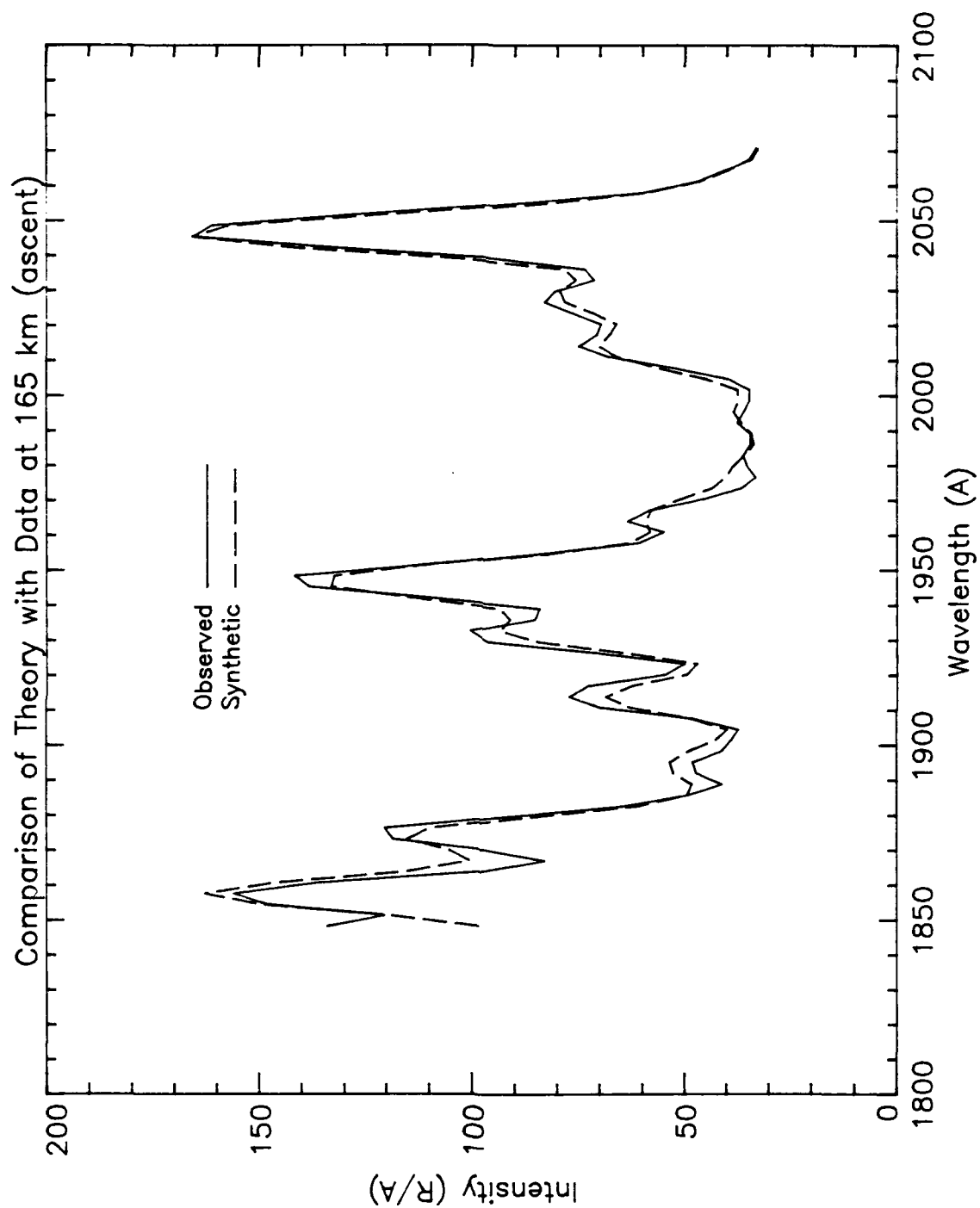
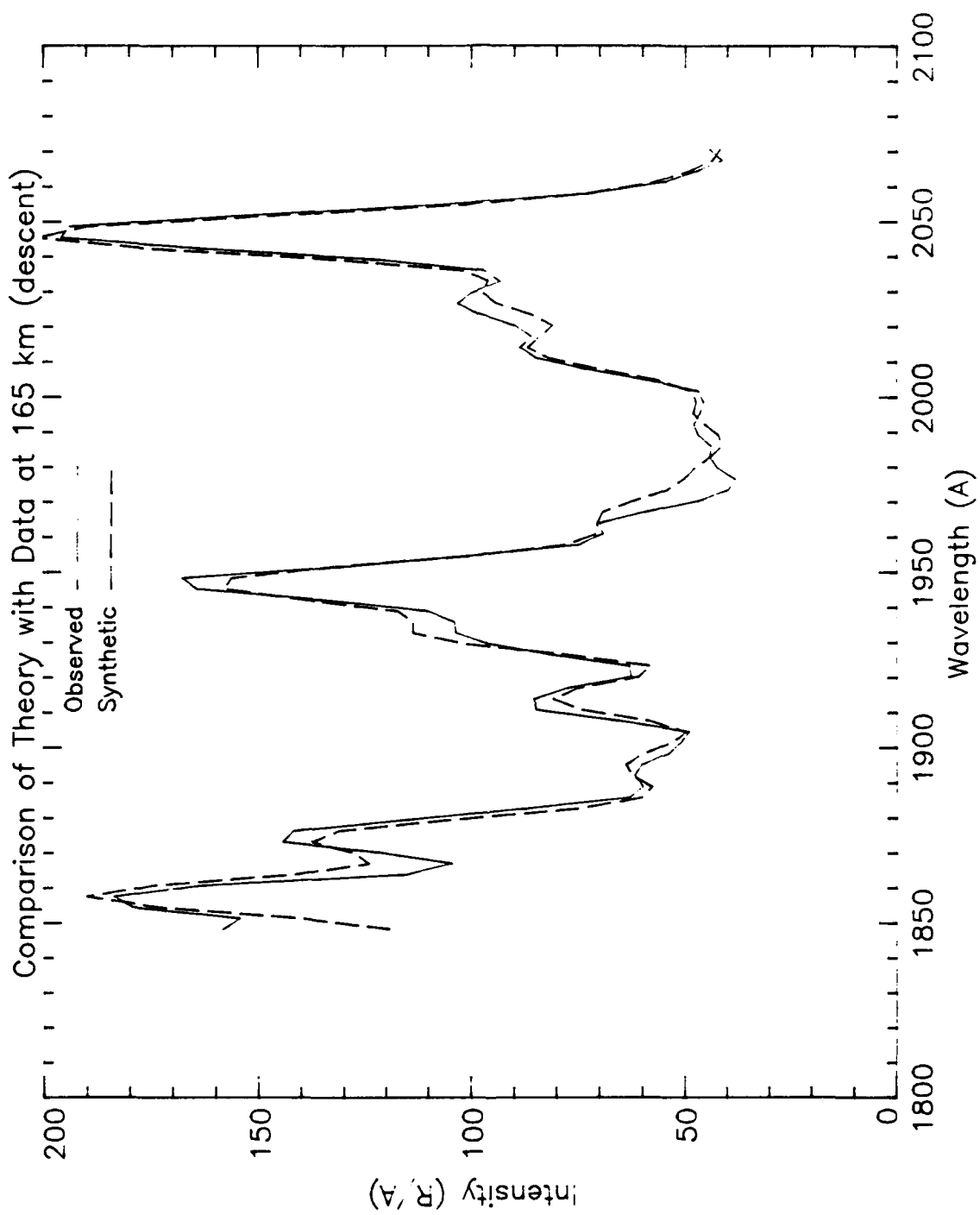


Figure 4-8 Comparison of Synthetic and Observed Spectra at 155 km (descent)



**Figure 4-9** Comparison of Synthetic and Observed Spectra at 165 km (ascent)





**Figure 4-10 Comparison of Synthetic and Observed Spectra at 165 km (descent)**

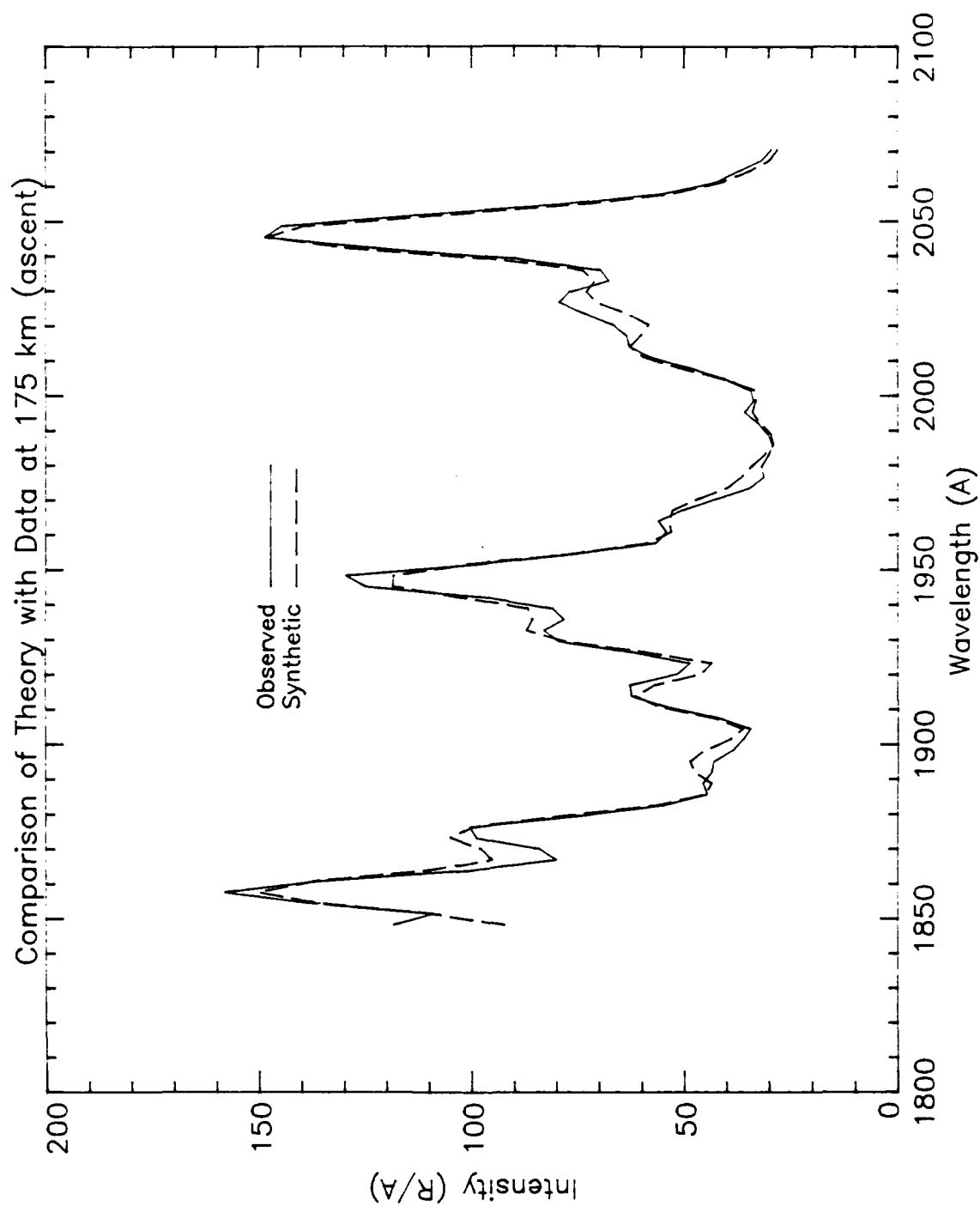
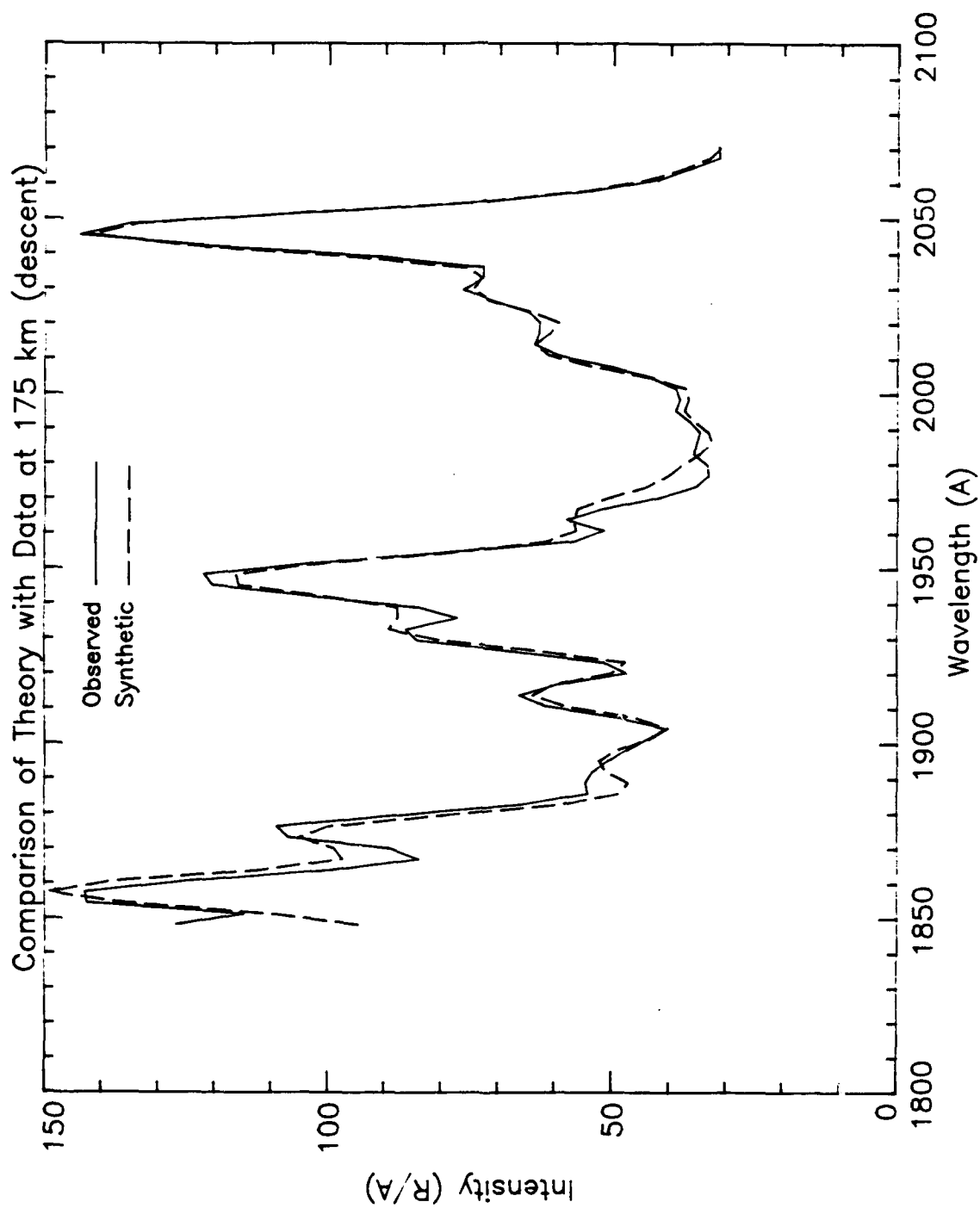


Figure 4-11 Comparison of Synthetic and Observed Spectra at 175 km (ascent)



**Figure 4-12** Comparison of Synthetic and Observed Spectra at 175 km (descent)

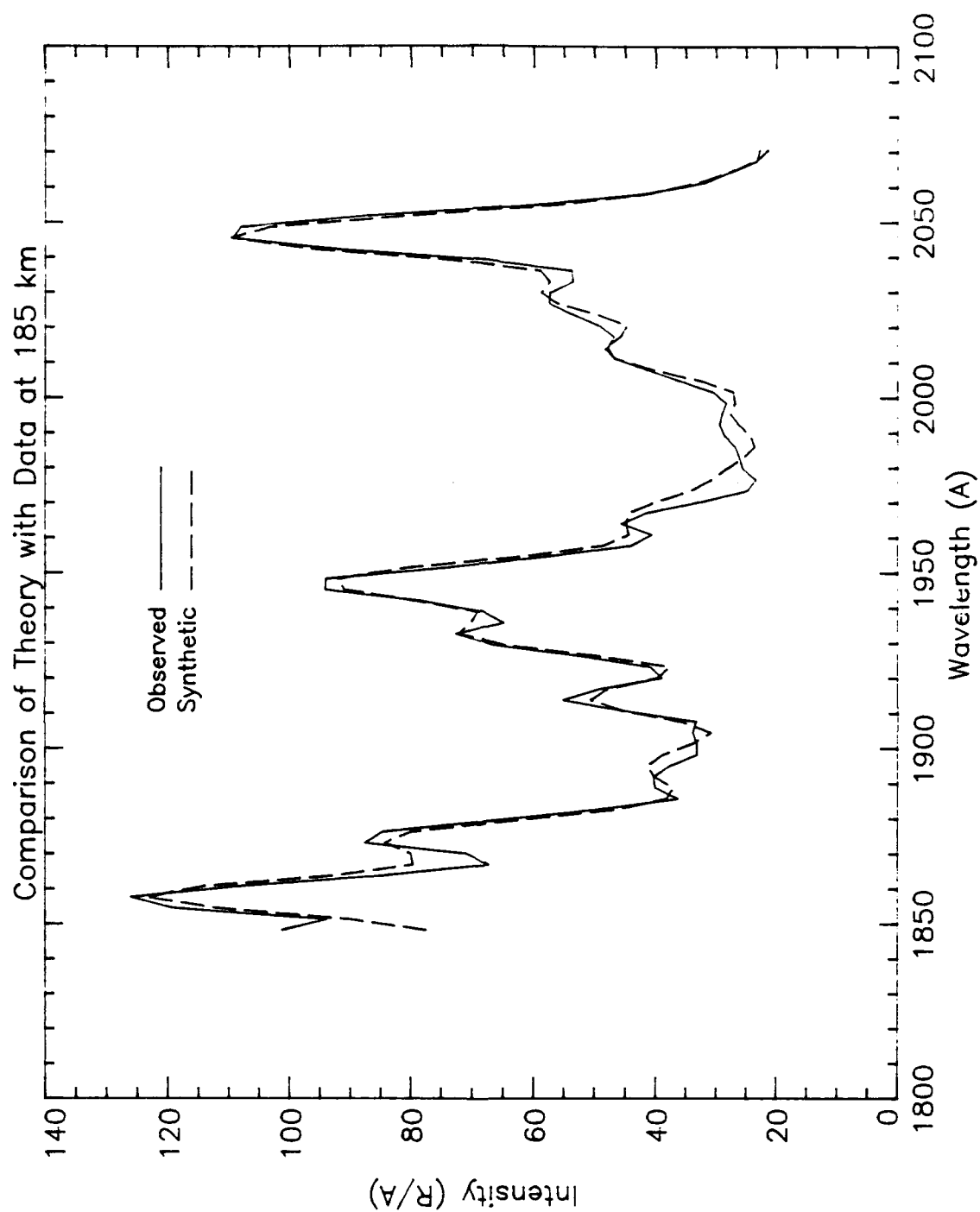


Figure 4-13 Comparison of Synthetic and Observed Spectra at 185 km

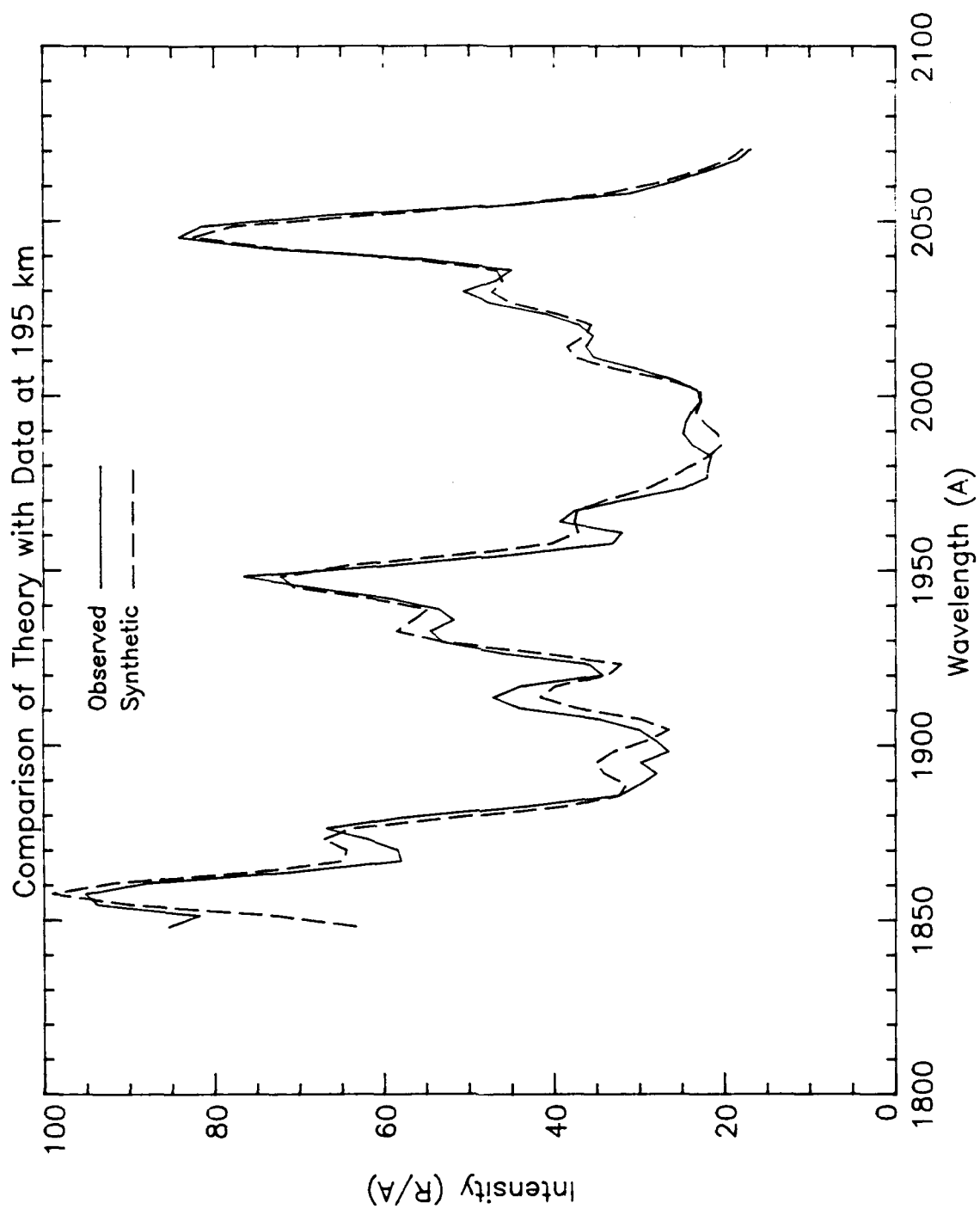


Figure 4-14 Comparison of Synthetic and Observed Spectra at 195 km

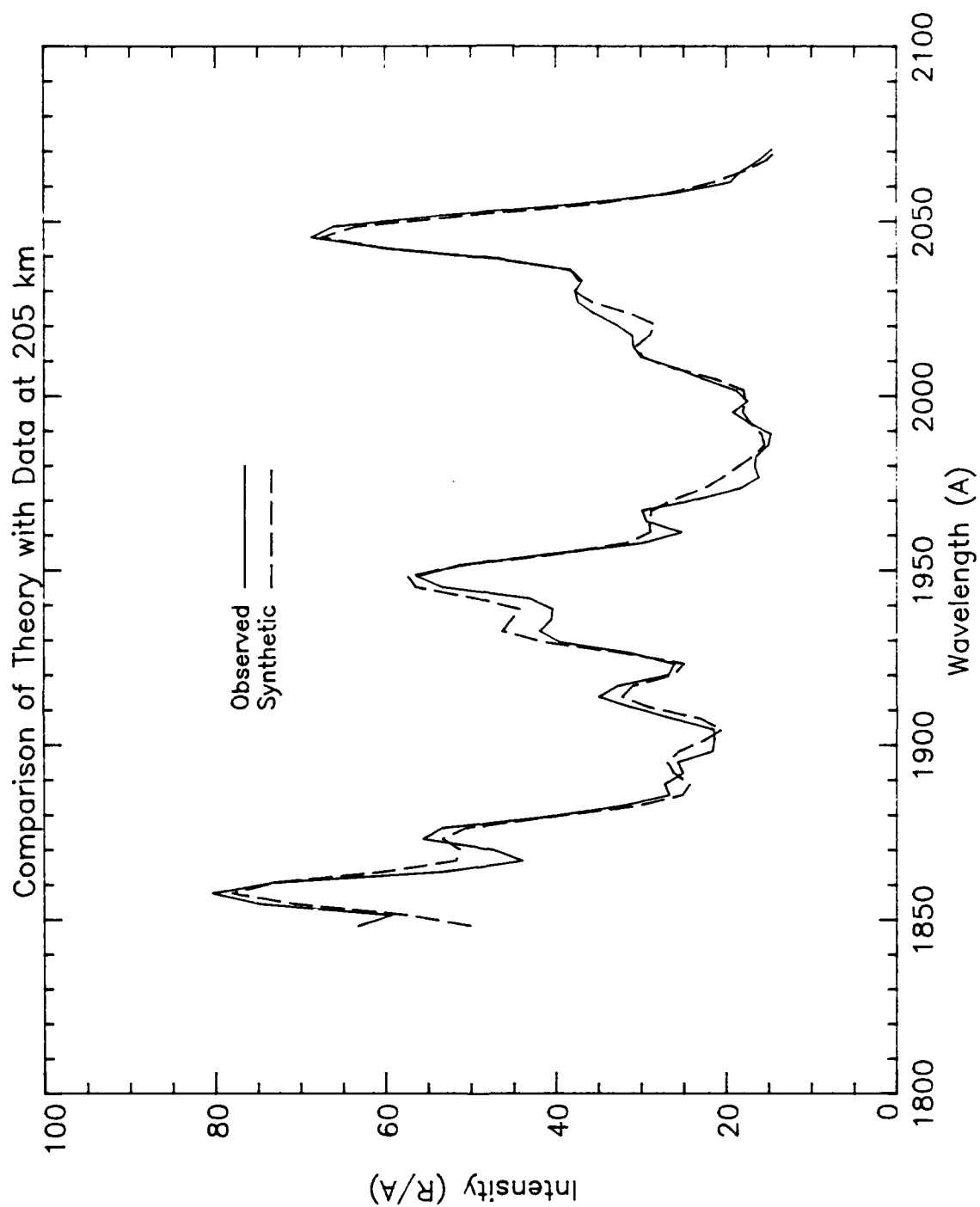


Figure 4-15 Comparison of Synthetic and Observed Spectra at 205 km

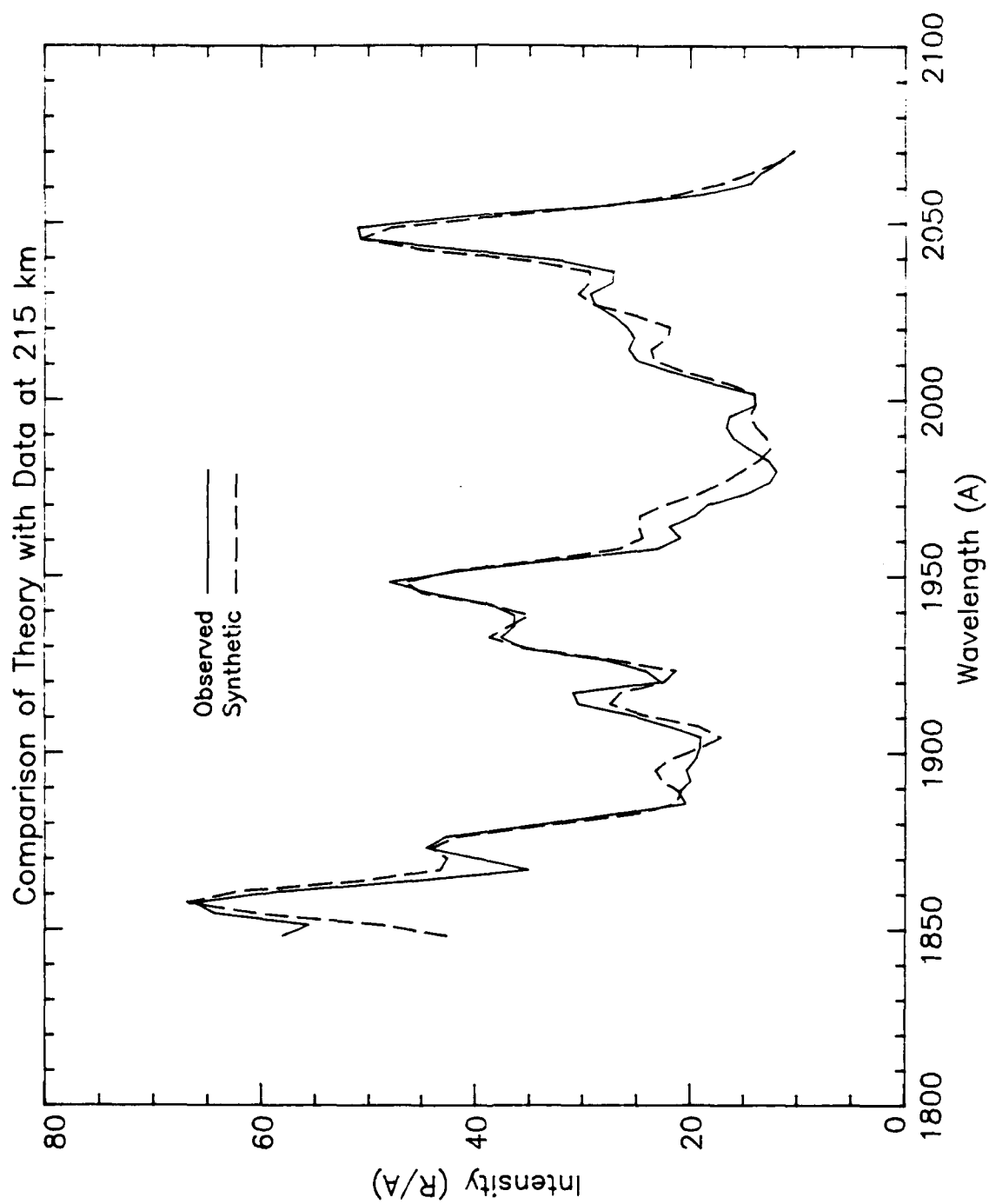


Figure 4-16 Comparison of Synthetic and Observed Spectra at 215 km

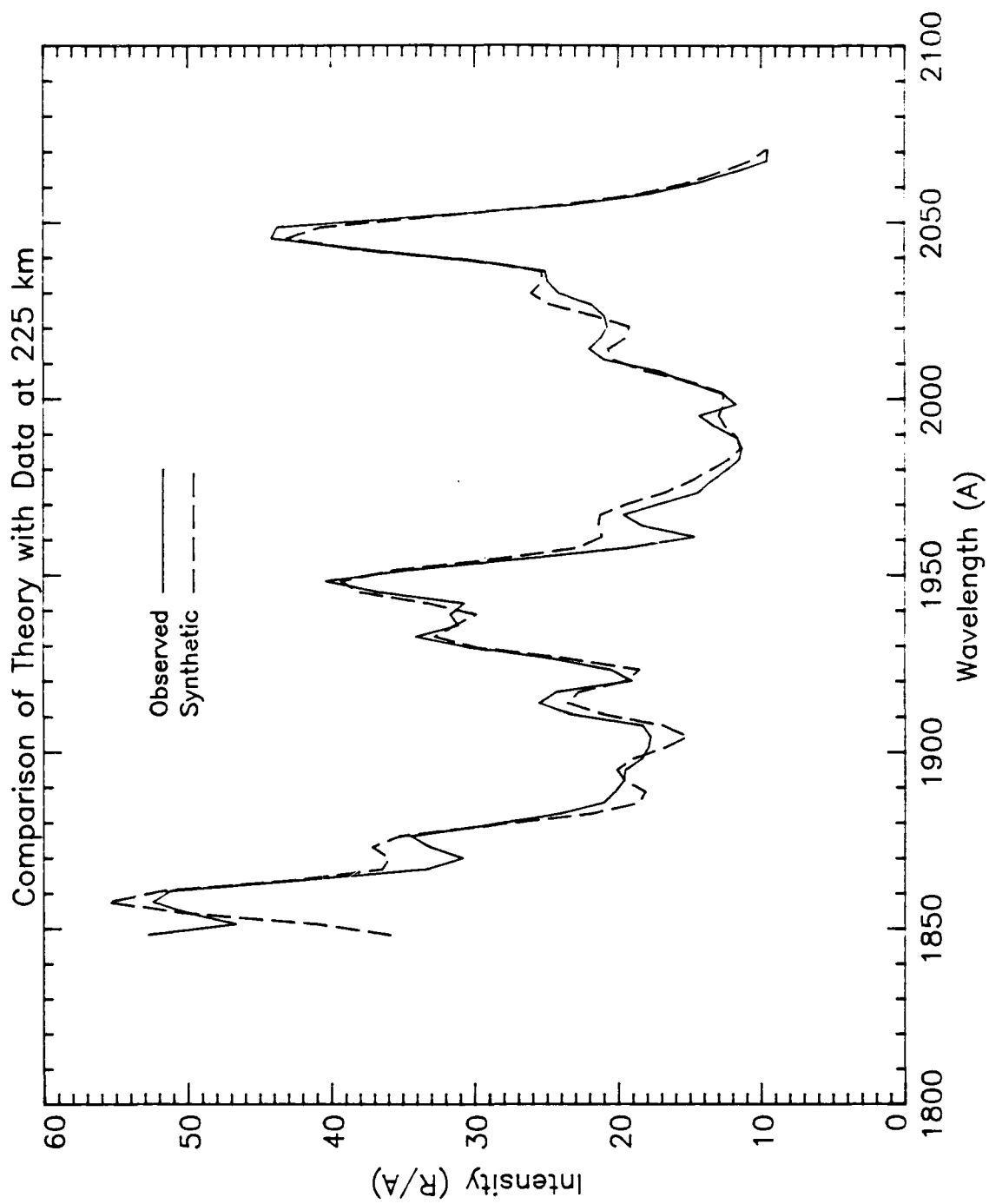


Figure 4-17 Comparison of Synthetic and Observed Spectra at 225 km



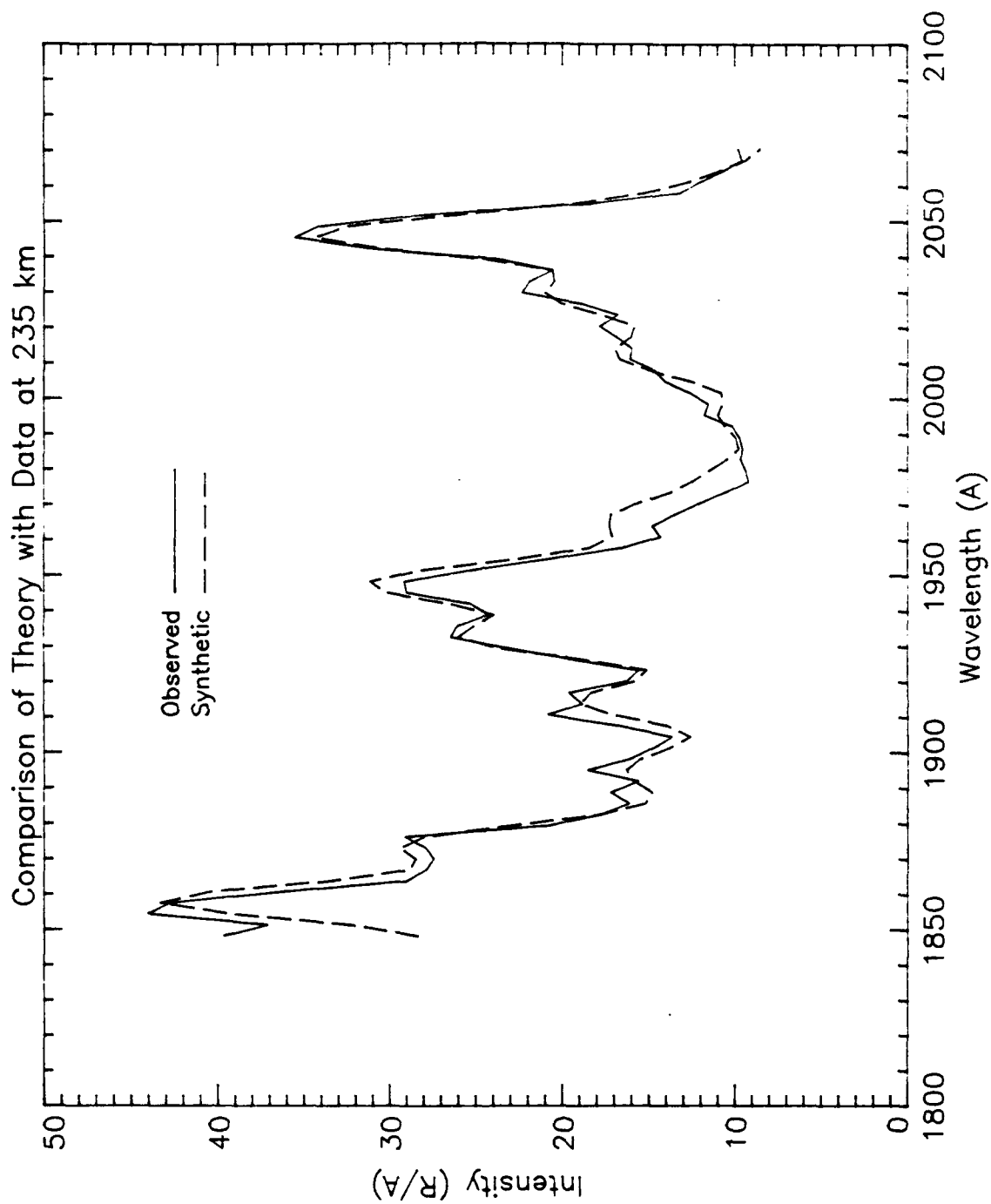


Figure 4-18 Comparison of Synthetic and Observed Spectra at 235 km

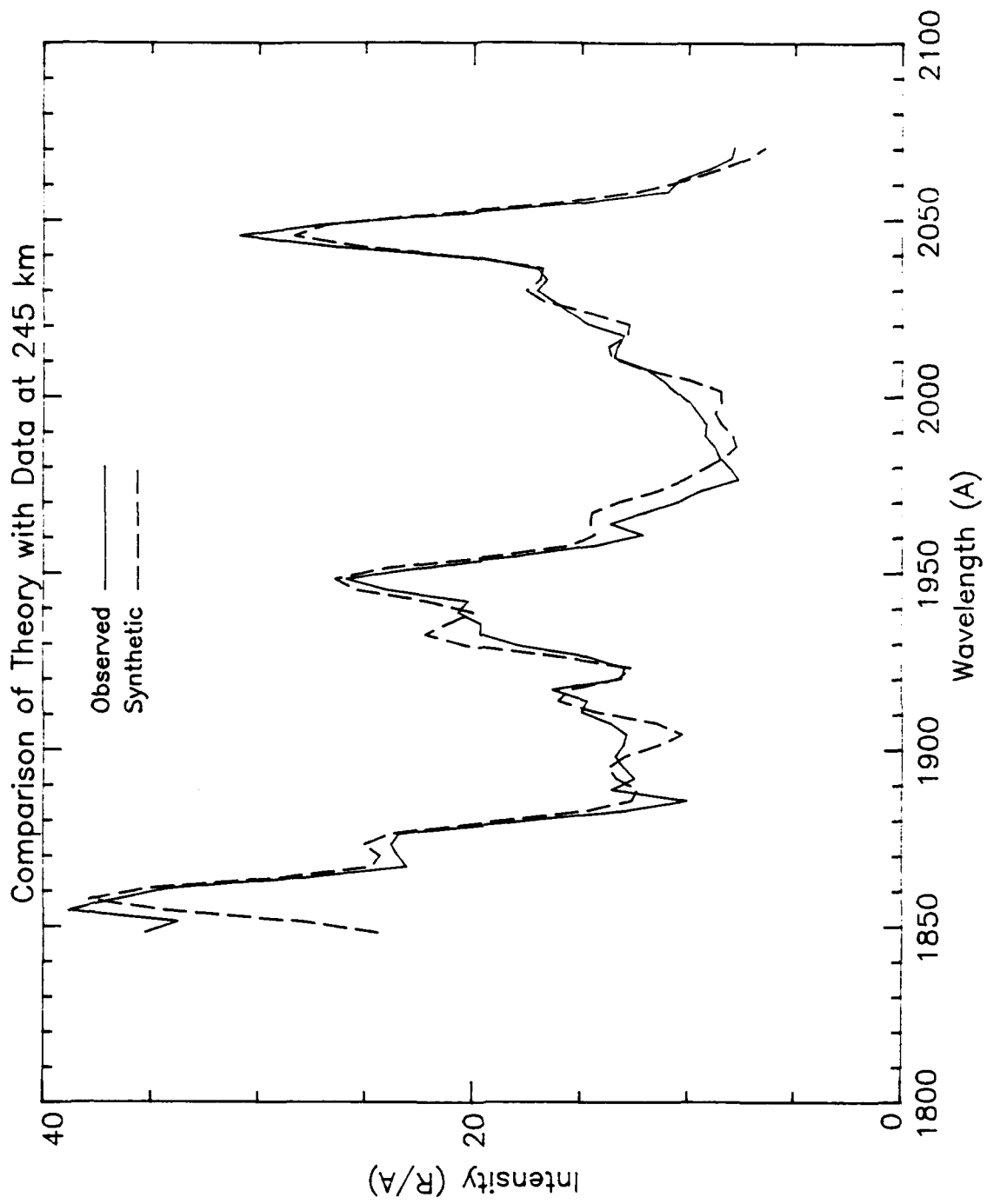


Figure 4-19 Comparison of Synthetic and Observed Spectra at 245 km

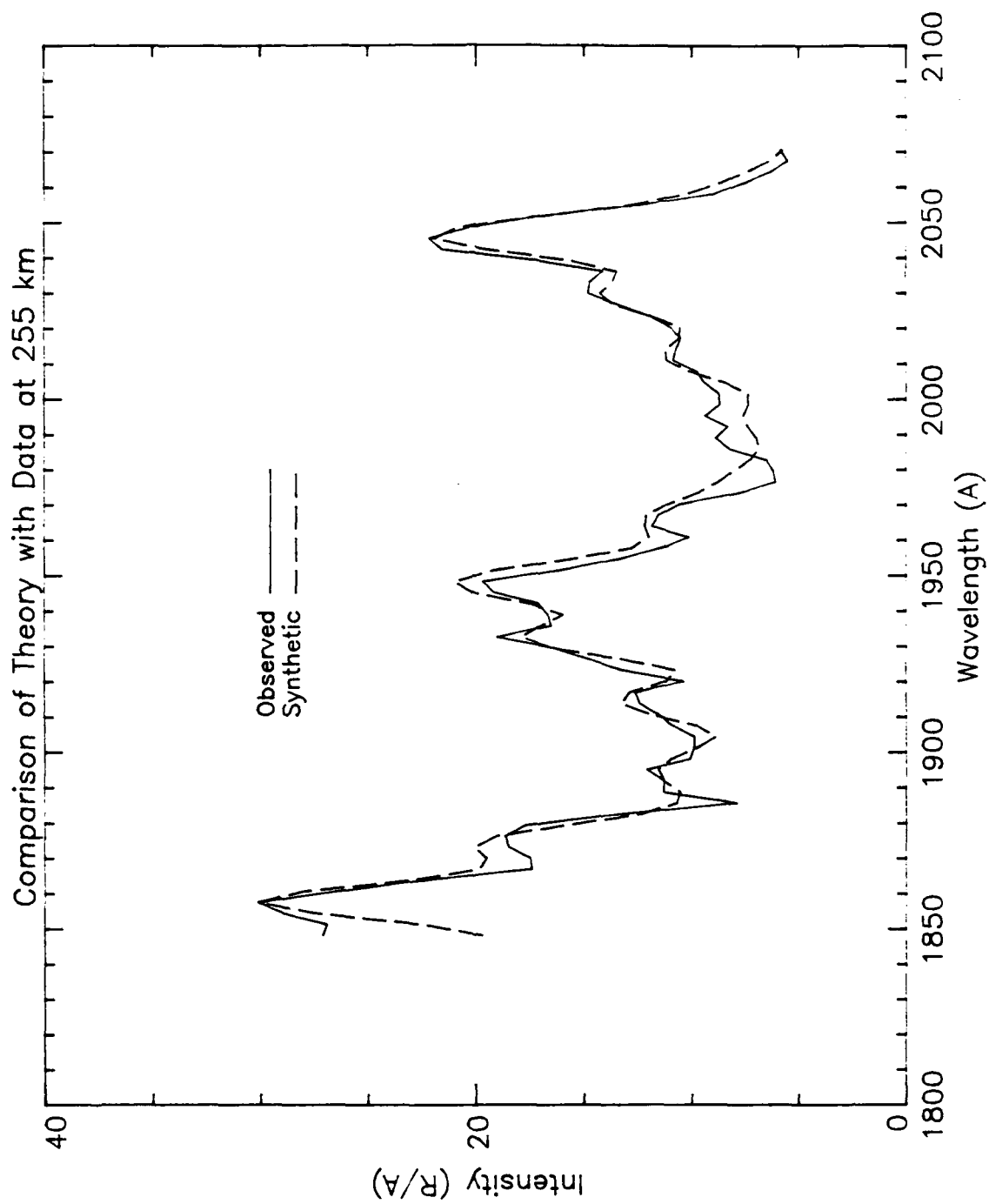


Figure 4-20 Comparison of Synthetic and Observed Spectra at 255 km

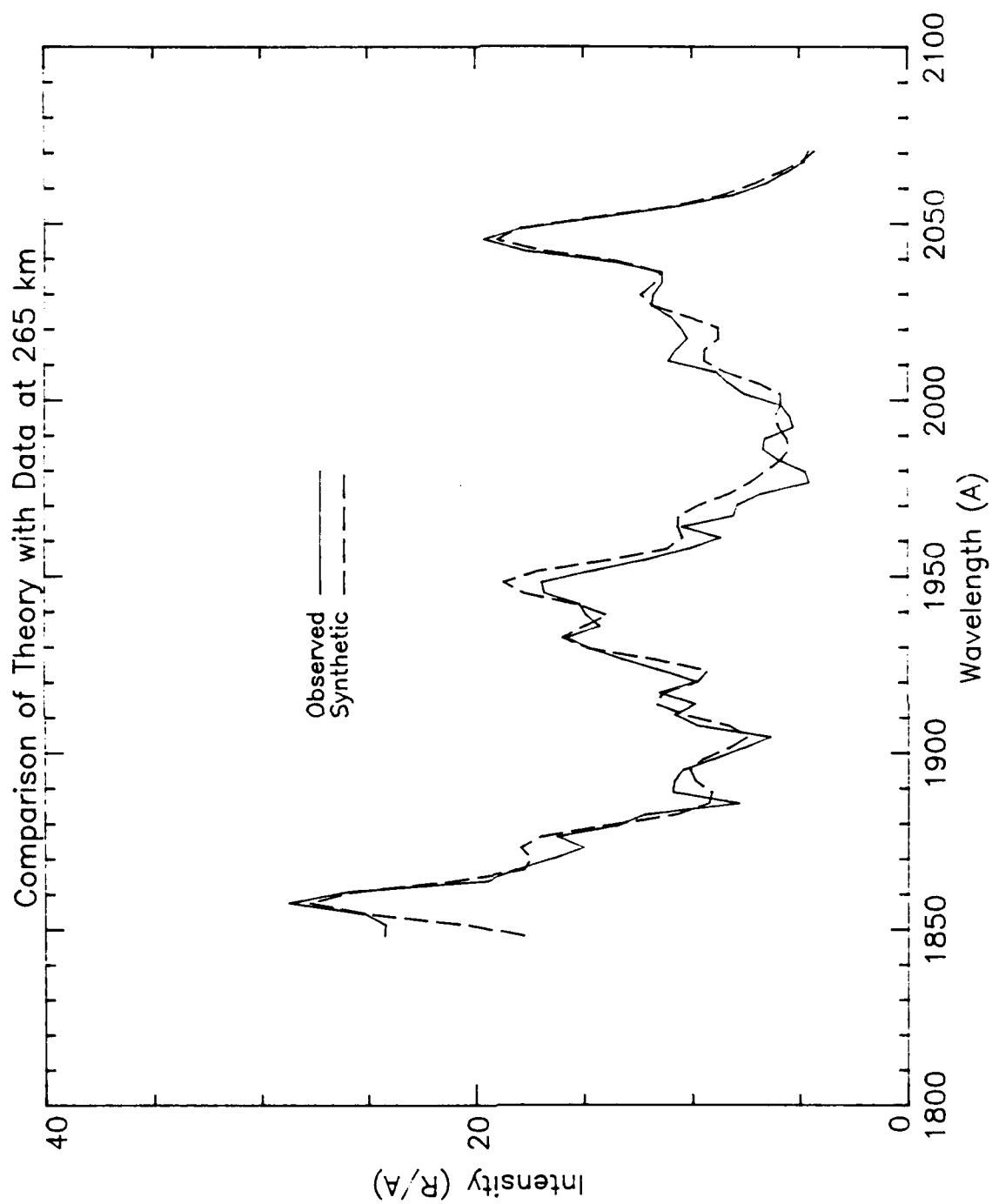


Figure 4-21 Comparison of Synthetic and Observed Spectra at 265 km

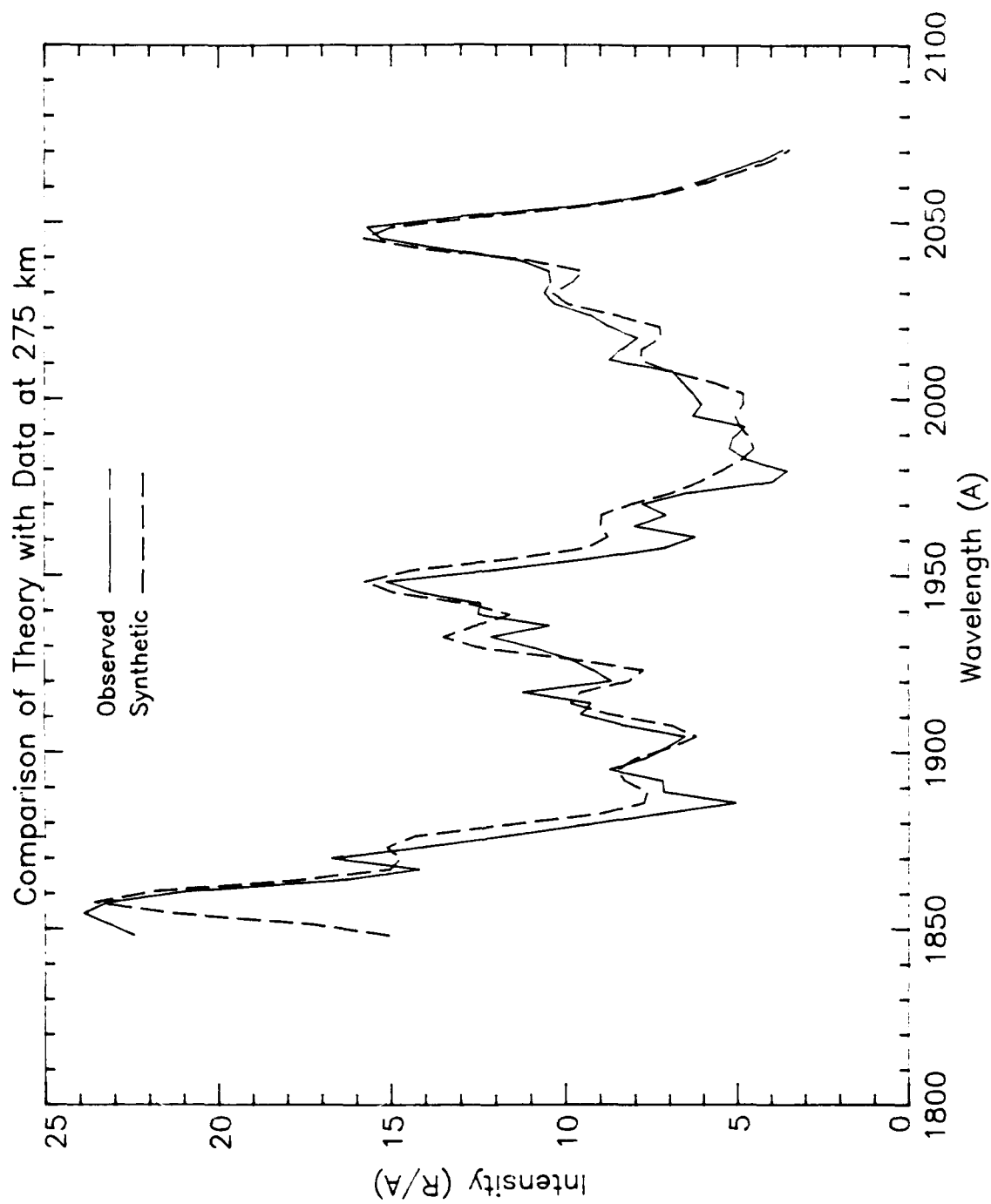
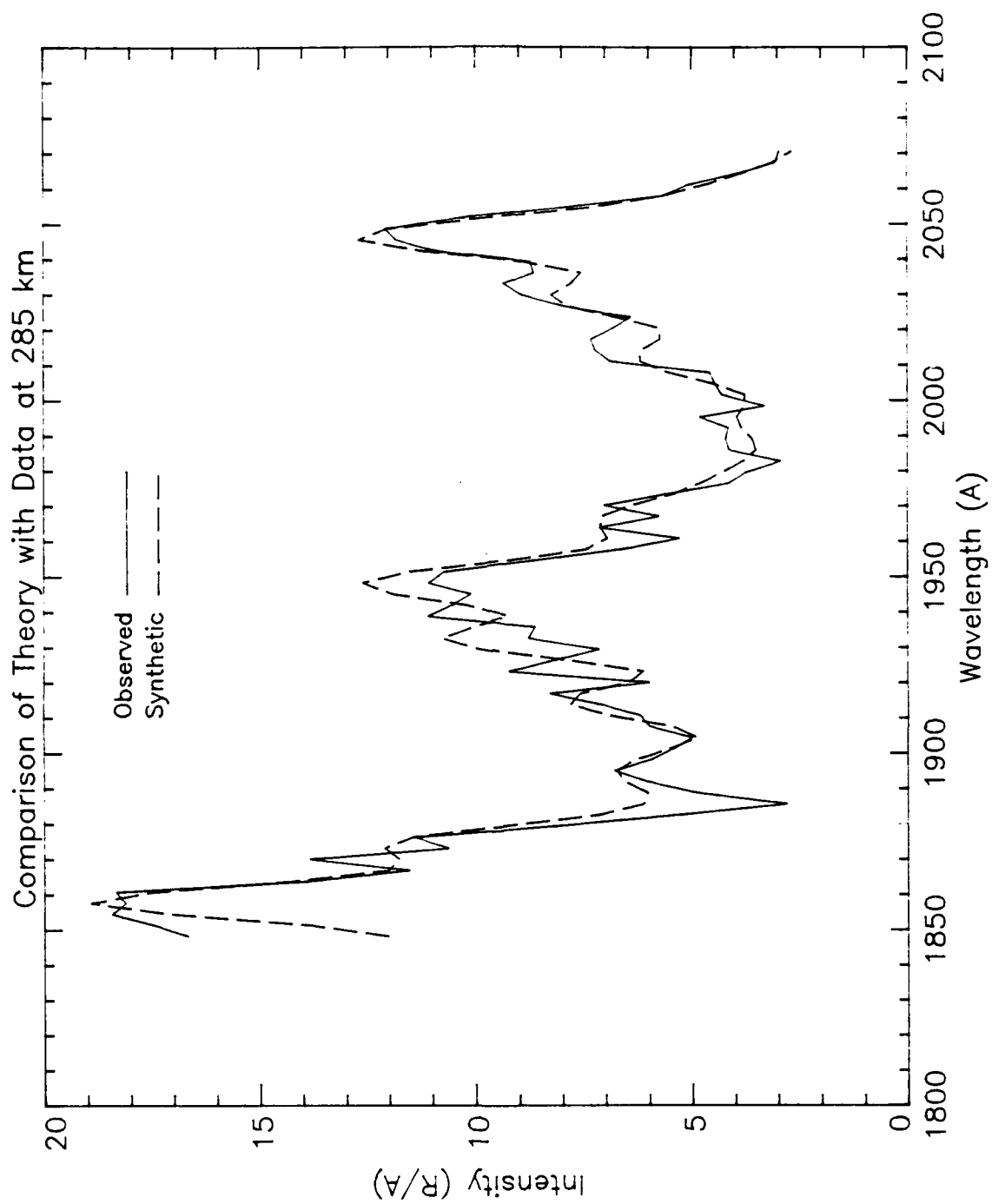


Figure 4-22 Comparison of Synthetic and Observed Spectra at 275 km



**Figure 4-23** Comparison of Synthetic and Observed Spectra at 285 km

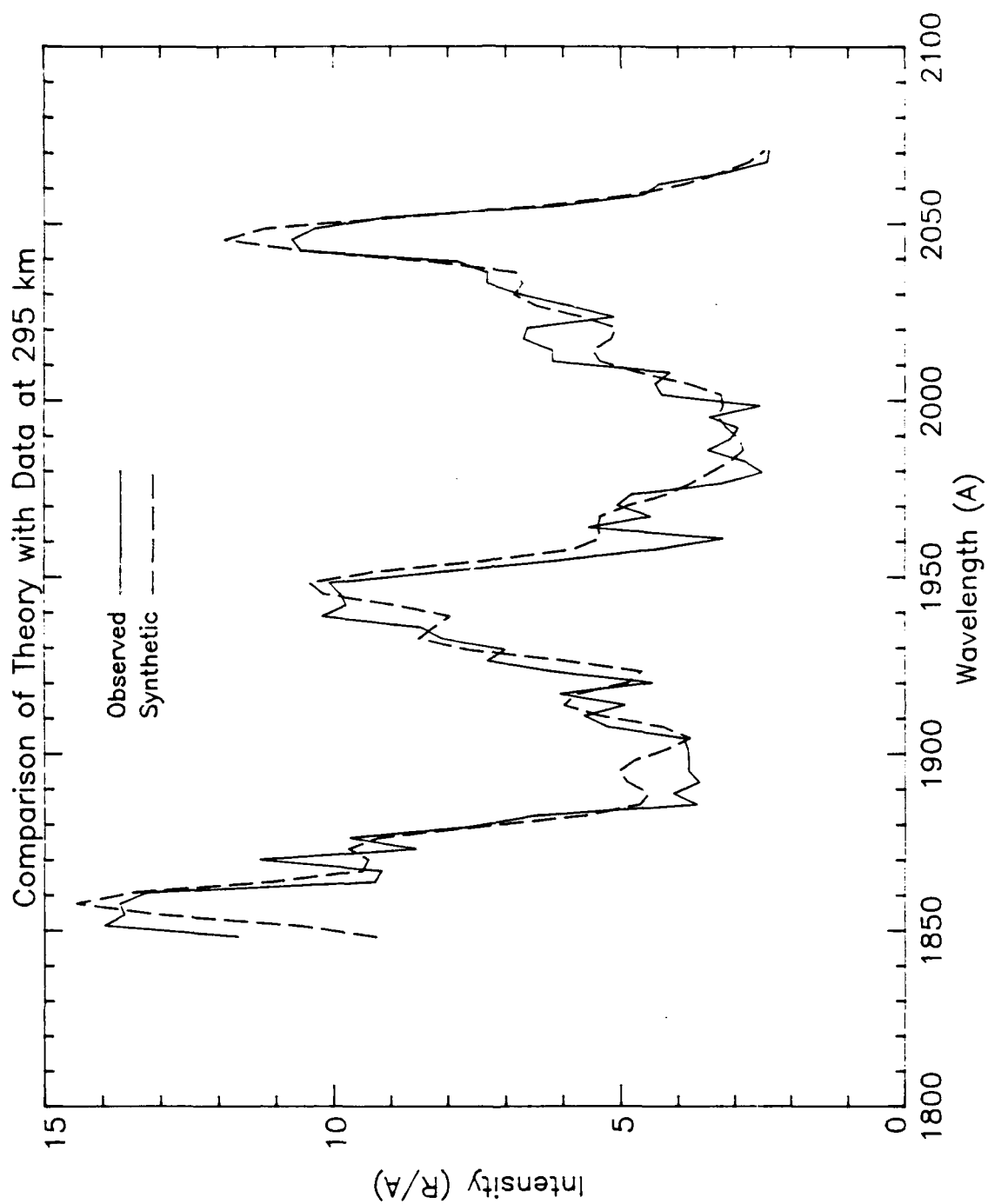


Figure 4-24 Comparison of Synthetic and Observed Spectra at 295 km

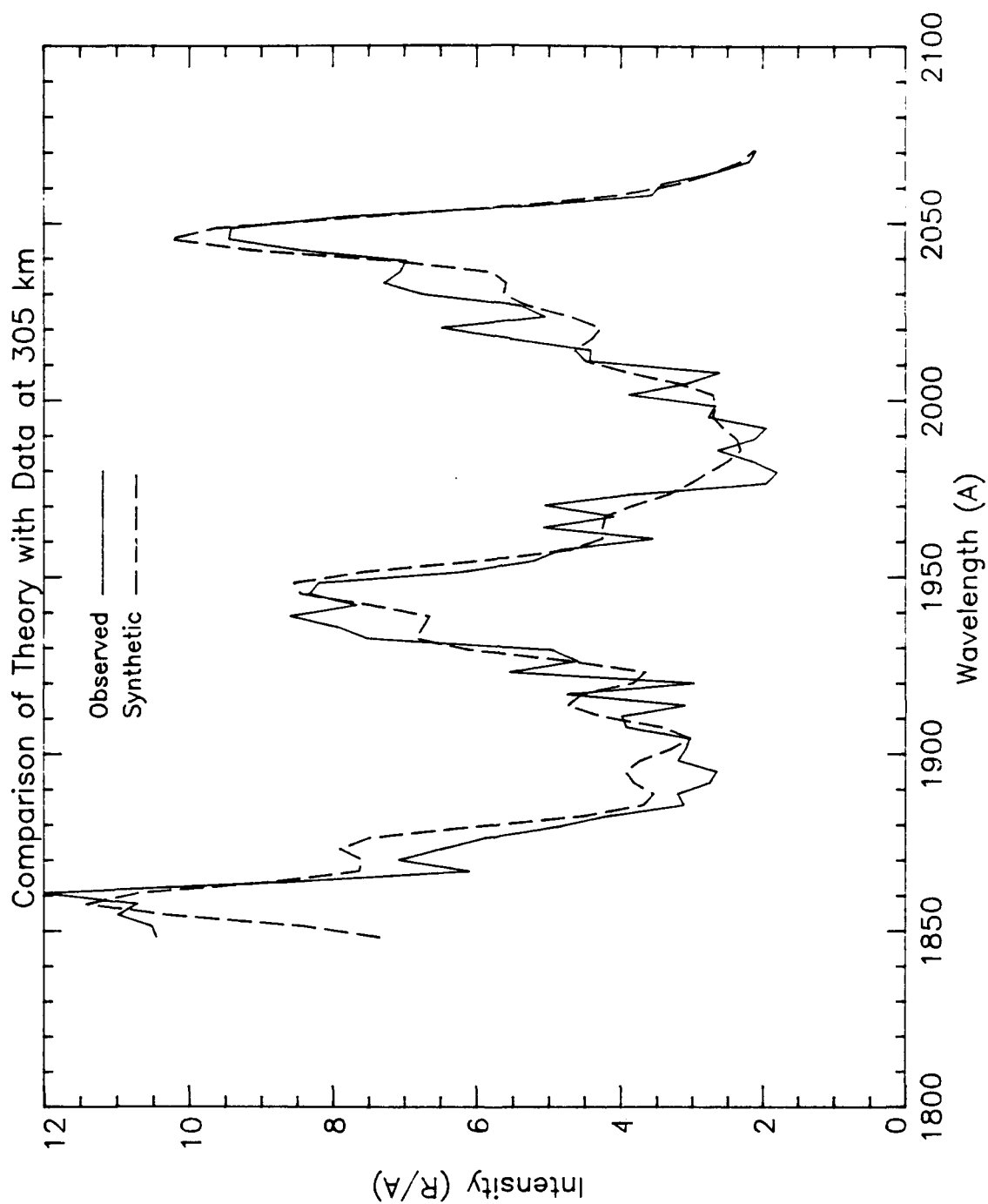


Figure 4-25 Comparison of Synthetic and Observed Spectra at 305 km



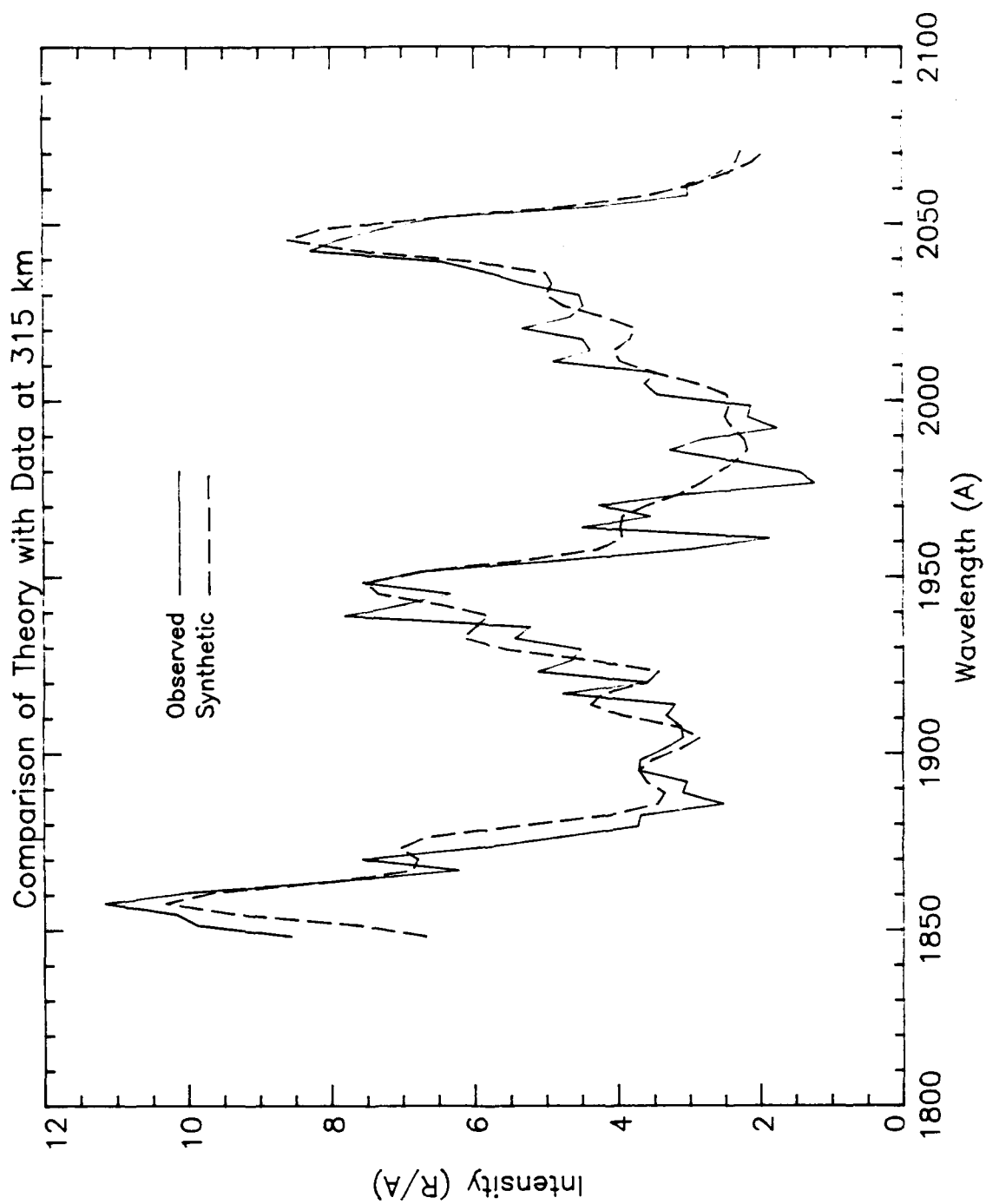


Figure 4-26 Comparison of Synthetic and Observed Spectra at 315 km

than  $12 \text{ R}/\text{\AA}$  at 315 km. Such a large change in the magnitude of the measured quantity causes problems with signal-to-noise ratio as can be seen by comparing Figures 4-2 and 4-26. At 105 km, nearly every feature of the observed spectrum is accounted for in the synthetic spectrum. Note that the spectrum varies smoothly and has almost no spikes. In contrast, the 315 km spectrum shows rapid fluctuation with wavelength and has many spikes. The small magnitude of the observed intensity exaggerates the effect of minor variations. Correspondingly, there are several features which are not mirrored in the synthetic fit. Nonetheless, the general shape of the 315 km spectrum is well matched by the synthetic spectrum, and prominent emissions such as the LBH (3,9) at  $1854 \text{ \AA}$  and the  $\gamma$  (2,0) at  $2047 \text{ \AA}$  are accurately modelled. The effect of altitude on the relative intensities between the LBH and the nitric oxide emissions can also be seen in the figures. Their different excitation mechanisms cause the NO and  $\text{N}_2$  emissions to dominate at different altitudes. The NO emissions are much more intense than the LBH emissions at low altitudes. Emitted intensities from the two species are comparable around 175 km altitude, with the LBH contributions becoming dominant above 185 km as photoelectron flux increases.

After the initial fitting was complete, the plots were evaluated for trends which would indicate ways to improve the fits. In comparing the synthetic spectra to the observed, it was noticed that the contributions from some vibrational transitions were consistently overestimated while other were underestimated. When the intensities at a given peak did not coincide, the difference between the synthetic and observed intensities as a fraction of the total intensity was used as a correction to the synthetic intensity. As discussed

in Chapter II, the influence of the vibrational terms on a spectrum is determined by the Franck-Condon factors. Correcting the intensity value generated by the synthetic spectrum model is equivalent, then, to changing the Franck-Condon factor for the vibrational transition concerned. Once the correction factors were found, new synthetic spectra were created and run through the fitting process. The specific vibrational transitions used in the comparisons are listed in Table 1 along with the scale factors they generated. Figure 4-27 gives a graphic representation of the corrections to nine of the LBH bands as a function of vibrational levels.

Generation of the correction factors was complicated by two characteristics of the spectra. First, there were some cases, for example the  $\epsilon(0,0)$  band at  $1877 \text{ \AA}$ , in which the synthetic intensity was not consistent in its deviation from the observed intensity. When this happened, the synthetic intensity was left unchanged, or was corrected to fit the largest possible number of the observed spectra. Second, and more importantly, all four of the band systems, NO  $\gamma$ ,  $\delta$ ,  $\epsilon$ , and LBH, exhibit some degree of overlap in the wavelength range of interest. This overlap means that the corrections for the bands are coupled. In an effort to reduce the effect of the coupling, peaks in the synthetic NO spectrum were compared with the measured spectrum at 105 km, where the nitric oxide emissions are much greater than those from  $\text{N}_2$ . Similarly, the LBH comparisons were made with the 265 km spectrum.

TABLE 1  
CORRECTIONS TO FRANCK-CONDON FACTORS

	Vibrational		Bandhead
	<u>Band</u>	<u>Correction</u>	<u>Wavelength (Å)</u>
N <sub>2</sub> LBH	1,8	1.3	1895
	2,9	1.0	1914
	2,10	1.0	1992
	3,9	1.2	1854
	3,10	0.8	1929
	3,11	0.8	2008
	4,10	1.0	1873
	4,11	0.9	1948
	4,12	0.9	2026
	5,11	1.4	1889
	5,12	0.75	1964
	5,13	1.2	2045
	6,13	1.0	1983
NO γ	2,0	1.0	2047
	3,0	1.0	1956
NO δ	No adjustments made to individual Franck-Condon factors.		
NO ε	0,0	0.9	1877
	0,1	1.15	1945
	1,1	0.6	1863

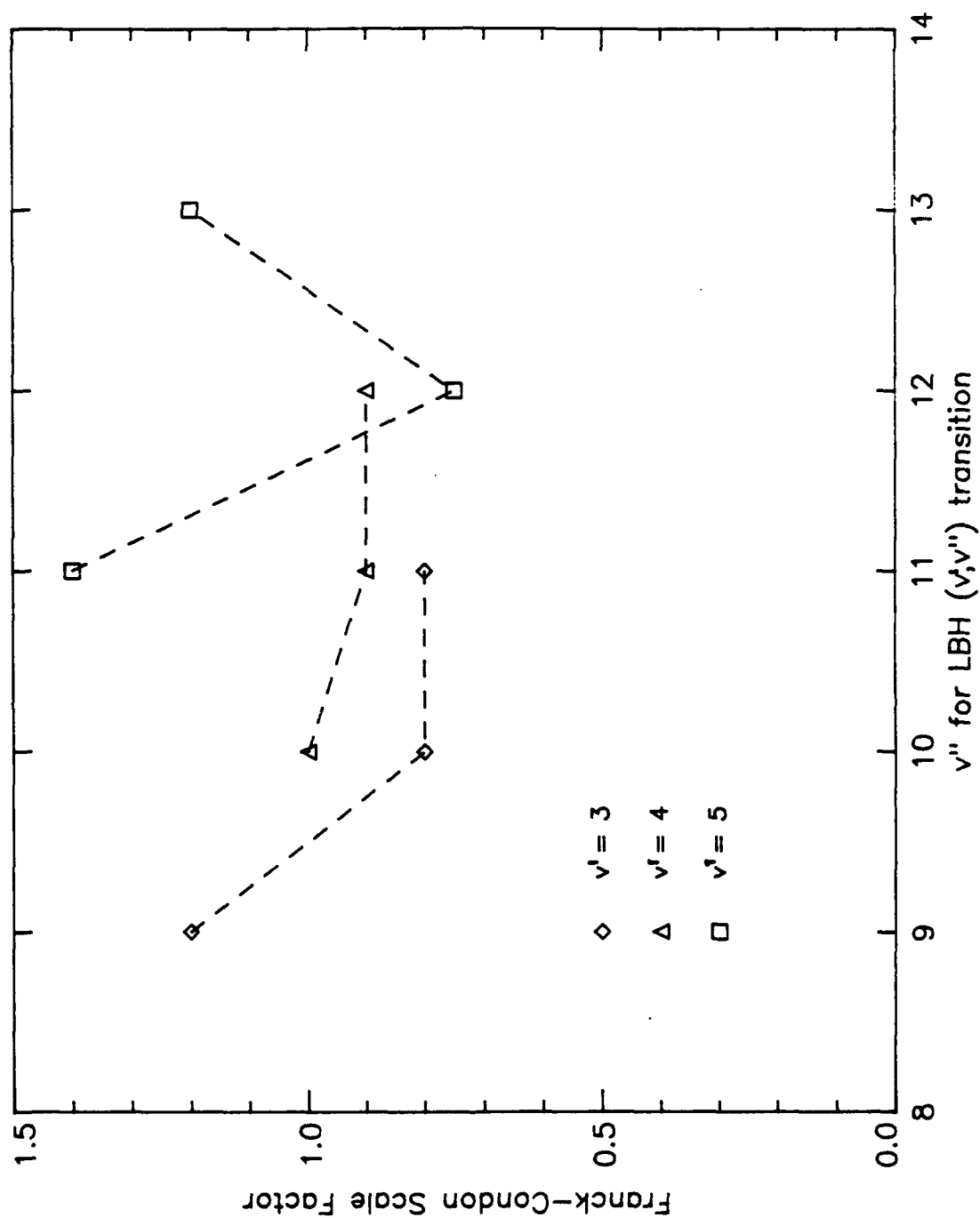


**Figure 4-27** Corrections to Franck-Condon Factors for Selected LBH Transitions

Figure 4-27 indicates that the Franck-Condon factors measured in this experiment agree fairly closely with theory for the (4,v") transitions. It also shows that the (3,9), (5,11), and (5,13) transitions are underestimated by theory, while the (3,10), (3,11), and (5,12) transitions are overestimated. These disagreements between measured and theoretical values may be partly due to the influence of strong emissions from the nitric oxide  $\epsilon(1,1)$  and  $\epsilon(0,0)$  bands which contaminate the portion of the spectrum from which the LBH corrections were estimated.

## B. COLUMN EMISSION RATES

When the fits were satisfactory, the scale factors between synthetic and observed spectra represented the column emission rates for nitric oxide and nitrogen. This rate can be converted directly to a column density for NO. The density profile for NO is shown in Figure 4-28. The error bars represent estimates of the maximum and minimum scale factors which will produce a plausible fit between the model and the observed data. The profile shows the expected exponential decrease of density with increasing altitude.

The results from the model calculations of LBH emissions are shown in Figure 4-29. These results represent the column emission rate profile for all of the LBH bands of  $N_2$ . These bands extend over a wavelength range of 1400 Å from 1205 Å to 2602 Å. In order to compare the emission rates from the MUSTANG data to the model, it was necessary to calculate the amount contributed to the entire LBH band system emission by the thirteen bands in the 1850 Å to 2070 Å region. This calculation was performed by summing the Franck-Condon factors for the thirteen bands listed in Table 1 and dividing by

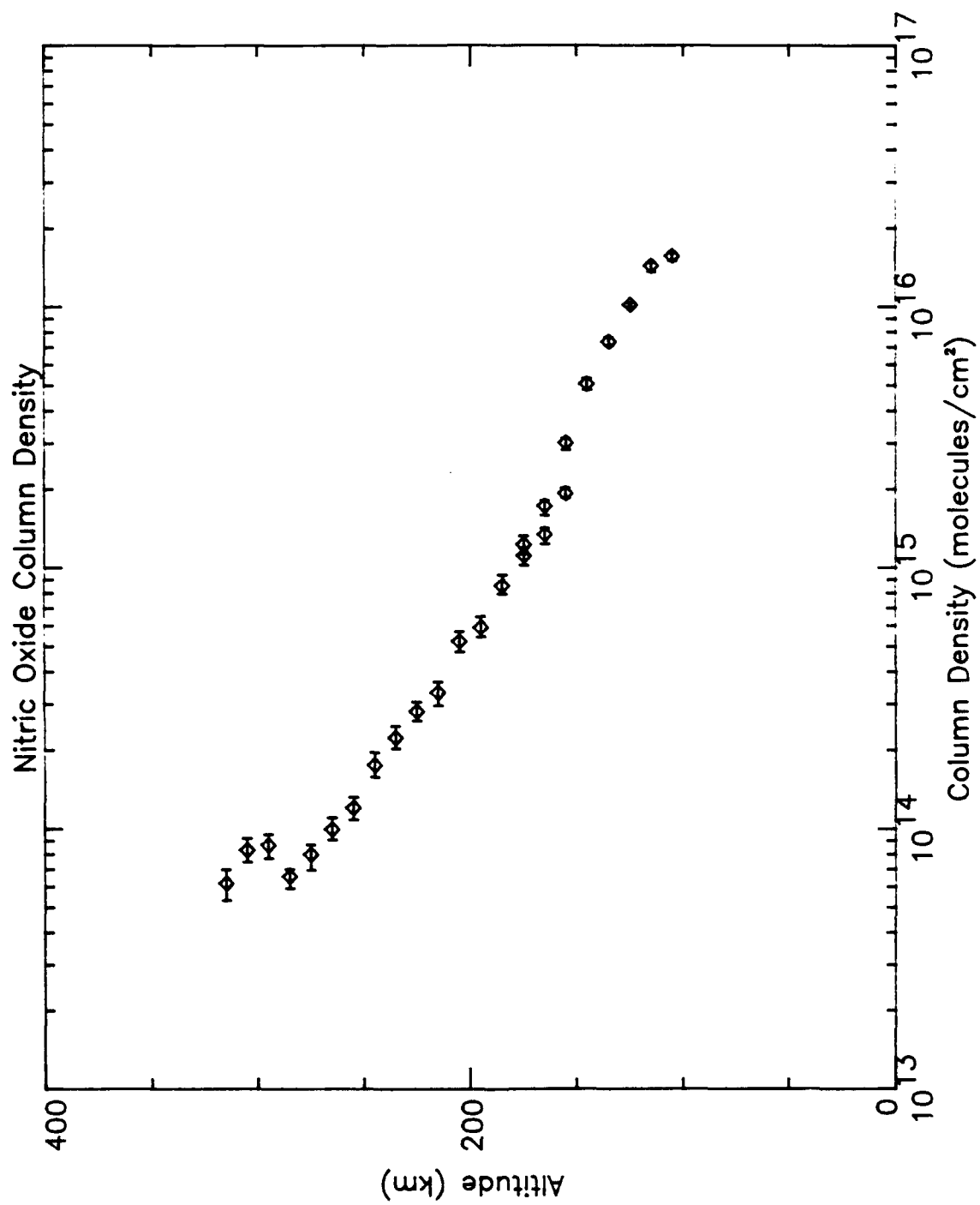
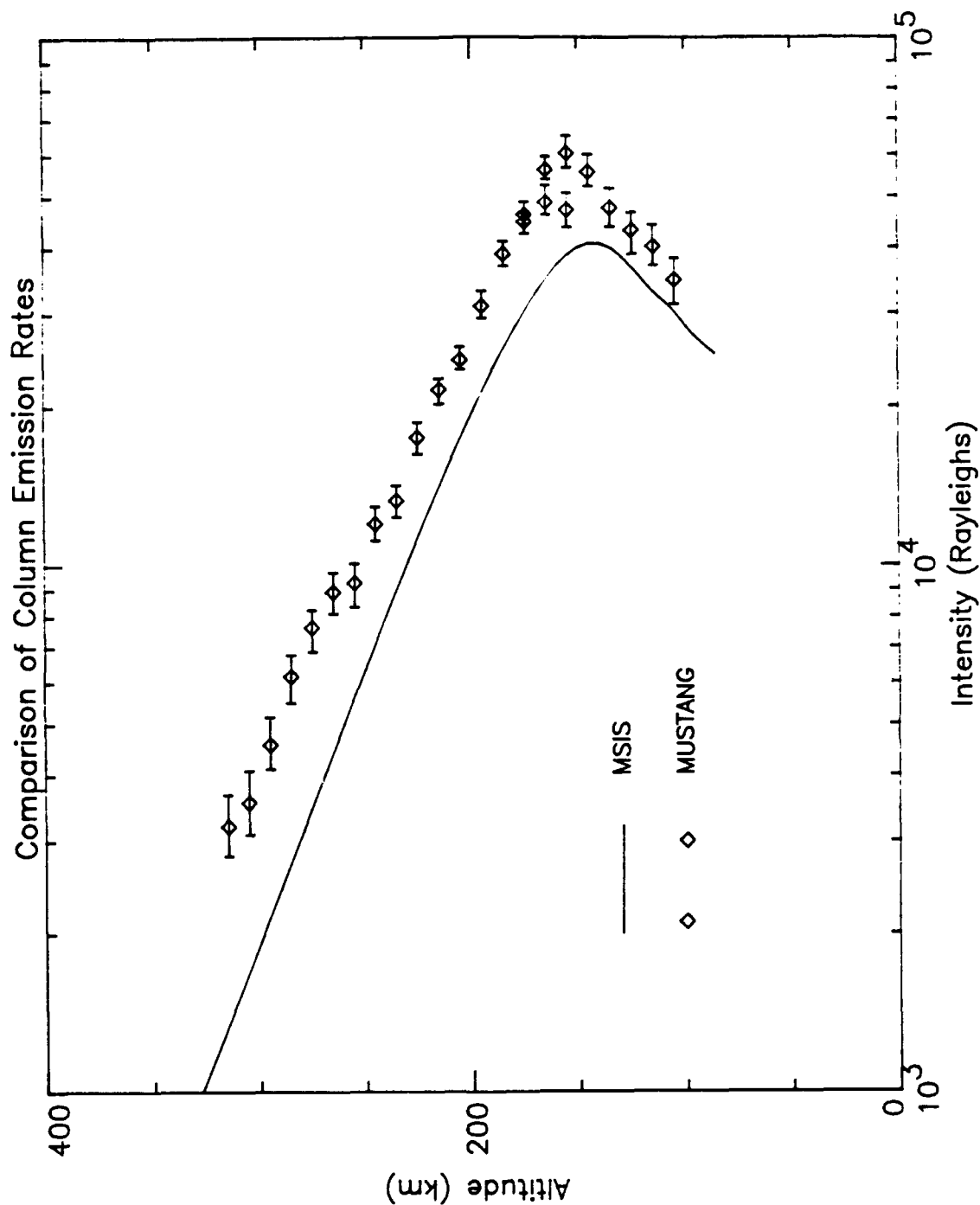


Figure 4-28 Nitric Oxide Column Density



**Figure 4-29 Comparison of Column Emission Rate Profiles.** The MSIS curve is for the following conditions: Densities at 120 km;  $[N_2] = 3.15 \times 10^{11} \text{ cm}^{-3}$ ,  $[O] = 9.09 \times 10^{10} \text{ cm}^{-3}$ ,  $[O_2] = 4.66 \times 10^{10} \text{ cm}^{-3}$ ;  $T_{\text{inf}} = 1312 \text{ K}$ .



the sum of all Franck-Condon factors for the LBH system. These bands represent approximately 21.1 percent of the total LBH emissions. The error estimates for the LBH emission rates again represent the maximum and minimum scale factors for achieving a believable fit with the observed spectra. The estimated error for the LBH terms is relatively large at low altitude because the LBH contribution to the recorded spectrum is overwhelmed by the nitric oxide contributions. At high altitude, the small signal-to-noise ratio leads to relatively large error estimates again.

As noted in Chapter II, the column emission rate for LBH cannot be converted directly to an  $N_2$  density because the photoelectron flux depends on that density. Consequently, Equation 2.15 cannot be solved directly for the density of  $N_2$ . Instead, the forward calculation must be iterated by varying the nitrogen density and the photoelectron flux until the calculated emission rate agrees with the observed rate. The photoelectron flux was estimated using two computer programs for atmospheric modelling. The neutral atmosphere was modelled by MSIS-83 (Hedin, 1983) using environmental conditions pertinent to the MUSTANG launch as inputs. The output from MSIS is a model of the neutral atmosphere with values for  $N_2$  density,  $O_2$  density, O density, and atmospheric temperature as a function of altitude. The model atmosphere was then fed into the NRL PEGFAC model which calculated the photoelectron flux using a Monte Carlo techniques. The diamond symbols in Figure 4-29 indicate the column emission rate measured by MUSTANG. The MUSTANG curve clearly does not coincide with the model curve. There are a number of explanations for the disparity between the profiles, one of which may be a difference between the actual temperature profile and that used in

the models. The temperature at high altitude in the thermosphere is called T-infinity or  $T_{inf}$ .  $T_{inf}$  calculated by MSIS was 1312 K. Clayton (1990), in his evaluation of the MUSTANG data, found a value for  $T_{inf}$  of 1800 K. The value of  $T_{inf}$  has a large impact on calculated column emission rate, especially at high altitude. The effect is shown in Figure 4-30 which presents emission rates calculated at 1312 K, 1500 K, and 1700 K. The difference in the two values may be partly explained by the differing methods used to calculate  $T_{inf}$ . Clayton produced his temperature profile by comparing the bandwidth of the NO  $\gamma(1,0)$  emission from a synthetic spectrum with that of the observed  $\gamma(1,0)$  emission. The MSIS model uses the F10.7 solar activity indication to create its temperature profile. The F10.7 value is a measure of solar output in the radio frequency portion of the electromagnetic spectrum which has become a benchmark for measuring solar activity. Unfortunately, changes in F10.7 are not linearly proportional to changes in UV activity, so the F10.7 index may not indicate the same temperature profile as that indicated by analysis of the bandwidth of ultraviolet emissions. Because his temperature profile was based on analysis of the MUSTANG data, Clayton's value of  $T_{inf}$  was used in this analysis.

Another reason for the disparity is the influence of the profiles for nitrogen density, molecular oxygen density, and atomic oxygen density, written  $[N_2]$ ,  $[O_2]$ , and  $[O]$  respectively. The MSIS density profiles are based on multi-year observations of densities under conditions similar to those given as inputs to the model. While this approach would be expected to produce reliable average results, individual cases may vary significantly from the long term average. The  $[N_2]$  and  $[O]$  profiles used in the PEGFAC models have a

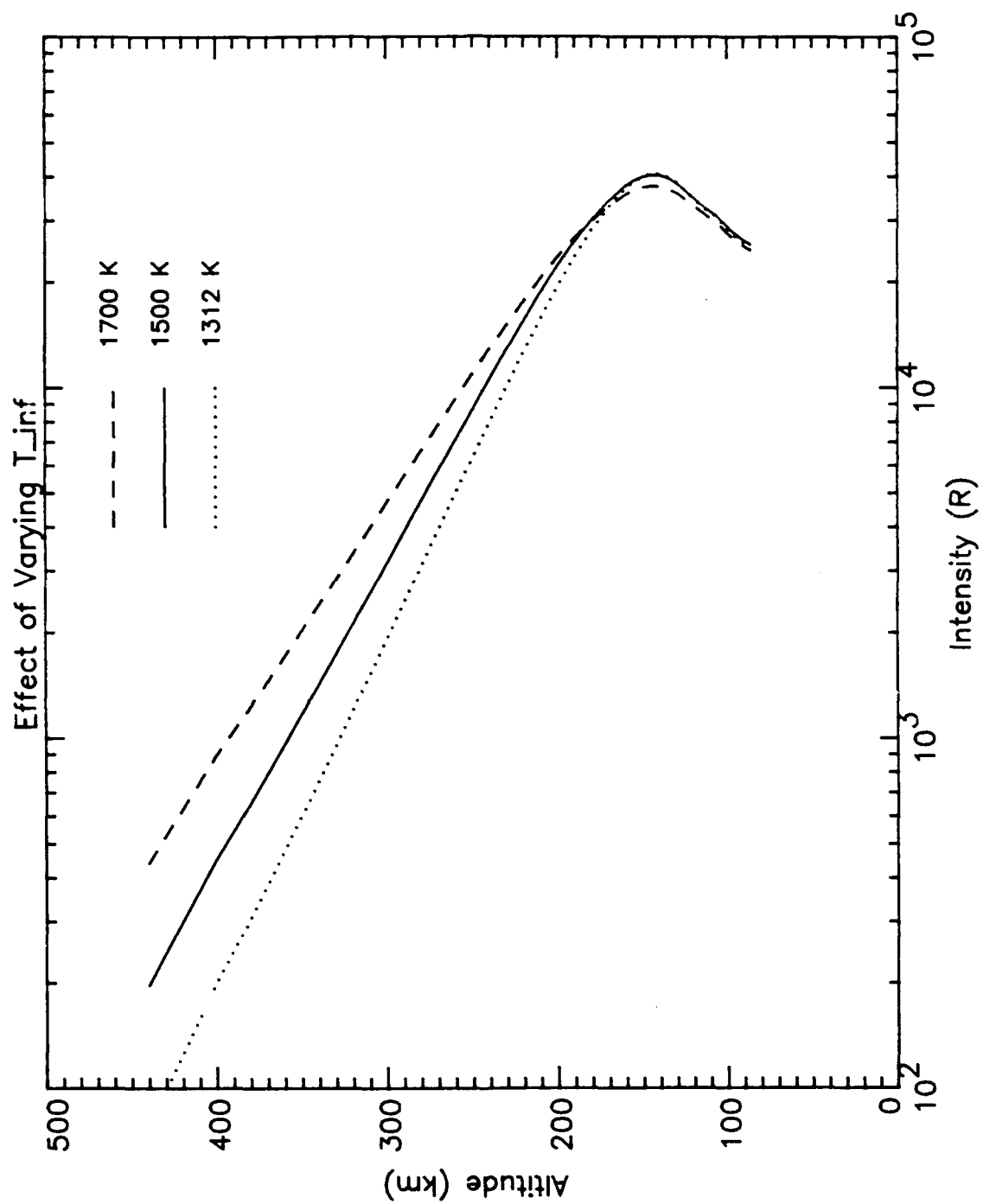
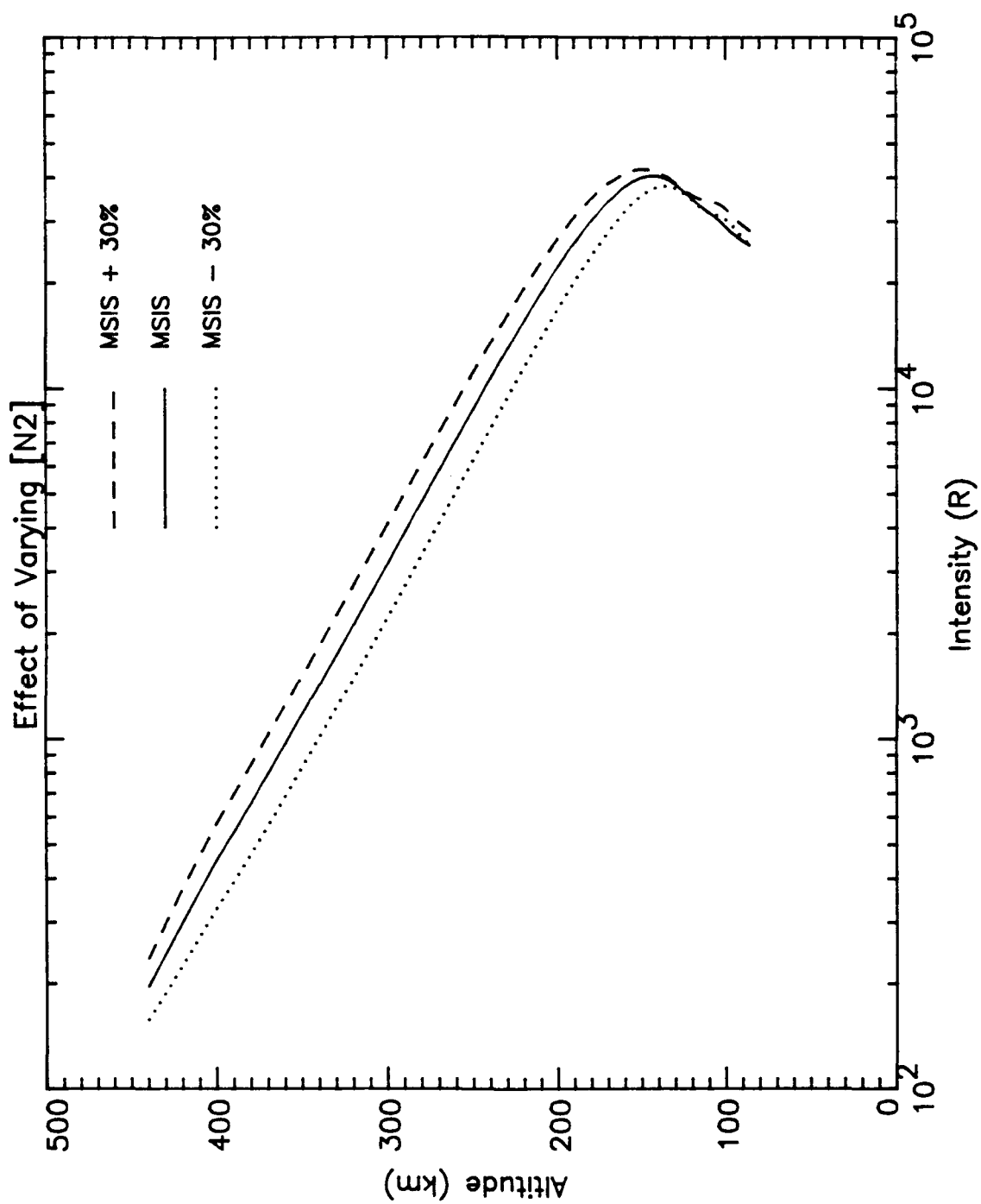


Figure 4-30 Effect on PEGFAC-Derived Emission Profile of Variation in  $T_{\infty}$  Parameter of MSIS

great influence on the calculated column emission rate as can be seen in Figures 4-31 and 4-32. The solid curve in each figure represents the emission rate derived from PEGFAC using the density calculated by MSIS, while the other curves show the effect of a 30% variation from the MSIS value. Figure 4-31 indicates that a change of 30% in the density of nitrogen at 120 km causes the emission rate to vary by approximately 30% at high altitudes. The peak value of intensity varies by only about 5%, but the height of the peak increases with increasing nitrogen density. The oxygen density profile in Figure 4-32 shows quite different properties. A 30% change in [O] has negligible effect on emission rate above 250 km, but causes the peak emission rate to vary by nearly 20%. The peak value decreases with increasing oxygen density, and the altitude of the peak remains constant. Changing the density of O<sub>2</sub> has little effect on the emission rate above 110 km (Figure 4-33).

Two different emission rate profiles from PEGFAC are compared with the MUSTANG profile in Figures 4-34 and 4-35. The MSIS parameters used to generate Figure 4-34 are:  $T_{inf} = 1500$  K, densities at 120 km;  $[N_2] = 4.10 \times 10^{11} \text{ cm}^{-3}$ ,  $[O] = 6.36 \times 10^{10} \text{ cm}^{-3}$ ,  $[O_2] = 4.66 \times 10^{10} \text{ cm}^{-3}$ . In Figure 4-35 the values are:  $T_{inf} = 1700$  K,  $[N_2] = 3.15 \times 10^{11} \text{ cm}^{-3}$ ,  $[O] = 4.55 \times 10^{10} \text{ cm}^{-3}$ , and  $[O_2] = 4.66 \times 10^{10} \text{ cm}^{-3}$ . While both figures indicate fairly good agreement in overall shape between the curves, in neither case are all features of the MUSTANG profile accounted for by the model. The peak of the intensity profile is not well fitted in both cases. Above 195 km, the model in Figure 4-34 shows good agreement with the MUSTANG data. Unfortunately, this agreement indicates a value for  $T_{inf}$  of 1500K, whereas Clayton's analysis of band widths indicated  $T_{inf}$  is 1800 K. Figure 4-35, at 1700 K, shows that the fit at high altitude is worse as

$T_{inf}$  approaches Clayton's value of 1800 K. In addition, the values of [O] in the two figures are not based on an independent measure of the atomic oxygen density. When it was clear that the MSIS values for oxygen and nitrogen densities would not give a close fit to the data, density values were chosen arbitrarily in an attempt to fit the model profile to the MUSTANG profile. The fact that Figure 4-35 shows reasonable agreement with the observed profile despite the large differences in parameter values from those in Figure 4-34 indicates that the method used in this thesis will not, by itself, allow calculation of a unique value for nitrogen density.



**Figure 4-31 Effect on PEGFAC-Derived Emission Rate of Variation in  $N_2$  Density Parameter of MSIS**

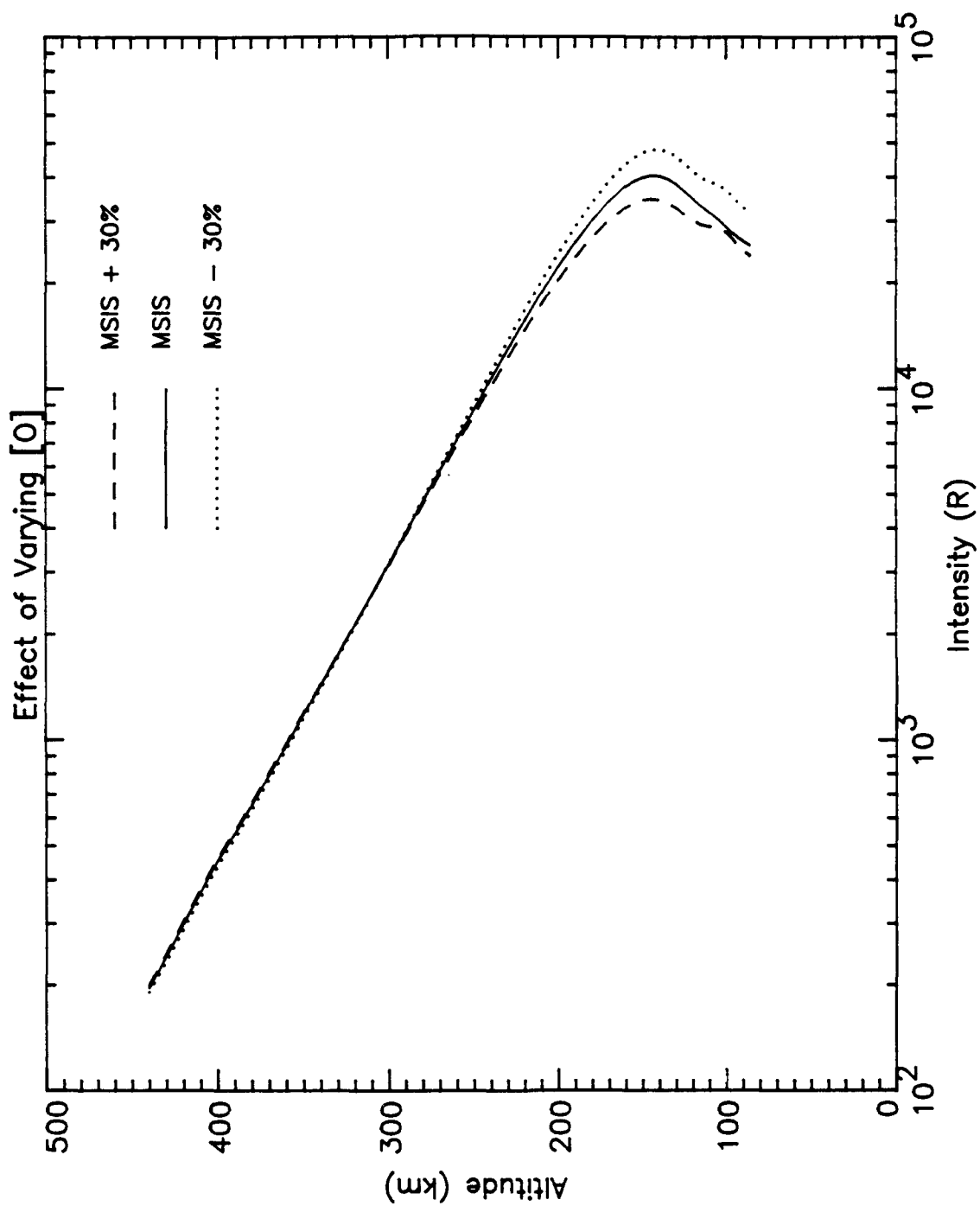
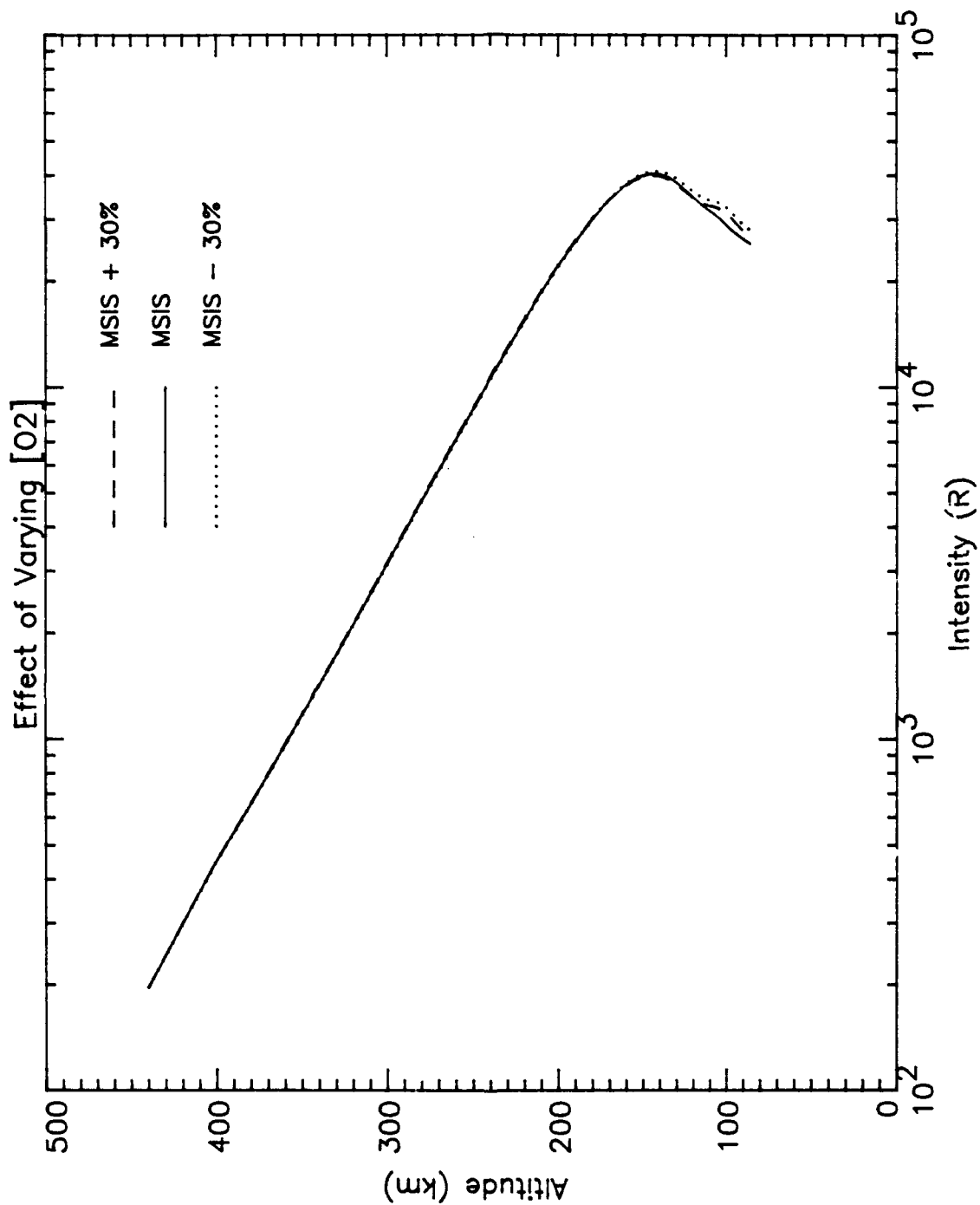


Figure 4-32 Effect on PEGFAC-Derived Emission Rate of Variation in O Density Parameter of MSIS



**Figure 4-33 Effect on PEGFAC-Derived Emission Rate of Variation in  $O_2$  Density Parameter of MSIS**



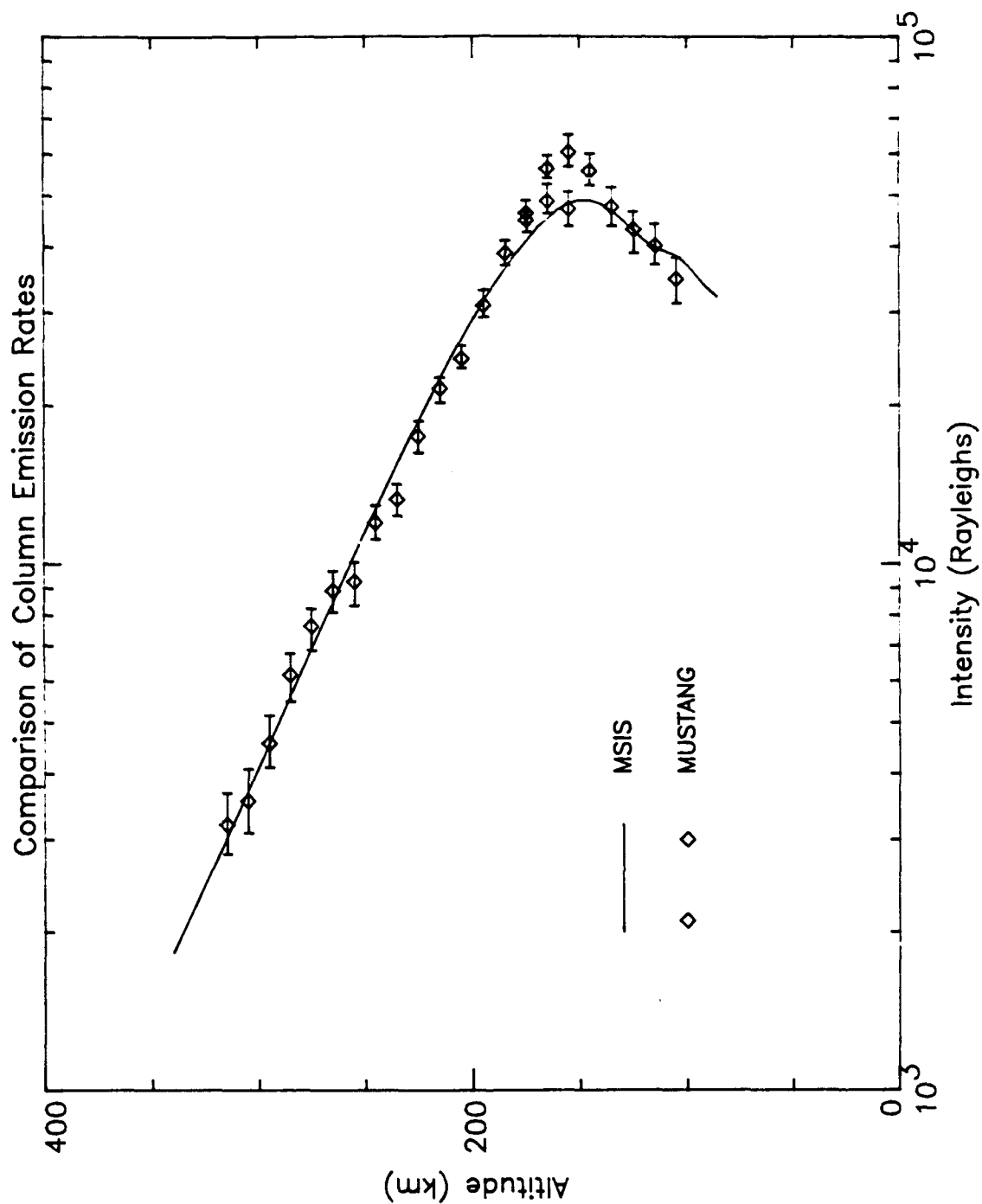


Figure 4-34 Comparison of Column Emission Rate Profiles. The MSIS curve is for the following conditions: Densities at 120 km;  $[N_2] = 4.10 \times 10^{11} \text{ cm}^{-3}$ ,  $[O] = 6.36 \times 10^{10} \text{ cm}^{-3}$ ,  $[O_2] = 4.66 \times 10^{10} \text{ cm}^{-3}$ ;  $T_{\text{inf}} = 1500 \text{ K}$ .

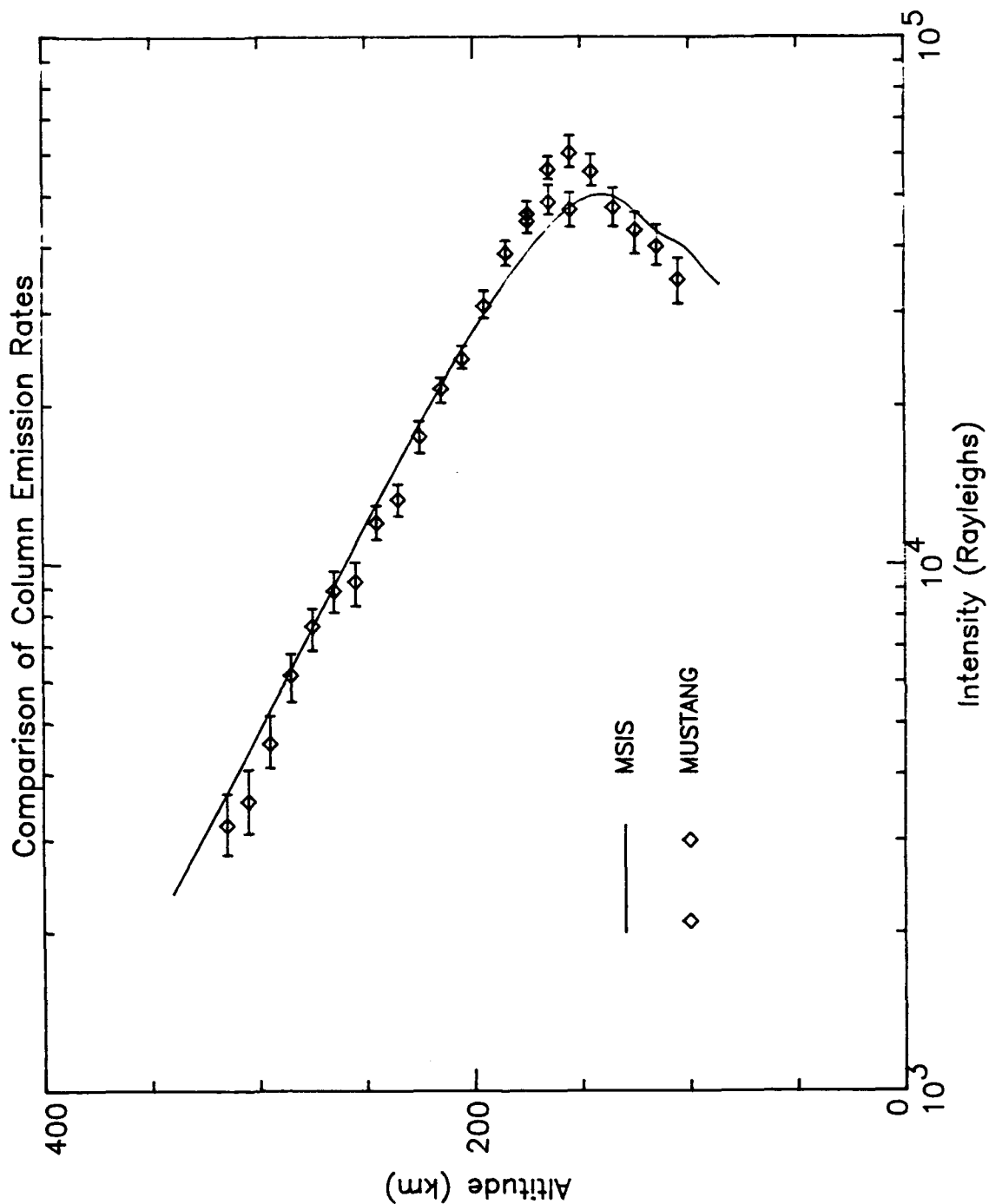


Figure 4-35 Comparison of Column Emission Rate Profiles. The MSIS curve is for the following conditions: Densities at 120 km;  $[N_2] = 3.15 \times 10^{11} \text{ cm}^{-3}$ ,  $[O] = 4.55 \times 10^{10} \text{ cm}^{-3}$ ,  $[O_2] = 4.66 \times 10^{10} \text{ cm}^{-3}$ ;  $T_{inf} = 1700 \text{ K}$ .

## V. CONCLUSION

### A. SUMMARY OF RESULTS

This thesis has demonstrated that synthetic spectra based on the calculation of excited state populations of molecular nitrogen and nitric oxide can be made to model accurately the observed airglow in the 1850 Å to 2070 Å wavelength region. The scale factors between the models and the measured spectra produce reasonable values for line-of-sight column densities of nitric oxide. Column densities for molecular nitrogen cannot be determined uniquely using the method outlined in this thesis. A vacuum calibration using a chamber manufactured from PVC pipe has been presented. The calibration was performed in a nitrogen atmosphere to prevent absorption of the ultraviolet radiation by oxygen. Chamber geometry and hardware considerations dictated that the vacuum calibration curve be used to extend an existing absolute calibration curve.

### B. RECOMMENDATIONS FOR FURTHER RESEARCH

The utility of measuring LBH emissions as a means to find nitrogen density depends critically on the ability to model the photoelectron flux which drives those emissions. An independent measure of the density of atomic oxygen is essential to reducing the number of free parameters used in generating the theoretical column emission rate for the LBH bands. An accurate temperature profile of the upper atmosphere is also needed. Further

insight into trends in the corrections to Franck-Condon factors may be gained by fitting synthetic spectra over a wider wavelength range than has been done to date.

Vacuum calibration of the MUSTANG spectrograph can be improved by repeating the procedure in a stainless steel vacuum chamber. A stainless steel chamber would eliminate the problem of outgassing experienced with PVC, and would allow the recording of spectra under high vacuum.

## REFERENCES

Andersen, C.K., *A Calibration of the Naval Postgraduate School Middle Ultraviolet Spectrograph and an Analysis of the OII 2470 Å and OI 2972 Å Emissions Obtained from Mid-Latitude Rocket Observations*, Master's Thesis, Naval Postgraduate School, 1990.

Bevington, P.R., *Data Reduction and Error Analysis for the Physical Sciences*, McGraw-Hill, Inc., 1969.

Bosserman, J.L., *Analysis of Thermospheric Dayglow Spectra from the Spacelab 1 Shuttle Mission*, Master's Thesis, Naval Postgraduate School, 1989.

Clayton, M.J., *Analysis of the Ultraviolet Emissions of Nitric Oxide from Mid-Latitude Rocket Observations*, Master's Thesis, Naval Postgraduate School, 1990.

Cleary, D.D., *Analysis of Nitric Oxide Fluorescence Bands from High Latitude Rocket Observations of the Thermospheric Dayglow*, Ph.D. dissertation, University of Colorado, 1985.

Cleary, D.D., "Daytime High-Latitude Rocket Observations of the NO  $\gamma$ ,  $\delta$ , and  $\epsilon$ , Bands", *Journal of Geophysical Research*, v.91, no.A10, 1986.

Eisberg, R. and Resnick, R., *Quantum Physics of Atoms, Molecules, Solids, Nuclei, and Particles*, Second Edition, John Wiley & Sons, Inc., 1985.

Hedin, A.E., "A Revised Thermospheric Model Based on Mass Spectrometer and Incoherent Scatter Data: MSIS-83", *Journal of Geophysical Research*, v.88, no.10170, 1983.

Herzberg, G., *Molecular Spectra and Molecular Structure I. Spectra of Diatomic Molecules*, Van Nostrand Reinhold, 1950.

Huber, K.P. and Herzberg, G., *Molecular Spectra and Molecular Structure IV. Constants of Diatomic Molecules*, Van Nostrand Reinhold, 1979.

Hund, F., "Zur Deutung der Molekulspektren", *Zeitschreif fur Physik*, v.42, p.93, 1927.

Tascione, T.F., *Introduction to the Space Environment*, Orbit Book Company, Inc., 1988

Vallance Jones, A., *Aurora*, D. Reidel Publishing Co., 1974

## INITIAL DISTRIBUTION LIST

	No. Copies
1. Defense Technical Information Center Cameron Station Alexandria, VA 22304-6145	2
2. Library, Code 0142 Naval Postgraduate School Monterey, CA 93943-5002	2
3. Dr. K. E. Woehler, Chairman Physics Department Naval Postgraduate School Monterey, CA 93943-5000	1
4. Dr. D. D. Cleary Physics Department, 61-CI Naval Postgraduate School Monterey, CA 93943-5000	4
5. Dr. S. Gnanalingam Physics Department, 61-Gm Naval Postgraduate School Monterey, CA 93943-5000	1
6. Space Systems Academic Group Code 72 Naval Postgraduate School Monterey, CA 93943-5100	1
7. LT Bryan D. Mack, USN 1356 Danielle Court Chesapeake, VA 23320	2
8. LT Billie S. Walden, USN Naval Education and Training Center Surface Warfare Officer School Command Newport, RI 06340	1